NOVEL IMAGING TECHNIQUES TO IMPROVE THE ACCURACY OF MEASUREMENT IN MAGNETIC RESONANCE IMAGING

by

Xianfeng Shi

A dissertation submitted to the faculty of
The University of Utah
in partial fulfillment of the requirements for the degree of

Doctor of Philosophy

in

Physics

Department of Physics and Astronomy

The University of Utah

May 2010

STATEMENT OF DISSERTATION APPROVAL

The dissertation of [redacted]**Shi**

has been approved by the following supervisory committee members:

Brian Saam	, Chair	**03/11/2010**
Eun-Kee [redacted]	, Member	**02/25/2010**
Dennis L. Parker	, Member	**03/01/2010**
Carleton Detar	, Member	**02/26/2010**
[redacted] **C.** [redacted]	, Member	**03/01/2010**

and by [redacted], Chair of

the Department of [redacted] **and** [redacted]

and by Charles A. Wight, Dean of The Graduate School.

ABSTRACT

Magnetic resonance imaging (MRI) techniques are widely applied in various disease diagnoses and scientific research projects as noninvasive methods. However, lower signal-to-noise ratio (SNR), B_1 inhomogeneity, motion-related artifact, susceptibility artifact, chemical shift artifact and Gibbs ring still play a negative role in image quality improvement. Various techniques and methods were developed to minimize and remove the degradation of image quality originating from artifacts.

In the first part of this dissertation, a motion artifact reduction technique based on a novel real time self-gated pulse sequence is presented. Diffusion weighted and diffusion tensor magnetic resonance imaging techniques are generally performed with signal averaging of multiple measurements to improve the signal-to-noise ratio and the accuracy of diffusion measurement. Any discrepancy in images between different averages causes errors that reduce the accuracy of diffusion MRI measurements. The new scheme is capable of detecting a subject's motion and reacquiring motion-corrupted data in real time and helps to improve the accuracy of diffusion MRI measurements.

In the second part of this dissertation, a rapid T_1 mapping technique (two dimensional singleshot spin echo stimulated echo planar image--2D ss-SESTEPI), which is an EPI-based singleshot imaging technique that simultaneously acquires a spin-EPI (SEPI) and a stimulated-EPI (STEPI) after a single RF excitation, is discussed. The magnitudes of SEPI and STEPI differ by T_1 decay for perfect 90^o RF pulses and can be

used to rapidly measure the T_1 relaxation time. However, the spatial variation of B_1 amplitude induces uneven splitting of the transverse magnetization for SEPI and STEPI within the imaging FOV. Therefore, correction for B_1 inhomogeneity is critical for 2D ss-SESTEPI to be used for T_1 measurement.

In general, the EPI-based pulse sequence suffers from geometric distortion around the boundary of air-tissue or bone tissue. In the third part of this dissertation, a novel pulse sequence is discussed, which was developed based on three dimensional singleshot diffusion weighted stimulated echo planar imaging (3D ss-DWSTEPI). A parallel imaging technique was combined with 3D ss-DWSTEPI to reduce the image distortion, and the secondary spin echo formed by three RF pulses (90^0-180^0-90^0) is used to improve the SNR. Image quality is improved.

To my wife

CONTENTS

LIST OF ACRONYMS

DWI	Diffusion Weighted Image
DTI	Diffusion Tensor Image
EPI	Echo Planar Imaging
FFT	Fast Fourier Transform
FID	Free Induction Decay
FOV	Field of View
FT	Fourier Transform
GRAPPA	Generalized Autocalibrating Partially Parallel Acquisition
GRE	Gradient Echo
Hz	Hertz (1 cycle/second)
MRI	Magnetic Resonance Imaging
NMR	Nuclear Magnetic Resonance
PE	Phase Encoding
RF	Radio Frequency
ROI	Region of Interest
SE	Spin Echo
SEPI	Spin Echo Planar Image
SNR	Signal-to-Noise Ratio
STE	Stimulated Echo

STEPI	Stimulated Echo Planar Image
T_1	Spin-Lattice Relaxation Time Constant
T_2	Spin-Spin Relaxation constant
TE	Time of Echo
TR	Repetition Time

ACKNOWLEDGMENTS

I would like to thank all the people who have helped and inspired me during my doctoral study.

It is difficult to overstate my gratitude to my Ph.D. supervisor, Dr. Eun-Kee Jeong. With his enthusiasm, his inspiration, and his great efforts to explain things clearly and simply, he made me deeply understand not only all kinds of magnetic imaging techniques but also basic physical significance. His endless guidance and assistance during my Ph.D. work made this dissertation possible. Without his valuable advice and continuous patience, I could not have overcome the numerous difficulties in my research.

I would also like to express my deep and sincere gratitude to Dr. Eugene G. Kholmovski. His wide knowledge and deep understanding of image reconstruction principles was of great benefit to me. His effort has been engraved into this dissertation. His kindness and help will never be forgotten.

I am likewise heartily thankful to Dr. Dennis L. Parker whose encouragement, guidance and support from the initial to the final level enabled me to develop an understanding of the MRI principle.

I would like also to express my gratitude to Dr. Brian Saam, Dr. Benjamin Bromley and Dr. Carleton Detar for serving on my Ph.D. committee.

I wish to thank Dr. SeongEun Kim, Dr. Taeho Kim, Dr. Junyu Guo, and Xin Liu. Their valuable advice and help benefit me a lot. I also thank all the other faculty, students and staff in the UCAIR for their warm friendship and kind help in various ways.

Finally, I express my deepest appreciation to my parents and my wife. Their love, caring and support for me have led me through the hardest times of my Ph.D. study and have become the soul of this dissertation.

CHAPTER 1

INTRODUCTION

1.1 Motivations

Magnetic Resonance Imaging (MRI) is a state of the art imaging technology that has shown many advantages in medical imaging such as noninvasive measurement, absence of side effects, remarkable soft-tissue contrast, and an ability to acquire images in any plane when compared to Positron Emission Tomography (PET) or X-ray Computer Tomography (X-ray CT). MRI is widely used for medical disease diagnosis and underlying scientific research. One of the major advantages of MRI is its rich numbers of image contrast and method to quantify various physiologic information. For instance, T_1 and T_2 weighted MRI are routinely used.

Diffusion weighted imaging is an important application of MRI. The basic principle of diffusion weighted magnetic resonance imaging was introduced in the 1980s. The most successful application of DWI is to detect endangered tissue in acute brain ischemia. Diffusion anisotropy is firstly detected by diffusion MRI. Diffusivity is larger in the fiber direction than in the direction perpendicular to fiber. To quantify the anisotropy of the background microstructure, diffusion tensor imaging is used to extract the fiber running direction. The apparent diffusion coefficient (ADC) calculated from a set of diffusion weighted images provides complemetary information to the conventional T_1 and T_2 weighted images used in disease diagnosis. Motion artifacts are caused by the

subject's motion during MRI data acquisition. Using a singleshot imaging technique (EPI: Echo-Planar-Imaging), the motion during the period of sampling can be considered as "frozen" in the first order approximation. However, the strong diffusion gradient is sensitive to motion, and motion usually leads to lower SNR. Furthermore, averaging multiple signals is a method to increase the SNR. The problem arises when the sequence is repeated several times with different motion patterns. Diffusion weighted image quality is degraded by inconsistent motion among the different averaged measurements. Subsequently, the accuracy of the DTI parameters evaluated from these motion-corrupted images may be decreased.

EPI-based imaging techniques are widely used in DWI because of their fast sampling speed. One disadvantage of imaging using EPI is the geometric distortion that is induced by the locally variant magnetic field at/near the interfaces of tissue/air and tissue/bone. The abrupt change in the magnetic susceptibility at the tissue interface induces the locally varying magnetic field, which causes a signal shift. This geometric distortion greatly limits the application of the singleshot EPI to a large region of the brain.

Dynamic enhanced contrast MRI can provide noninvasive pharmacokinetics. In most cases, temporal change of the signal intensity is used to evaluate the pharmacokinetics. One shortcoming is that signal behavior strongly relies on imaging techniques. Signal intensity shows a nonlinear relationship with contrast agent concentration. On the other hand, the intrinsic character of a water molecule such as T_1 relaxation time is also altered by the introduction of a contrast agent. However, experiments demonstrate that $\Delta R_1 \left(= \frac{1}{T_1(c)} - \frac{1}{T_1(0)}\right)$ is proportional to the contrast agent

concentration. To calculate ΔR_1, dynamic and accurate T_1 relaxation time measurement is required.

1.2 Overview of Dissertation

This dissertation is composed of six chapters including this introduction. Chapter 2 introduces the basic principle of magnetic resonance using both quantum and classical descriptions of magnetization. Data acquisitions and image reconstructions are reviewed in detail as well.

Chapter 3 explains a new scheme that realizes real-time self-gated data acquisition to improve the accuracy of the diffusion tensor imaging. In general, motion-corrupted diffusion weighted data show signal attenuation in the k-space center and k-space center shift depending on the motion pattern. By monitoring the change of k-space center position and intensity, the pulse sequence determines which acquisition is corrupted by motion and reacquires the corrupted data. Especially for human patient data collection, we are unwilling to perform the same measurement several times because of occasional motion during the experiment. It is not only inconvenient to the patient but also increases the expense by requiring another scan. If no additional motion correction method is applied, corrupted data must be removed from the analysis, which reduces the SNR. Motion-corrupted data will be reacquired in real time and the effect of motion on diffusion weighted image is minimized. Thus, the accuracy of parameters calculated based on these images is greatly improved.

Chapter 4 discusses a new pulse sequence (2D ss-SESTEPI), which rapidly acquires a complete T_1 map in a singleshot. The rapid T_1 mapping may be useful to dynamically measure the concentration of the gadolinium-based MRI contrast agent for

tumor evaluation. 2D ss-SESTEPI is an EPI-based singleshot imaging technique that simultaneously acquires a spin-EPI and stimulated-EPI after a single RF excitation. The magnitudes of SEPI and STEPI differ by T_1 decay for perfect 90^o RF pulses and can be used to rapidly measure the T_1 relaxation time. However, the spatial variation of B_1 amplitude induces uneven splitting of the transverse magnetization for SEPI and STEPI within the imaging FOV. Therefore, correction of B_1 inhomogeneity is critical for 2D ss-SESTEPI to be used for T_1 measurement. B_1 inhomogeneity correction is performed by acquiring an additional stimulated-echo with minimal mixing time, calculating the difference between the spin-echo and the stimulated-echo and multiplying the stimulated-EPI by the inverse functional map.

Chapter 5 introduces a new pulse sequence design for image geometric distortion reduction. A parallel imaging technique was successfully implemented into the previously developed 3D ss-DWSTEPI (3D singleshot diffusion-weighted stimulated EPI) pulse sequence to increase the k_y travel speed and reduce the geometric distortion. The problem arises when the parallel imaging technique is applied. Because the total amount of data is halved, the SNR of the resultant images is reduced. A spin-echo-EPI was sampled from the transverse magnetization, which was left from the tipup 90 RF pulse in stimulated-echo acquisition. This transverse magnetization was discarded in conventional stimulated-echo imaging. The summation of secondary spin EPI and stimulated EPI improves the image SNR. This technique could be implemented in the presence of tissue interfaces and improve the image quality.

Chapter 6 summarizes the achievements and demonstrates the limitations of this dissertation as well as giving suggestions for future work.

CHAPTER 2

MAGNETIC RESONANCE IMAGING PRINCIPLES

The NMR (Nuclear Magnetic Resonance) phenomenon was first observed in bulk matter independently by Felix Bloch (1) and Edward Purcell (2) in 1946. They were later awarded the Nobel Prize in physics in 1952 for their discoveries. Then in 1971, Raymond Damadian discovered that the relaxation times of water proton in tissues and tumors differed (3). Since then, scientists have tried to use NMR to study disease. In 1973, Paul Lauterbur introduced gradients in the magnetic field. This spatial information was encoded in two-dimensional (2D) images. He first displayed magnetic resonance imaging on small test tube samples (4). In 1975, Richard Ernst used phase and frequency encodings, and the Fourier Transform to construct magnetic resonance images (5). Current MRI (magnetic resonance imaging) techniques mostly originated from this technique. In 1991, Ernst was awarded The Nobel Prize in Chemistry for his contribution to pulsed Fourier Transform NMR and MRI. Also in 1975, Peter Mansfield proposed a fast imaging technique called Echo Planar Imaging (EPI) to perform real-time movie imaging of a single cardiac cycle in 1987 (6). By using Ernst's technique, Edelstein and coworkers achieved body imaging in 1980 (7). As time went on, MRI techniques were rapidly developed and progressed to realize clinical application. In 1993, using singleshot EPI, functional MRI (fMRI) was introduced. It assisted us in discovering the function of the various regions of the human brain.

2.1 Nuclear Magnetic Resonance

NMR describes a physical phenomenon on the basis of the magnetic properties of an atom's nucleus. A macroscopic object consists of a great deal of atoms. The collective behavior of these atoms under the effect of an applied magnetic field has been studied. Faraday's Law demonstrates that the electromotive force (emf) inside a closed circuit is induced while the magnetic flux enclosed in this loop is varied. It implies that a receiver coil can be regarded as a tool of signal detection of a macroscopic object in an applied magnetic field.

Furthermore, substance magnetization is also equal to magnetic field multiplied by a constant called magnetic susceptibility. The induced signal is proportional to the product of Larmor frequency and magnetization. Thus, high magnetic field strength and nuclei with large gyro-magnetic ratios and greater abundance can improve the sensitivity of signal detection in NMR experiments. Because ^{1}H nuclei satisfy the large abundance in biological systems from Table 2.1, they appear to provide the highest sensitivity in NMR studies in vivo. Figure 2.1 shows a simplified diagram of nuclear magnetic resonance signal acquisition. Any change in the magnetic environment of a coil of wire will cause a voltage (emf) to be "induced" in the coil. No matter how the change occurs, the voltage will be generated.

2.1.1 Classical Description

In the presence of a magnetic field, the magnetic moments precess around the applied magnetic field (Figure 2.2). The relationship between the magnetic moment of the nucleus and its intrinsic spin angular momentum is expressed as:

Table 2.1. List of selected nuclei found in the human body with natural abundance, spin, gyromagnetic ratio and their elemental abundance.

Nucleus	Symbol	Natural Abundance (%)	Spin (ħ)	Gyromagnetic ratio γ (MHz/T)	Elemental abundance in body (%)
Hydrogen	^{1}H	99.985	1/2	42.58	63
	^{2}H	0.015	1	6.54	63
Phosphorus	^{31}P	100	1/2	17.25	0.24
Sodium	^{23}Na	100	3/2	11.27	0.041
Nitrogen	^{14}N	99.63	1	3.08	1.5
Carbon	^{13}C	1.11	1/2	10.71	9.4
Fluorine	^{19}F	100	1/2	40.08	0
Oxygen	^{17}O	0.037	5/2	-5.77	26

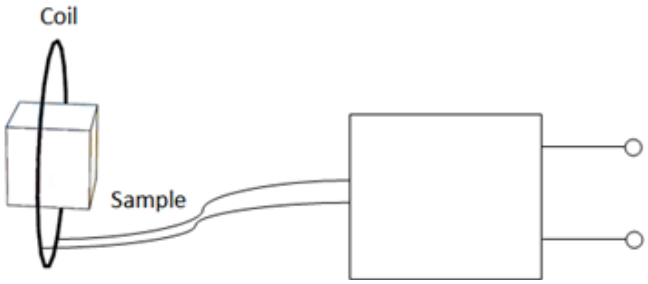

Figure 2.1. Simplified diagram of a surface coil.

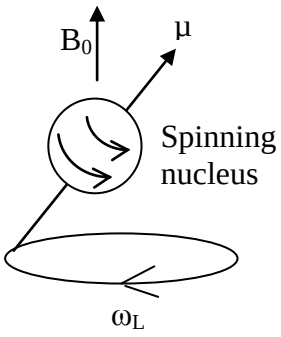

Figure 2.2. In the presence of an applied magnetic field B_0, nuclei with nonzero spin precess about the field.

$$\vec{\mu} = \gamma \vec{I} \tag{2.1}$$

where $\vec{\mu}$ is the nuclear magnetic dipole moment and $\vec{I}$ is its spin angular momentum. γ is a physical constant known as the gyromagnetic ratio. For the hydrogen nucleus, $\gamma = 2.675 \times 10^8 rad/s/T$. The frequency at which the nucleus precesses about the magnetic field is known as the Larmor frequency, ω_L.

$$\omega_L = \gamma B_0 \tag{2.2}$$

The magnetic field resulting from the magnetic dipole moment $\vec{\mu}$ can be deduced. The net magnetic field induced by all the nuclei in a given volume can be identified by the vector sum of their magnetic moments. The sum is referred to as the nuclear magnetization represented by **M.** The component of **M,** which is perpendicular to the static magnetic field $\mathbf{B}_0$, precesses at the Larmor frequency, ω_L. This produces an oscillating magnetic field that can be detected with an RF receive coil. At equilibrium, nuclei precess with random phases. So the transverse components of their magnetic moments cancel out, and no detectable signal is observed. But a small net magnetization in the longitudinal direction still exists.

2.1.2 RF excitation

By applying a transverse oscillating magnetic field to the tissue at exactly the Larmor frequency ω_L , the nuclear magnetization can be tipped away from the longitudinal axis (8), producing a finite component in the transverse plane. A detectable signal can be generated by the excess precessing nuclei on the transverse plane, as shown in Figure 2.3.

2.1.3 Free Induction Decay

After a time-varying magnetization is excited by the RF pulse, the detectable signal decays subject to T_1 and T_2 (T_2^*) relaxation decay mechanism in a given volume of tissue. Figure 2.4 shows only T_2^* relaxation. T_1 represents the spin-lattice relaxation time and T_2 is referred to as the spin-spin relaxation time.

2.1.3.1 T_1 Relaxation Time

T_1 is also called the longitudinal relaxation time. It is a measure of the time required for a substance in an applied magnetic field to remain longitudinally magnetized

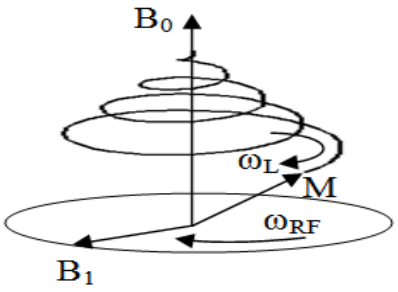

Figure 2.3. When a radio frequency (RF) field B_1 is applied at a frequency that exactly matches the larmor frequency of the nuclei, $\omega_{RF} = \omega_L$, the net magnetization is tipped away from the longitudinal direction.

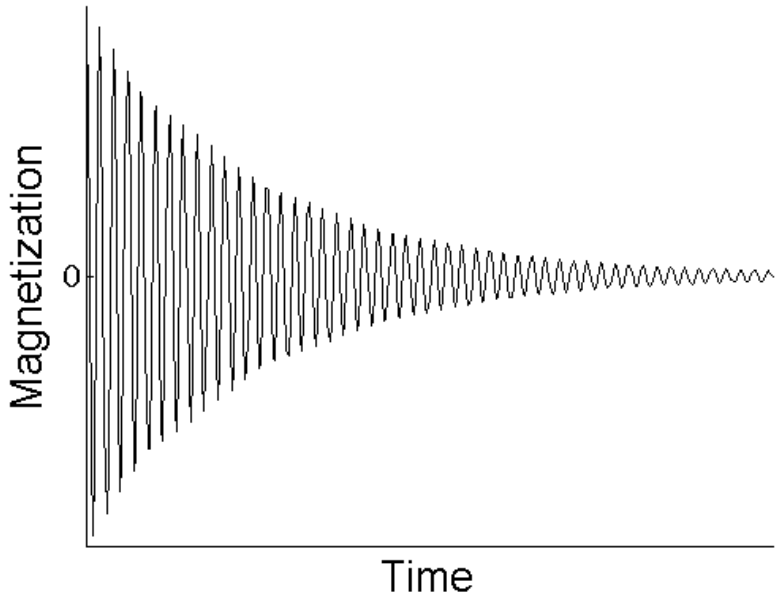

Figure 2.4. Signal detected from receiver coil undergoes T_2^* relaxation decay in the lab reference frame.

following an RF pulse. In other words, T_1 is the time constant for our system to release the energy absorbed due to the RF pulse into the environment. T_1 is determined by thermal fluctuations in the environment or lattice. Lattice or environment refers to as a system consisting of any other nuclei excluding the labeled resonating proton as shown in Figure 2.5. (a) Diagram demonstrates the resonating proton surrounded by lattice or environment. (b) Due to thermal fluctuation, the resonating proton experiences variation in the local magnetic field. The interaction between the resonating proton and the local magnetic field induces T_1 relaxation.

Dipole-dipole interaction (9) is one of most prominent relaxation mechanism. The classical interaction energy (U) between two dipole moments $\overrightarrow{\mu_1}$ and $\overrightarrow{\mu_2}$ is

$$U = \frac{\overrightarrow{\mu_1} \cdot \overrightarrow{\mu_2}}{r^3} - \frac{3(\overrightarrow{\mu_1} \cdot \vec{r})(\overrightarrow{\mu_2} \cdot \vec{r})}{r^5} \qquad (2.3)$$

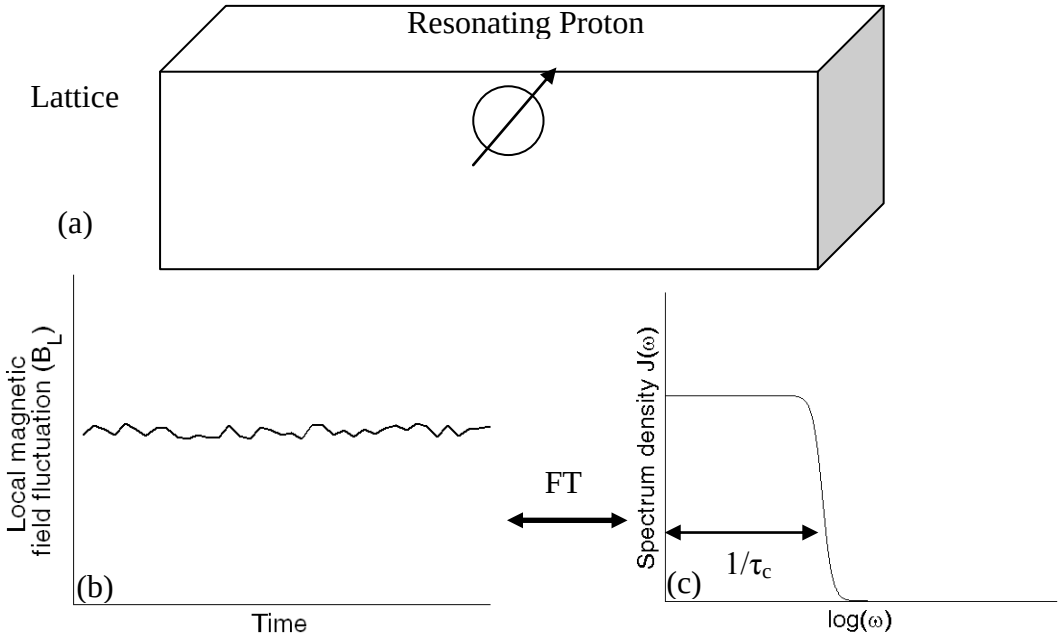

Figure 2.5. Illustration of lattice, local field fluctuation and spectral density. (a) Resonating proton lies inside the lattice environment. (b) Resonating proton experiences local magnetic field fluctuation due to thermal interaction. (c) By performing Fourier transform on (b), spectral density is calculated.

The relationship between magnetic moment and spin angular moment is described $\overrightarrow{\mu_1} = \gamma_1 \hbar \overrightarrow{I_1}$ and $\overrightarrow{\mu_2} = \gamma_2 \hbar \overrightarrow{I_2}$. The Hamiltonian for this system can be written in a form.

$$\mathcal{H} = \frac{\gamma_1 \gamma_2 \hbar^2}{r^3}(A + B + C + D + E + F) \tag{2.4}$$

where $A = I_{1z} I_{2z}(1 - 3cos^2\theta)$

$$B = -\frac{1}{4}(I_1^+ I_2^- + I_1^- I_2^+)(1 - 3cos^2\theta)$$

$$C = -\frac{3}{2}(I_1^+ I_{2z} + I_{1z} I_2^+) sin\theta cos\theta e^{-i\phi}$$

$$D = -\frac{3}{2}(I_1^- I_{2z} + I_{1z} I_2^-) sin\theta cos\theta e^{i\phi}$$

$$E = -\frac{3}{4} I_1^+ I_2^+ sin^2\theta e^{-2i\phi}$$

$$F = -\frac{3}{4} I_1^- I_2^- sin^2\theta e^{2i\phi}$$

A and B terms may result in T_2 relaxation time decay. C, D, E and F terms are the causes of T_1 relaxation. Figure 2.6 shows spectral density versus natural log of frequency with different correlation times (τ_c). Spectral density can be expressed as $J(\omega) = \frac{2\tau_c}{1+(\omega\tau_c)^2}$. We

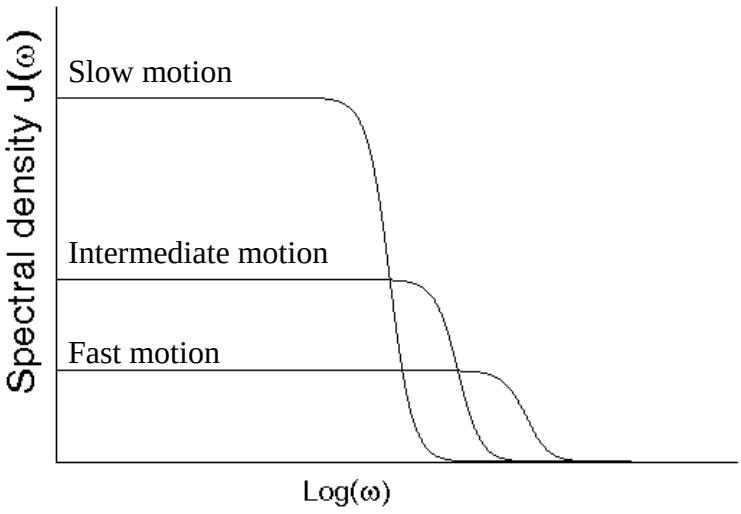

Figure 2.6. Spectral density at different molecular motion.

can describe correlation time as how fast one proton jumps into another site. Because protons always behave as one part of a molecule, we need to examine the behavior of molecules. In fact, all molecules have natural motions due to vibration, rotation and translation. Smaller molecules like water move rapidly. Fast molecular motion means a short correlation time or higher transition frequency. Larger molecules like proteins generally move slowly, showing a lower transition frequency. The T_1 relaxation time reflects the relationship between the frequency of these molecular motions and the resonance (Larmor) frequency.

Tumbling molecules create local magnetic field fluctuation as indicated in Figure 2.7. In Figure 2.7a, the hydrogen magnetic moments align to the applied magnetic field. This enhances total magnetic field strength. In case (b) and (c), there is no net effect because the hydrogen magnetic moments are perpendicular to B_o. In case (d), a water

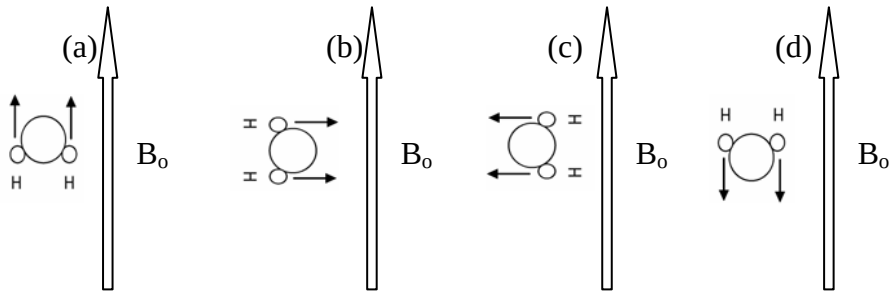

Figure 2.7. Water molecule tumbling

molecule imposes a negative effect on the applied field B_o. This is the reason that tumbling results in local magnetic field fluctuation.

Figure 2.8 displays the relationship between T_1 and correlation time (9). When correlation time is similar to inverse Larmor frequency, T_1 becomes minimum. For example, water molecules are small and move too rapidly to be efficient on T_1 relaxation. Similarly, large proteins move too slowly. T_1 values are longer for free water than for any other substance in the body (~4000 ms). When water molecules are bound or restricted, their correlation time may be close to the inverse Larmor frequency. The T_1 value of restricted water is therefore much shorter than that of free water.

Paramagnetic metal ions such as gadolinium and manganese are generally used as T_1 contrast agents to improve image contrast. They are typically chelated to an organic ligand to minimize the toxicity. For instance, free gadolinium can substitute for calcium in the body and be very toxic. Moreover, chelation also reduces their tumbling rates. The local magnetic field fluctuation created by tumbling macromolecules will stimulate longitudinal relaxation and shorten T_1 of water proton. For example, gadolinium is the most widely used paramagnetic ion because it has seven unpaired electrons, which can provide a high magnetic moment.

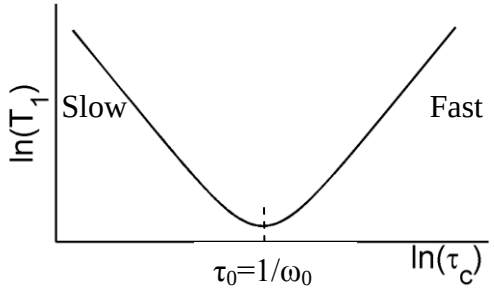

Figure 2.8. Variation of T_1 with the correlation time τ_c.

Signal enhancement requires direct interaction between unpaired electrons in the ion and water proton. Moreover, the coordination number in G_d^{3+} is estimated to be nine, where the coordination number means the number of atoms or ligands directly bonded to the metal center such as G_d^{3+}; A ligand is a molecule or atom bound directly to a metal center. The ligands are coordinated by valent bonds in which shared electron pairs are donated to the metal ion by the ligand. In Gd-DTPA (10), DTPA with eight coordination sites is a chelation ligand, and only eight of gadolinium's nine possible coordination sites could be filled. This leaves one open site to interact with water protons, as illustrated in Figure 2.9. In 1 mm^3 voxel, the molecule number for 1 mole water is about $3.3x10^{19}$, while the G_d number for 1 μM/L G_d-DTPA is $1.1x10^{16}$. The ratio between water molecules and G_d-DTPA in 1 mm^3 voxel is 3000. Although only a small fraction of the water can bind to G_d^{3+} at any one time, the bound fraction is in continual exchange with the free water, so that the T_1-shortening effect is distributed throughout the bulk fluid. This results in an enhancement of signal on T_1 weighted images.

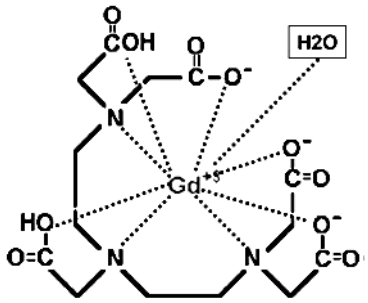

Figure 2.9. Molecular structure of Gd-DTPA. Gadolinium ion ($Gd^{3+)}$ in the chelate has nine coordination sites (dotted lines), five with carboxyl groups and three with amino nitrogen atoms. The remaining vacant site is coordinated with a water molecule (H_2O)

2.1.3.2 T_2 Relaxation Time

Spin-spin relaxation time (T_2) is a measure of how long transverse magnetization would maintain its coherence in a perfectly uniform external magnetic field. It is associated with a loss of spin phase and is seen as a transverse signal decay after the initial excitation. This spin-spin relaxation mechanism results from spin diffusion. In the previous section, dipole-dipole interaction was introduced as a possible cause of T_2 decay that does not involve a transfer of energy between resonating spin system and lattice environment. The spin-spin relaxation decay can arise from the fact that the protons themselves are slightly magnetic, which can exchange magnetization or the spread in precession rate due to diffusive movement of spins in microscopic magnetic field inhomogeneities.

Another important mechanism is magnetic field inhomogeneity, which can be induced by two sources. One results from the nonuniform magnetic field (B_o) due to magnet design. The other is due to the local field inhomogeneity as tissue magnetic properties can vary across tissue boundaries. These fixed field inhomogeneities can be recovered by applying an 180^o RF as in spin echo, while the signal decay from spin

diffusion cannot be recovered. A new time constant T_2^* is introduced which is defined as the combination of T_2 decay plus the local field inhomogeneity induced decay.

$$\frac{1}{T_2^*} = \frac{1}{T_2} + \Delta\omega \qquad (2.5)$$

Here $\Delta\omega$ describes the frequency distribution generated by local magnetic field inhomogeneity. Figure 2.10 shows the relationship between T_2 and correlation time (11,12). The correlation time decreases with the increased temperature. So T_2 relaxation time is longer. For instance, free water molecules move too rapidly to be efficient on T_2 relaxation. Any local field inhomogeneities experienced by a proton average to zero over a short period of time. Conversely, for those protons in membrane lipids and most macromolecules, molecular motions are extremely slow. A slowly fluctuating or "static" local magnetic field with respect to the Larmor frequency is generated by these molecules. Figure 2.11 demonstrates the relationship between interaction energy and the relative distance of two magnetic dipole moments (9). Protons near the macromolecule experience a local magnetic field gradient. The protons' spin temporarily resonate at a slightly different frequency and therefore gain or lose phase compared to other spins.

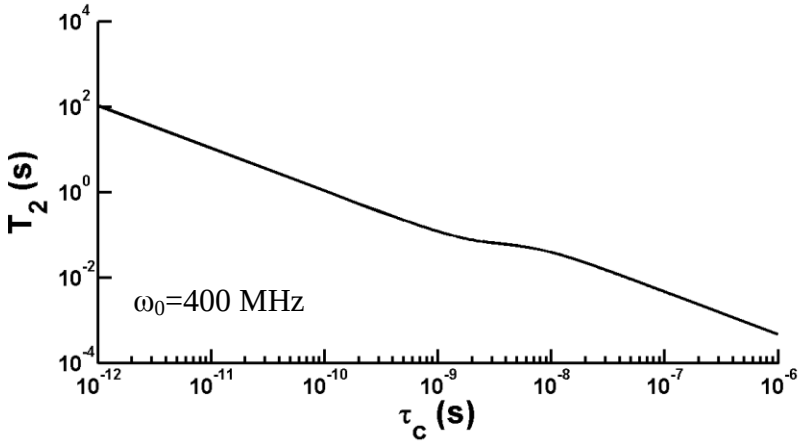

Figure 2.10. The relationship between T_2 and correlation time.

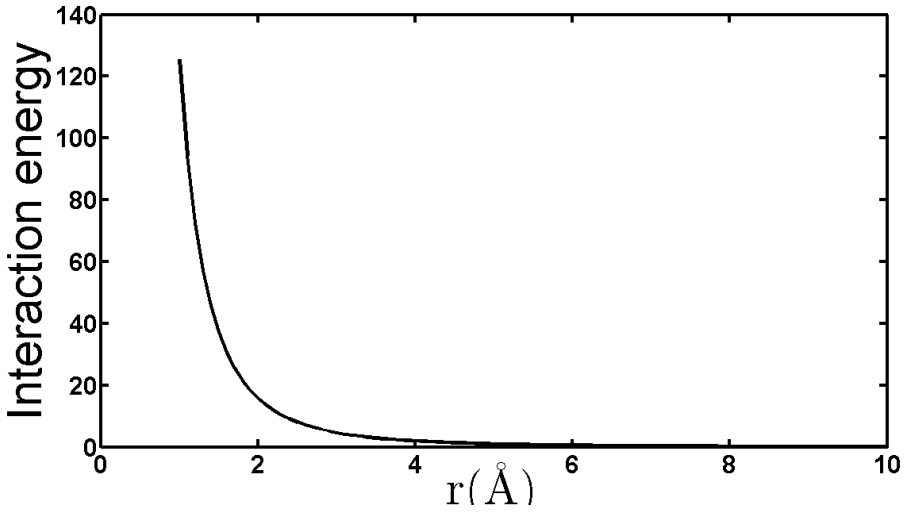

Figure 2.11. The relationship between interaction energy and relative distance of two dipole moments.

Different contrast agents can show different influence on T_1 and T_2 weighted images. Chemical compounds, which include gadolinium and manganese, primarily shorten T_1 of water and produce enhancement on T_1-weighted images, while superparamagnetic particles mainly shorten T_2/T_2* relaxation time of water and decrease signal intensity on T_2-weighted images. Since superparamagnetic particles have much stronger magnetic moments than individual paramagnetic ions (13) and thereby alter the magnetic field over a much longer range, they result in rapid dephasing of water protons which leads to a strong signal decay on T_2/T_2* weighted image.

2.1.4 Quantum Description

One spin with spin magnetic moment $\vec{I}$ is placed in a static magnetic field, H_0. m is the eigenvalue of the z-component of spin $\vec{I}$. The interaction energy of spin and magnetic field is defined as:

$$E_m = -\gamma\hbar H_0 m \tag{2.6}$$

Correspondingly, the solution for this system to the time-independent Schrödinger equation is

$$\varphi(t) = \sum_{m=-I}^{I} c_m u_m e^{-\frac{i}{\hbar}E_m t} \tag{2.7}$$

where u_m is an eigenfunction of the time-independent Schrödinger equation. c_m is a complex contant. Its square of absolute value is the probability of finding the state occupied. The expectation value of the x component of spin magnetic moment is found:

$$\langle\mu_x\rangle = \langle\varphi(t)|\mu_x|\varphi(t)\rangle = \langle\varphi(t)|\gamma\hbar I_x|\varphi(t)\rangle \tag{2.8}$$

For a proton, the spin quantum number is ½. Since I_x is half of the summation of the raising and lowering operator, the diagonal elements of matrix I_x vanish. Substituting Eq. (2.7) into Eq. (2.8), we get

$$\langle\mu_x\rangle = \gamma\hbar\left[c_{1/2}^* c_{-1/2}\left\langle\frac{1}{2}\middle|I_x\middle|-\frac{1}{2}\right\rangle + c_{-1/2}^* c_{1/2}\left\langle\frac{1}{2}\middle|I_x\middle|-\frac{1}{2}\right\rangle\right] e^{-i\gamma H_0 t} \tag{2.9}$$

We define $c_{1/2} = ae^{i\alpha}$ and $c_{-1/2} = be^{i\beta}$, where a and b are two real, positive numbers. α and β are also two real numbers. Because the total probability should be 1, $a^2 + b^2 = 1$. The result of Eq. (2.9) is written as below:

$$\langle\mu_x\rangle = \gamma\hbar ab\cos(\alpha - \beta - \omega_0 t) \tag{2.10}$$

Similarly, we derive

$$\langle\mu_y\rangle = -\gamma\hbar ab\sin(\alpha - \beta - \omega_0 t) \tag{2.11}$$

$$\langle\mu_z\rangle = \gamma\hbar\frac{a^2 - b^2}{2} \tag{2.12}$$

If we define $\phi = \beta - \alpha - \omega_0 t$ and $a^2 = \frac{1+\cos\theta}{2}$, Eqs.(2.10), (2.11) and (2.12) are rewritten as

$$\langle \mu_x \rangle = \frac{\gamma\hbar}{2} \sin\theta \cos\phi,$$

$$\langle \mu_y \rangle = \frac{\gamma\hbar}{2} \sin\theta \sin\phi \tag{2.13}$$

$$\langle \mu_z \rangle = \frac{\gamma\hbar}{2} \cos\theta$$

Eq. (2.13) is similar to a vector that rotates around the direction of H_0. The z-component of the spin magnetic moment is either parallel or antiparallel to the field orientation. However, its expectation value can take any value between $\frac{\gamma\hbar}{2}$ and $(-\frac{\gamma\hbar}{2})$ along any orientation depending on a choice of a and $(\alpha - \beta)$. For a system that consists of many spins, each spin has its own individual combination of a and $(\alpha - \beta)$. There is no reason that a spin prefers a certain $(\alpha - \beta)$. In other words, there is random $(\alpha - \beta)$ distribution. The net result is zero transverse magnetization. However, longitudinal magnetization is nonzero. Here, if we introduce a short duration RF field oscillating at the resonance frequency, the effect of this $\vec{H}_1$ field induces the rotation of total magnetization. Then the $\vec{H}_1$ field is switched off. Total magnetization $(\vec{M})$ time evolution obeys Bloch Equation:

$$\frac{dM_z}{dt} = \frac{M_0 - M_z}{T_1} - \gamma(\vec{M} \times \vec{H})_z \tag{2.14}$$

$$\frac{dM_x}{dt} = \gamma(\vec{M} \times \vec{H})_x - \frac{M_x}{T_2} \tag{2.15}$$

$$\frac{dM_y}{dt} = \gamma(\vec{M} \times \vec{H})_y - \frac{M_y}{T_2} \tag{2.16}$$

Here $\vec{H}$ stands for total magnetic field, which is the vector summation of $\vec{H}_0$ and $\vec{H}_1$. To simplify the calculation, a rotating frame is introduced. The relationship between laboratory frame and the rotating frame is described by

$$\frac{d\vec{M}}{dt} = \frac{d\overrightarrow{M'}}{dt} + \vec{\Omega} \times \vec{M} \tag{2.17}$$

where $\overrightarrow{M'}$ is the magnetization vector in the rotating frame. $\vec{\Omega}$, which is parallel to the external magnetic field, is the rotating frequency with respect to the lab frame. $H_1^{'}\left[= \left(H_0 - \frac{\Omega}{\gamma}\right)\vec{k} + H_1\vec{\imath}\right]$ is the effective magnetic field in the rotating frame. From the above discussion, we can see that $\vec{M}$ will rotate around the $H_1^{'}$ field. If we turn on H_1 for a short time duration τ, the rotation angle is evaluated as $\theta = \gamma H_1^{'}\tau$. For instance, if Ω is exactly equal to γH_0, the magnetization rotates in the $y^{'} - z^{'}$ plane.

2.2 Magnetic Resonance Imaging Theory

This section primarily introduces signal collection, slice selection, frequency encoding and phase encoding and popular image techniques. In the signal collection device, coil sensitivity is determined by the principle of reciprocity (14) and the signal equation is derived. Slice selection focuses on how to implement spatial frequency selection. Phase encoding, readout design and coil selection are discussed in detail. In the end I will introduce several popular image techniques such as gradient echo, spin echo, and EPI acquisition.

2.2.1 Signal Collection

The fundamental signal in an MR experiment comes from the detection of electromotive force on the coil, while time-varying magnetization can generate time-varying magnetic flux inside the coil. An effective current density is generated due to the time varying magnetization (15) as

$$\vec{J} = \vec{\nabla} \times \vec{M} \tag{2.18}$$

A magnetic field related to this current density is expressed as

$$\vec{B} = \vec{\nabla} \times \vec{A} = \vec{\nabla} \times \left(\frac{\mu_0}{4\pi} \int d^3 r' \frac{\vec{J}(\vec{r}')}{|\vec{r} - \vec{r}'|} \right) \tag{2.19}$$

The magnetic flux inside the coil is derived as

$$\phi = \int \vec{B} \cdot d\vec{S} = \int (\vec{\nabla} \times \vec{A}) \cdot d\vec{S} = \oint d\vec{l} \cdot \vec{A} \tag{2.20}$$

Finally we obtain the flux formula

$$\phi = \int d^3 \, r \vec{B}' \cdot \vec{M} \tag{2.21}$$

where $\vec{B}'$ represents the magnetic field per unit of direct current flowing in the coil. Thus the voltage induced in the coil is

$$\begin{aligned} V(t) = -\frac{d\phi}{dt} = -\frac{d}{dt} [& \int B_x'(r) M_x(r,t) + \int B_y'(r) M_y(r,t) \\ & + \int B_z'(r) M_z(r,t)] \end{aligned} \tag{2.22}$$

In general, due to longer T_1 relaxation time, $M_z(r,t)$ is a slowly varying compared with transverse components of magnetization. The last term in Eq. (2.22) is dropped.

$$V(t) = -\int \left[B_x'(r) \frac{dM_x(r,t)}{dt} + B_y'(r) \frac{dM_y(r,t)}{dt} \right] d\vec{r} \tag{2.23}$$

In order to achieve M_x and M_y, we need to solve the Bloch equation that is described in the previous section 2.1.4 for free precession case. The solution is

$$M_{xy}(t) = M_{xy}(0) e^{-t/T_2} e^{-i\omega t} \tag{2.24}$$

Here $M_{xy} = M_x + iM_y$ and $M_{xy}(0)$ is referred to as the transverse magnetization immediately after an RF pulse. Substituting Eq. (2.24) into Eq. (2.23), we obtain

$$V(t) = \int \omega(r)\left|B'_{xy}(r)\right|\left|M_{xy}(r,0)\right| e^{-t/T_2(r)} \cos\left[-\omega(r)t + \varphi(r) + \frac{\pi}{2}\right] \tag{2.25}$$

where $B'_{xy}(r) = B'_x(r) + iB'_y(r)$ and $\varphi(r)$ is the total phase shift due to the reception phase angle and phase shift from RF excitation. Because the detection of a signal with very high frequency challenges our electronic device, a phase sensitive detection (PSD) technique is applied to lower the high frequency. Figure 2.12 shows a simple diagram of how PSD works. But for a single PSD, we cannot determine whether the isochromat is precessing clockwise or counterclockwise. The second PSD with 90 degree phase shift is added. Then we find

$$S(t) = V^1_{psd}(t) + iV^2_{psd}(t) = \omega_0 e^{i\pi/2} \int B''_{xy}(r) M_{xy}(r,0) e^{-i\Delta\omega(r)t}\, dr \tag{2.26}$$

where $B''_{xy}(r) = \left|B'_{xy}(r)\right| e^{-i\varphi t}$ and $\omega = \omega_0 + \Delta\omega$.

2.2.2 Slice Selection

Slice selection is accomplished by applying a RF pulse and a one-dimensional, linear magnetic field gradient. The magnetic field gradient creates position-dependent resonance frequency. Figure 2.13 shows that the imaged slice is defined by the condition

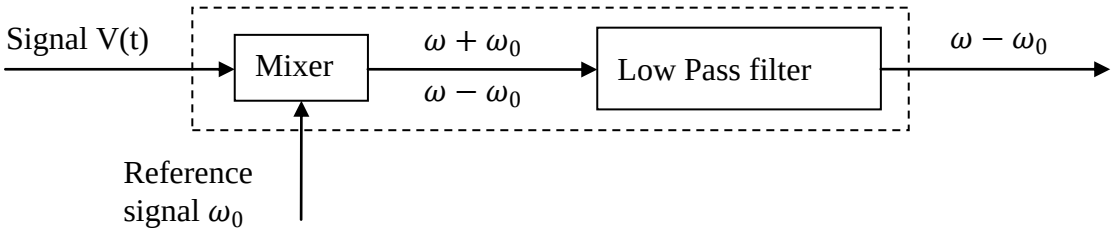

Figure 2.12. Phase sensitive detection.

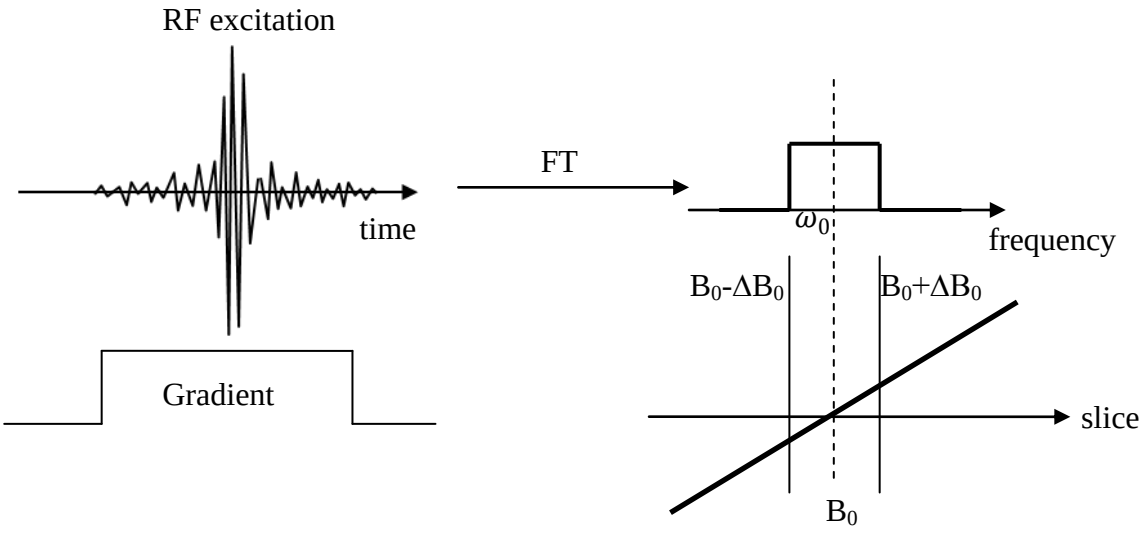

Figure 2.13. Slice selection diagram

$\omega_0 - \Delta\omega_0/2 < \gamma G_{ss} r_{ss} < \omega_0 + \Delta\omega_0/2$, where ω_0 is the offset frequency of the slice selection RF pulse, $\Delta\omega_0$ its bandwidth, and G_{ss} the slice-selection magnetic field gradient. The desired frequency needs to be translated to the waveform of the RF pulse in the time domain. Currently, there are two methods for selective pulse design. One is the Fourier transform approach. The key assumption about this method is that RF pulse waveform is the Fourier transform of the desired excitation profile. Because all RF pulses are multiplied by a window function in time and have finite length in the time domain, the Fourier transform of this modified RF pulse will be associated with a modified frequency distribution in Figure 2.14. The solution to this problem is to apply a Hanning filter on the RF pulse. The Hanning filter minimizes the Gibbs ringing artifact but broadens the slice profile. The Fourier method is very easy to implement for RF pulse design, but the resulting function is not accurate because spin system responds nonlinearly to RF excitation. However, solving the Bloch Equation provides another method to design RF pulses. During the derivation of solution, a small tip angle approximation is employed.

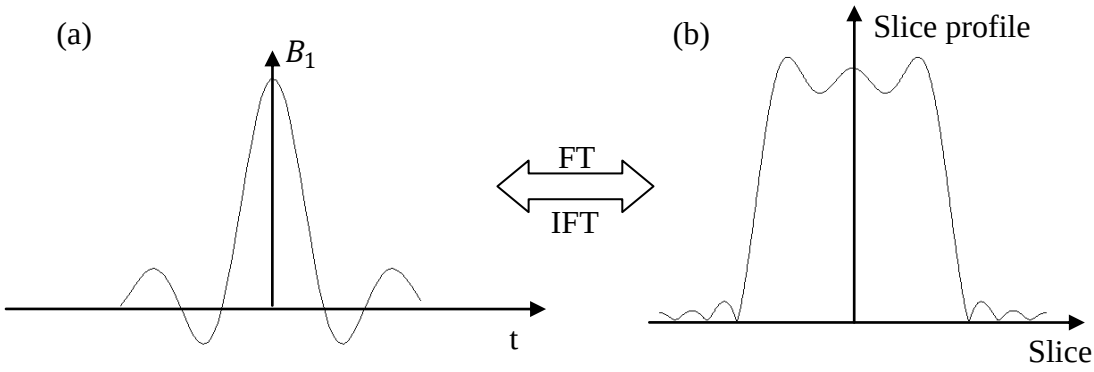

Figure 2.14. The diagram of slice excitation. (a) A sinc pulse modified by a window function and (b) its corresponding slice profile which suffers from Gibbs ring artifact.

Experiments demonstrate that the solution of Bloch Equation remains acceptable for flip angles up to 90^o.

2.2.3 Frequency Encoding

Frequency encoding is used to cause the resonance frequency to vary with spatial position. Within the slice-selected imaging plane, a small gradient is turned on to allow for spatial encoding in the readout direction. In Figure 2.15, the anterior part of the human head has a slightly lower resonance frequency than the posterior part. The signal acquired in the presence of a readout gradient is composed of components with frequencies from a narrow range, known as the signal bandwidth, around the Larmor frequency ω_0 at the center of the field–of-view. Each of the signal components is produced by spins from a certain location in the object. With the readout gradient along the x axis, the magnetic field that the object experiences after excitation is the homogeneous B_0 field plus another linear gradient field ($G_x x$). The resonance frequency versus position x is

$$\omega(x) = \omega_0 + \gamma G_x x \qquad (2.27)$$

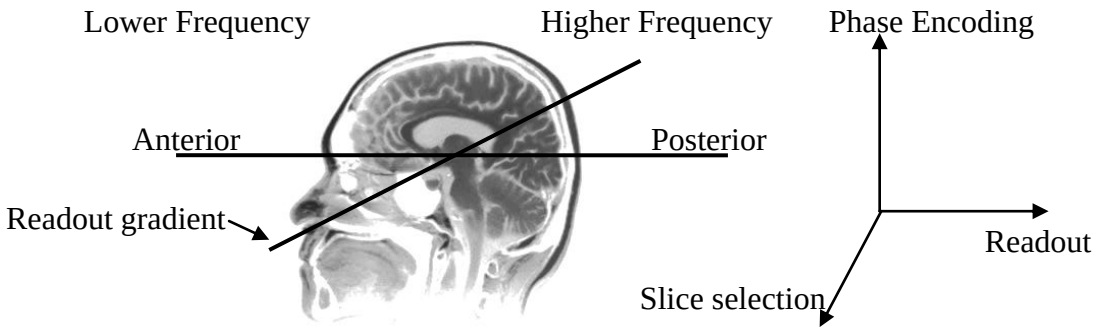

Figure 2.15. Frequency encoding diagram

In an infinitesimal interval dx at point x, neglecting the transverse relaxation effect, the acquired signal is proportional to

$$dS(x,t) \propto M(x)dxe^{-i\gamma(B_0+G_x x)t} \tag{2.28}$$

where $M(x)$ represents the position dependence of the transverse magnetization. To simplify the equation, we ignored the scaling constant. The signal equation becomes

$$dS(x,t) = M(x)dxe^{-i\gamma(B_0+G_x x)t} \tag{2.29}$$

The signal from the whole object is found as

$$S(t) = \int dS(x,t) = \int_{-\infty}^{+\infty} M(x)e^{-i\gamma(B_0+G_x x)t}dx \tag{2.30}$$

According to phase sensitive detection technique, the resulting signal becomes

$$S(t) = \int_{-\infty}^{+\infty} M(x)e^{-i\gamma G_x xt}dx \tag{2.31}$$

However, the number of sampling points is finite in the time domain, and the signal equation is rewritten as

$$S(n) = \int_{-\frac{L_x}{2}}^{\frac{L_x}{2}} M(x)e^{-ik_x(n)x} \tag{2.32}$$

where $k_x(n) = \gamma G_x \tau n$ and τ is sampling time interval in the readout direction and n stands for the n^{th} sampling time point. Total N samples of signal are collected from a

field-of-view L_x. Therefore, the inverse discrete FT of the signal will reconstruct M(x) with spatial resolution L_x/N.

$$L_x = 2\pi/\Delta k_x \tag{2.33}$$

According to the sampling theorem (16), a continuous function can be reconstructed fully from a series of discrete samples if the sampling time interval is not larger than $1/(2f_{max})$. f_{max} is the highest frequency of that continuous function. Otherwise, it will induce ghost artifacts in our image. Thus the relationship between signal bandwidth and readout gradient and field-of-view is expressed as

$$2f_{max} = \frac{\gamma G_x L_x}{2\pi} \tag{2.34}$$

2.2.4 Phase Encoding

The phase encoding gradient steps through k-space in a manner similar to the frequency encoding gradient. However, with frequency encoding, the transverse magnetization is recorded continuously while turning on the readout gradient. In contrast, phase encoding uses only a pulsed gradient field to move the magnetization to a particular location in k-space. Then the transverse magnetization signal is read out. From the phase encoding gradient, an extra phase term is introduced on the transverse magnetization

$$\varphi(y) = \gamma y \int_t^{t+T_y} G_y dt \tag{2.35}$$

where T_y is the duration of the gradient. As a result of frequency and phase encodings, the signal is calculated by 2D Fourier transform of the magnetization:

$$S = \iint M(x,y) e^{-ik_x(n)x + i\varphi(y)} dxdy \tag{2.36}$$

Substituting $k_y = \gamma \int_t^{t+T_y} G_y dt$ into the signal equation, we derive

$$S = \iint M(x,y) e^{-ik_x(n)x + ik_y y} dxdy \tag{2.37}$$

By altering the magnitude of phase encoding gradient step by step such as $G_y = m * G_{y0}$, the signal equation can be rewritten as

$$S(n,m) = \iint M(x,y) e^{-ik_x(n)x + ik_y(m)y} dxdy \tag{2.38}$$

where $k_y(m) = \gamma G_{y0} T_y m$. After all the phase encoding lines are acquired, an image can be reconstructed by the inverse discrete Fourier transform of $S(n,m)$. It is convenient to picture the behavior of spin while applying the slice selection, phase encoding gradient and frequency encoding gradient. A simple diagram is plotted in Figure 2.16.

Slice selection gradient and RF pulse work together to select an imaged slice layer. All the spins precess at the same frequency after applying the RF pulse when phase encoding gradient is turned on. Along the phase encoding direction, Larmor frequency is different. Spins own the different phase and have the same frequency again immediately after turning off phase encoding gradient. When frequency encoding gradient is on, along the readout direction, spin precesses at different Larmor frequency. At a certain time instant, spin phase exhibits spatial dependence.

2.2.5 Imaging Hardware

An MR scanner hardware scheme is demonstrated in Figure 2.17. The superconducting magnet produces a homogeneous magnetic field B_0. In Figure 2.17, a gradient coil generates a magnetic field gradient and results in linearly spatial dependence

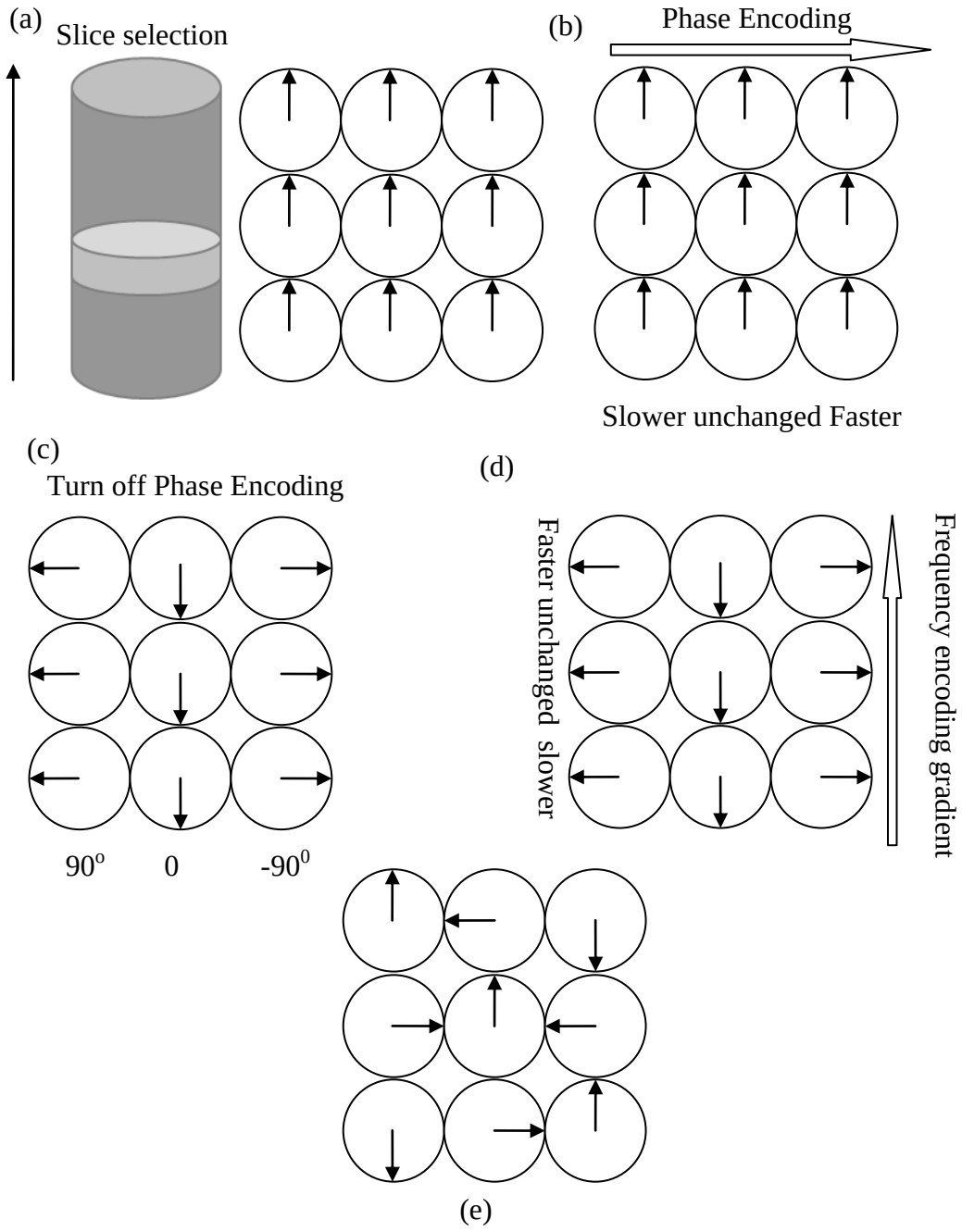

Figure 2.16. Spin precession diagram under various conditions.

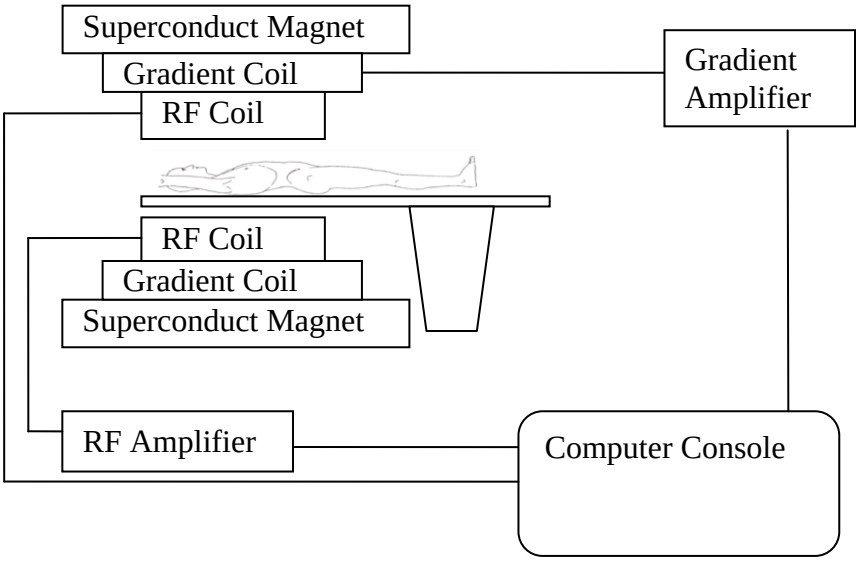

Figure 2.17. Hardware design overview of MR

of magnetic field. The famous gradient coil design is a Golay pair shown in Figure 2.18. This configuration creates a very linear field at the center plane.

RF coil is used to excite the imaged slice and acquire the desired signal. Based on its function, RF coil is grouped into three general categories: (1) transmit and receive coil, (2) receive only coil, and (3) transmit only coil. The transmit and receive coil both generate a B_1 field on the imaged object and collect signal from the object. A transmit coil serves as a B_1 field producer. A receive only coil is considered a signal detector. Based on geometric shape, RF coils can be defined as volume coils and surface coils. A volume coil is generally put around the object while a surface coil is placed on the surface of the object. Since the coil sensitivity is inversely proportional to $\frac{1}{r^3}$, where r represents the distance between coil and region of interest (ROI) location, signal intensity detected by the surface coil is nonuniform, which results from the inhomogeneous reception profile. However, the surface coil provides high sensitivity compared to a

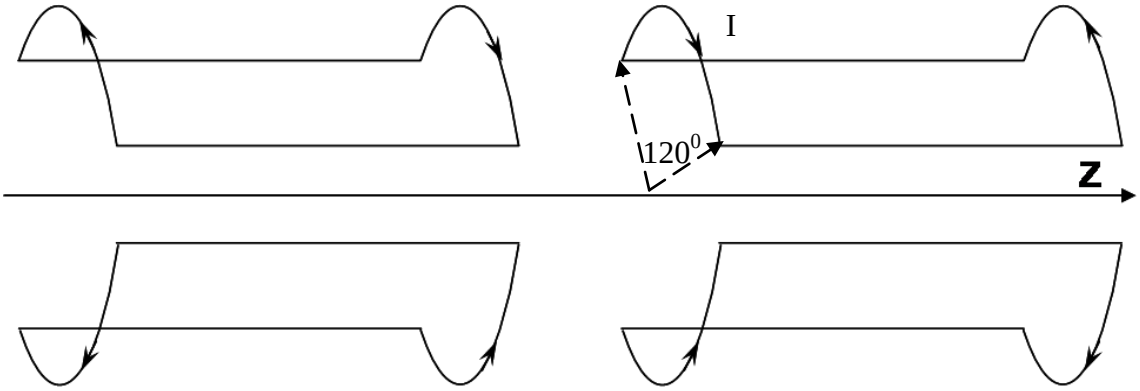

Figure 2.18. Golay pair

volume coil. A volume coil has a better RF homogeneity over a larger volume but lower SNR. The simplest surface coil is plotted in Figure 2.19a. The well-known volume coil is the birdcage coil (Figure 2.19b). In general, a volume coil is large enough to fit the whole body or part of body such as the head, wrist or knee. The transmit and receive switching scheme is demonstrated in Figure 2.20. During the transmission pulse, the receiver circuit is effectively shorted to ground. So the power is transmitted to the coil. Signal induced from the object is too small to bias the pin diode and is routed only to the receive path.

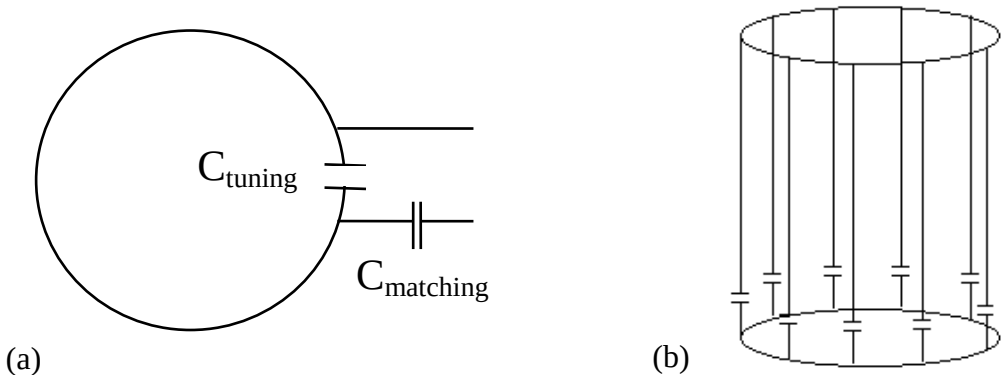

Figure 2.19. The diagram of typical RF coil. (a) Surface coil and (b) Birdcage coil.

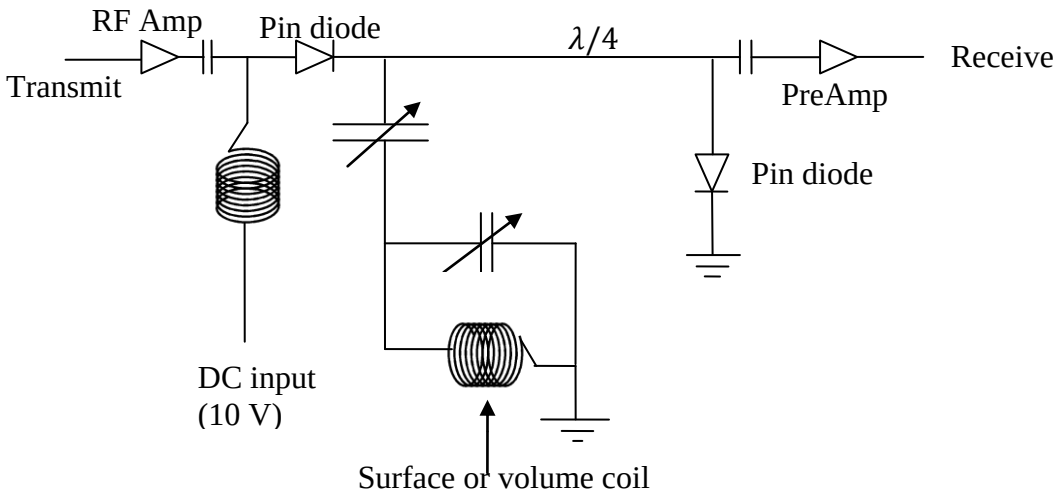

Figure 2.20. Circuit diagram of transmit and receive coil

2.2.6 Magnetic Resonance Imaging Techniques

To better understand MRI application, this section mainly introduces several basic imaging techniques such as free induction decay, gradient echo imaging, spin echo imaging and echo planar imaging (EPI) et al.

2.2.6.1 Free Induction Decay

Free induction decay (FID) is the observable NMR signal generated by non-equilibrium magnetization. Immediately after the sample is excited by an RF pulse, it starts to re-radiate the absorbed energy. If everything is perfect, signal decay can be predicted by T_2 relaxation time. However, in the real world, it is subject to T_2^* decay due to main magnet inhomogeneity and magnetic susceptibility of tissues. A sequence diagram is described in Figure 2.21. The primary application of FID pulse sequence focuses on NMR spectroscopy. Time domain signals are converted into frequency domain signals using Fourier transform.

$$f(\omega) = \int_{-\infty}^{+\infty} S(t) e^{-i\omega t}\, dt \tag{2.39}$$

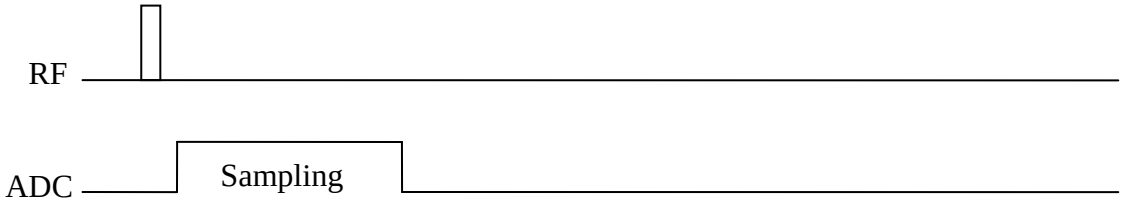

Figure 2.21. Free induction decay sequence diagram.

where $S(t)$ is the time domain signal, and $f(\omega)$ is its Fourier transformed complex signal. From classical mechanics, the relationship between object magnetization $\vec{M}(= M_x\vec{\imath} + M_y\vec{\jmath} + M_z\vec{k})$ and the applied magnetic field $H_0\vec{k}$ is given as

$$\frac{d\vec{M}}{dt} = \gamma\vec{M} \times H_0\vec{k} \tag{2.40}$$

The solution to Eq. (2.40) can be expressed by

$$\begin{aligned} M_{xy}(t) &= M_{xy}(0)e^{-i\gamma H_0 t} \\ M_z(t) &= M_z(0) \end{aligned} \tag{2.41}$$

where $M_{xy}(t) = M_x(t) + iM_y(t)$ and $M_{xy}(0) = M_x(0) + iM_y(0)$. Eq. (2.41) describes the clockwise rotation of magnetization about the applied magnetic field. Now, we apply another small magnetic field $\vec{H}_1$ (e.g., its magnitude of 50 mT) on the system to study the behavior of magnetization. A typical $\vec{H}_1$ field takes the following form:

$$\vec{H}_1(t) = H_1^e(t)e^{-i(\omega t+\varphi)}\vec{\imath} \tag{2.42}$$

where $H_1^e(t)$ means envelope function and ω is excitation frequency. If the initial phase angle φ is constant, there is no significant effect on our excitation. This phase can be neglected. Currently, many scanners use a quadrature coil to deliver the RF field. Quadrature detection mechanism provides two advantages. One is to improve signal to

noise ratio and the other is to reduce energy deposit (SAR). For an arbitrary $H_1^e(t)$, there is usually no closed-form solution for Bloch equation by substituting Eq. (2.40) into Eqs. (2.14), (2.15) and (2.16). In a spin system, there are many isochromats due to main magnetic field inhomogeneity and object magnetic susceptibility-induced field inhomogeneity. Isochromat refers to a group of spins resonating at the same frequency. In the first place, we excite on-resonance isochromat which resonates at ω_0. The terms related to T_1 and T_2 decay are dropped if the RF pulse duration is much shorter than T_1 and T_2. Now, Bloch Equation is altered from the laboratory frame to the rotating frame (17).

$$\begin{aligned} \frac{dM_{x'}}{dt} &= 0 \\ \frac{dM_{y'}}{dt} &= \gamma H_1^e(t) M_{z'} \\ \frac{dM_{z'}}{dt} &= -\gamma H_1^e(t) M_{y'} \end{aligned} \tag{2.43}$$

The solution of Eq. (2.43) is easily seen to be

$$\begin{aligned} M_{x'}(t) &= 0 \\ M_{y'}(t) &= M_0 \sin\left(\int_0^t \gamma H_1^e(t')dt'\right) \\ M_{y'}(t) &= M_0 \sin\left(\int_0^t \gamma H_1^e(t')dt'\right) \end{aligned} \tag{2.44}$$

where M_0 is the initial magnetization. Eq. (2.69) indicates the bulk magnetization that precesses about the x' axis in the rotating frame. In contrast to on-resonance excitation, if excitation frequency (ω) is different from that of isochromat, the Bloch equation is rewritten as

$$\frac{dM_{x'}}{dt} = \Delta\omega_0 M_{y'}$$

$$\frac{dM_{y'}}{dt} = -\Delta\omega_0 M_{x'} + \gamma H_1^e(t) M_{z'} \tag{2.45}$$

$$\frac{dM_{z'}}{dt} = -\gamma H_1^e(t) M_{y'}$$

where $\Delta\omega_0 = \omega_0 - \omega$. For a rectangular pulse, the magnitude of transverse magnetization of the solution to Eq. (2.45) is given as

$$M_{x'y'}(t_{RF}) = M_0 \frac{\omega_1}{\sqrt{\Delta\omega_0^2 + \omega_1^2}} \sqrt{sin^2\alpha + (1-\cos\alpha)^2 \frac{\Delta\omega_0^2}{\Delta\omega_0^2 + \omega_1^2}} \tag{2.46}$$

where $\omega_1 = \gamma H_1$, $H_1^e(t) = H_1 \prod\left(\frac{t - t_{RF}/2}{t_{RF}}\right)$, t_{RF} is the duration of RF pulse, and flip angle $\alpha = \sqrt{\Delta\omega_0^2 + \omega_1^2}\, t_{RF}$. Eq. (2.46) is plotted in Figure 2.22.

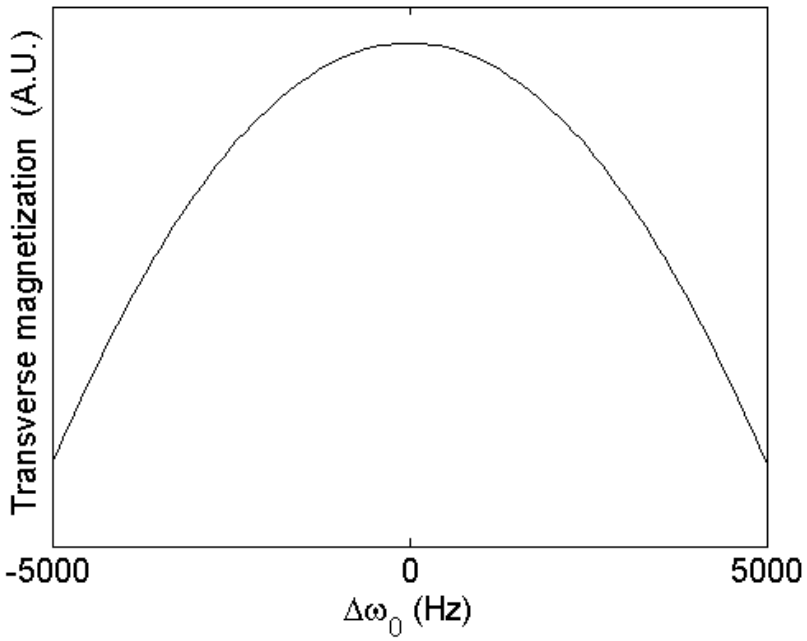

Figure 2.22. The relationship between transverse magnetization in rotating frame and off-frequency.

The prepared magnetization by RF pulse decreases as the off-frequency increases. If we do not drop T_1/T_2 related terms in the Bloch Equation, the x' and y' component of transverse magnetization can be achieved in the rotating frame. For a RF pulse duration greatly less than T_1 and T_2, the solution to Bloch equation can be written as (9),

$$M_{x'}(0) = \chi_0(\omega_0 T_2)\frac{(\omega_0 - \omega)T_2}{1 + (\omega - \omega_0)^2 T_2^2} H_1$$
$$M_{y'}(0) = \chi_0(\omega_0 T_2)\frac{1}{1 + (\omega - \omega_0)^2 T_2^2} H_1 \quad (2.47)$$

where ω_0 represents the Larmor frequency without H_1 field. χ_0 is the magnetic susceptibility of the sample without H_1 field, and ω is the excitation frequency of the H_1 field. After the RF field is switched off, the transverse magnetization continues to conduct precession in the rotating frame. It is subject to T_2 relaxation time decay. The motion is described by

$$M_{x'}(t) = (M_{x'}(0)\cos\Delta\omega t + M_{y'}(0)\sin\Delta\omega t)e^{-t/T_2}$$
$$M_{y'}(t) = (M_{y'}(0)\cos\Delta\omega t - M_{x'}(0)\sin\Delta\omega t)e^{-t/T_2} \quad (2.48)$$

where $\Delta\omega\ (= \omega_0 - \omega)$ is off-resonance frequency. If we define it as

$$M_{x'y'}(t) \equiv M_{x'}(t) + iM_{y'}(t) \quad (2.49)$$

then the transverse magnetization in the rotating frame is simplified as

$$M_{x'y'}(t) = e^{-i\Delta\omega t - \frac{t}{T_2}} M_{x'y'}(0) \quad (2.50)$$

The signal in the laboratory frame is

$$M_{xy}(t) = e^{-i\omega_0 t - \frac{t}{T_2}} M_{xy}(0) \quad (2.51)$$

A new variable is introduced to simplify the calculation.

$$M_{xy}(t) = \left|M_{xy}(t)\right| e^{i\varphi(t)} = M_{+}(t) e^{i\varphi(t)}$$

$$M_{+}(t) = e^{-\frac{t}{T_2}} M_{+}(0) \tag{2.52}$$

$$\varphi(t) = -\omega_0 t + \varphi(0)$$

From Eq. (2.23), signal induced in the coil is

$$V(t) = -\int B_{r,x} \frac{dM_x(\vec{r},t)}{dt} + B_{r,y} \frac{dM_y(\vec{r},t)}{dt} d\vec{r} \tag{2.53}$$

$$V(t) \propto \omega_0 V_{sample}\, M_{+}(0) B_{+} \sin\left(\omega_0 t + \theta - \varphi(0)\right) \tag{2.54}$$

where $M_{+}(0) = \sqrt{M_x^2(0) + M_y^2(0)}$, $B_{r,x} = B_{+}\cos\theta$, $B_{r,y} = B_{+}\sin\theta$ and V_{sample} is the sample volume. θ is the angle between the receive field and x-axis. Now the real part and imaginary part of the signal can be achieved by the multiplication of Eq. (2.54) by $\sin(\omega_0 - \Delta\omega)t$ and $\cos(\omega_0 - \Delta\omega)\, t$, respectively.

$$\begin{aligned} S(t) &= V(t)\sin(\omega_0 - \Delta\omega)t + iV(t)\cos(\omega_0 - \Delta\omega)\, t \\ &= \omega_0 V_{sample}\, e^{-t/T_2} M_{+}(0) B_{+} e^{-i[\Delta\omega t - \theta + \varphi(0)]} \end{aligned} \tag{2.55}$$

For an ideal case, $\theta = \varphi(0) = 0$. $\Delta\omega$=0 for on-resonance conditions.The real channel aligns with the direction of the x'-component of the transverse magnetization. Eq. (2.55) is rewritten as below.

$$\begin{aligned} S(t) \propto M_{+}(0) e^{-t/T_2} &= \sqrt{M_x^2(0) + M_y^2(0)}\, e^{-t/T_2} \\ &= \sqrt{M_{x'}^2(0) + M_{y'}^2(0)}\, e^{-t/T_2} \\ &= \chi_0(\omega_0 T_2) \frac{1}{\sqrt{1 + (\omega - \omega_0)^2 T_2^2}} H_1 e^{-\frac{t}{T_2}} \\ &= \chi_0(\omega_0 T_2) H_1 e^{-\frac{t}{T_2}} \end{aligned} \tag{2.56}$$

Eq. (2.56) and its Fourier transform are shown in Figure 2.23. It demonstrates that the real part of the spectrum would be in pure absorptive mode and the imaginary spectrum would be in pure dispersive mode (18). If off-resonance excitation occurs with $\theta = \varphi(0) = 0$ for a single isochromat, signal Eq. (2.56) is modified as

$$S(t) \propto \chi_0(\omega_0 T_2) \frac{1}{\sqrt{1+(\omega-\omega_0)^2 T_2^2}} H_1 e^{-\frac{t}{T_2}} e^{-i\Delta\omega t} \tag{2.57}$$

Eq. (2.57) and its Fourier transform are described in Figure 2.24. For a sample with two isochromats, the net signal results from a mixture of signal with two different off-resonance frequencies as shown in Figure 2.25. If the real channel and the imaginary channel don't align with the x' and y' component of transverse magnetization in the rotating frame ($\theta = \theta_0$) in Figure 2.26, both the real part and the imaginary part of the signal are a mixture of the x' and y' component. Fourier Transform of the real and imaginary part of the signal is not in pure absorptive and dispersive mode, respectively. For most cases, phase correction is performed on the real part of the signal and then spectrum curve-fitting is followed. Resonance peak line-shape is described by the Lorentzian function. In reality, each signal is a mixture of two modes. The dispersive contribution can be removed by "phase correction" to give purely absorptive signals. According to Figure 2.26, by altering the angle from θ to ψ, the pure absorptive signal can be calculated by this equation

$$\text{Absorptive}=S_{Real} * \cos\psi + S_{imag} * sin\psi \tag{2.58}$$

Here ψ is phase, which is a summation of phases induced by the initial RF pulse, receive field and instrumental error, respectively. If we assume that there is no phase error resulting from the instrument device. From Eq. (2.55), we derive

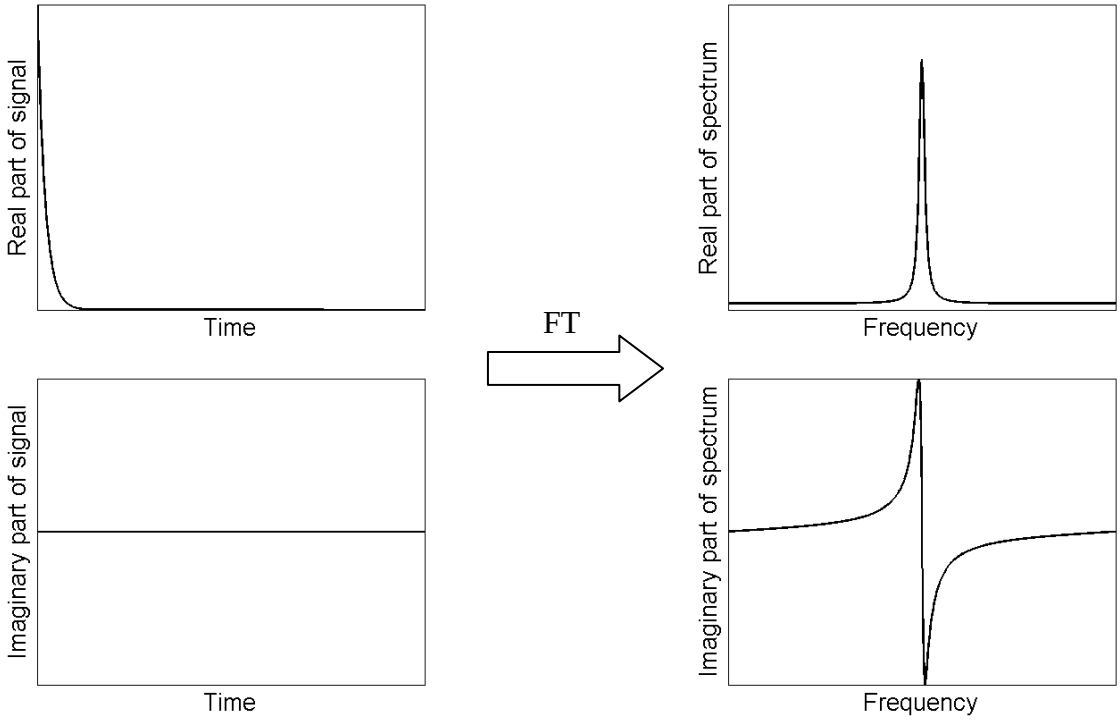

Figure 2.23. On-resonance signal and its Fourier transform.

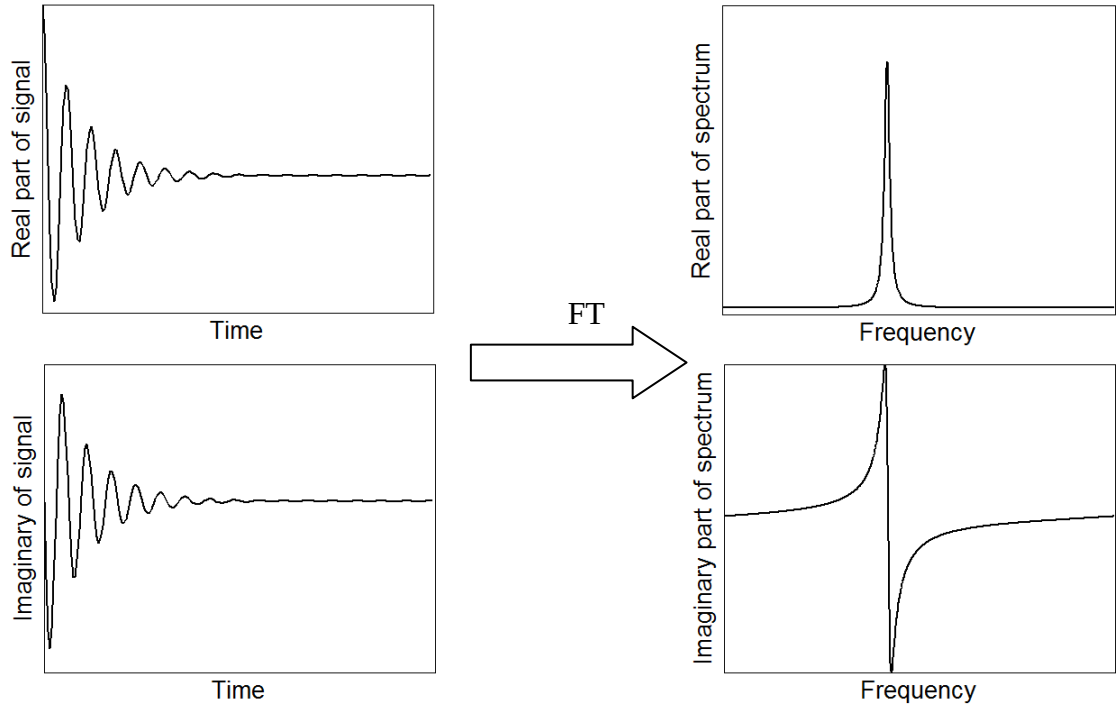

Figure 2.24. Single isochromat off-resonance excitation and its Fourier transform.

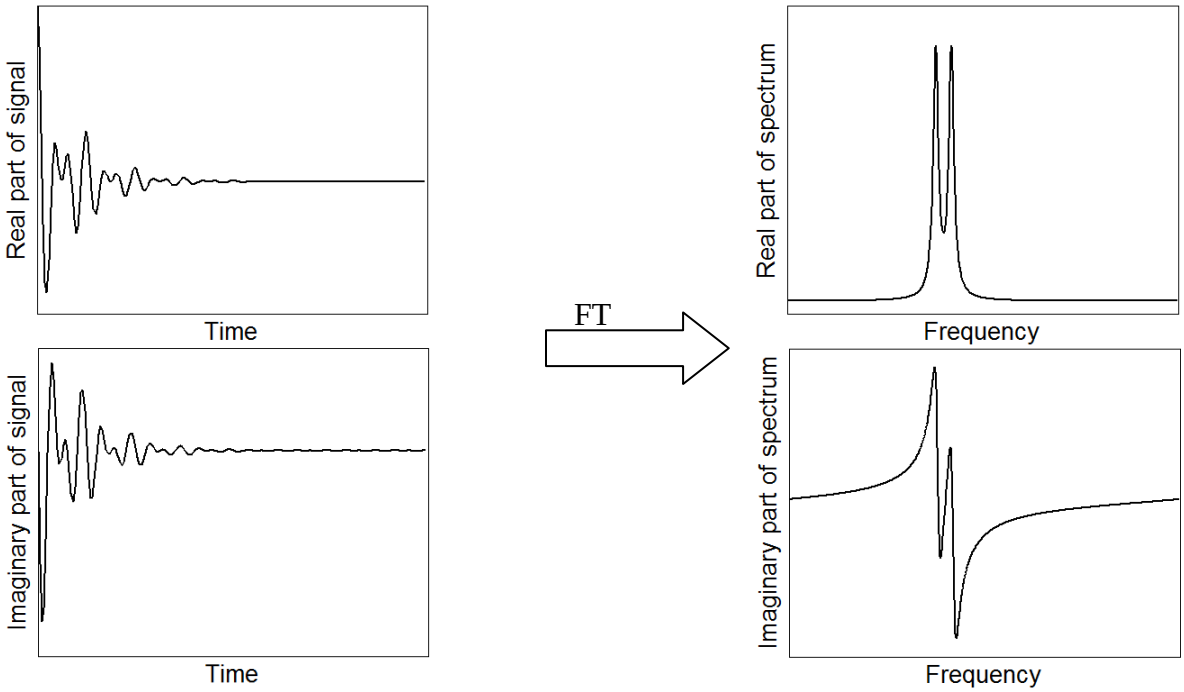

Figure 2.25. Off-resonance excitation with two different off-resonance isochromats.

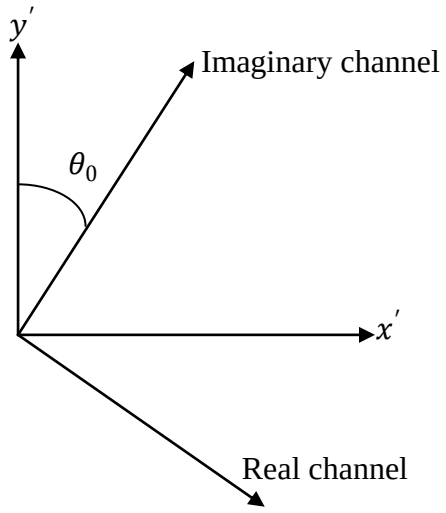

Figure 2.26. The relative position of real/imaginary channel with respect to transverse magnetization.

$$\psi = \theta - \varphi(0) \tag{2.59}$$

From the Eq. (2.46), we could compute $\varphi(0)$ (17)

$$\tan\varphi(0) = \tan\frac{\alpha}{2}\frac{\Delta\omega_0}{\sqrt{\Delta\omega_0^2 + \omega_1^2}} \tag{2.60}$$

Here α is a flip angle. Eq. (2.60) demonstrates that $\varphi(0)$ increases almost linearly with the frequency shift $\Delta\omega_0$. For example, one obvious source of off-frequency is chemical shift. So the FID signal modulated by phase ψ can be demodulated by

$$\psi = slope * \Delta\omega_0 + \theta \tag{2.61}$$

If we can determine slope and intercept in Eq. (2.61), the phase will be corrected to achieve a pure absorptive signal.

2.2.6.2 Gradient Echo Imaging

The basic pulse sequence for gradient echo imaging (GRE) consists of a partial flip angle excitation pulse and a slice selective gradient pulse G_z. At this point the spins are phased and precess at the same frequency. After the RF pulse, a phase encoding gradient would be implemented to generate position dependent phase along the phase encoding direction. Spins are still precessing with the same frequency. If a frequency encoding gradient is applied simultaneously or just after the phase encoding gradient, the spin resonance frequency becomes position dependent along the readout direction. To get a signal, we need an echo. Therefore we need to realign the spins. Spin refocusing can be realized by frequency encoding gradients as shown in Figure 2.27. The echo time (TE) is the time between the center of the RF pulse and the maximum of signal. The duration of phase encoding gradient (G_y) is τ_y. The frequency encoding gradient is applied along the readout direction. Readout sampling time is T_s. t' is the time relative to the peak echo

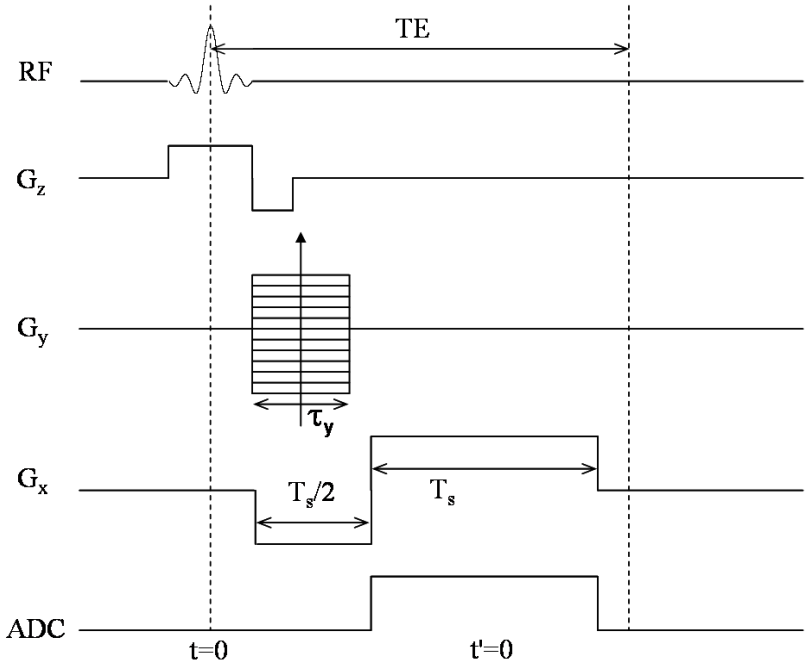

Figure 2.27. GRE pulse sequence

during the sampling period. The Analog to digital converter (ADC) is turned on to collect data during the period of T_s. If we turn on a 90^o RF pulse with the slice encoding gradient for a period, the immediate magnetization (M_{xy0}) on the transverse plane is equal to the equilibrium magnetization M_0. Then spins start to de-phase. If the phase encoding gradient is switched on, the additional phase is introduced, which is position dependent ($\gamma G_y \tau_y y$). Phase can be interpreted by k-space method

$$k_y(n\tau_y) = \frac{\gamma}{2\pi}\int_0^{\tau_y} nG_y(t'')dt'' = \frac{\gamma}{2\pi} nG_y(\tau_y)\tau_y \qquad (2.62)$$

where n is phase encoding steps. The frequency encoding gradient consists of de-phasing lobe and readout lobe. Then the echo is formed at the center of k-space. The frequency encoding gradient results in a resonance frequency depending on x-position. It is interpreted by k-space expression.

$$k_x(t) = \frac{\gamma}{2\pi}\int_0^t dt' G_x(t') = \frac{\gamma}{2\pi} G_x(t - TE) = \frac{\gamma}{2\pi} G_x t' \tag{2.63}$$

So the final image signal is expressed as

$$S(k_x, k_y) = \iint \rho(x, y) e^{-i2\pi(k_x x + k_y y)} dx dy \tag{2.64}$$

The signal is subject to T_2^* relaxation time decay. The flip angle induced by the RF pulse used in GRE is usually smaller than 90^0. The partial flip angle causes the magnetization to rotate only partly into the xy-plane. When the repetition time is shorter than T_1, the use of a partial flip angle can lead to higher signal intensity. The steady state longitudinal (M_z^{ss}) and transverse (M_{xy}^{ss}) magnetization are expressed in Eq. (2.65) and Eq. (2.66).

$$M_z^{ss} = \frac{M_0(1 - e^{-TR/T_1})}{1 - cos\alpha e^{-TR/T_1}} \tag{2.65}$$

$$M_{xy}^{ss} = \frac{M_0(1 - e^{-TR/T_1})}{1 - cos\alpha e^{-TR/T_1}} sin\alpha \tag{2.66}$$

Here α is flip angle and M_0 is the equilibrium magnetization. TR means time of repetition. The maximum signal intensity is given by the Ernst angle which is defined in Eq. (2.67).

$$cos\alpha_E = e^{-TR/T_1} \tag{2.67}$$

Short TR means short measurement time. With short TR we can achieve a stronger signal by reducing the flip angle.

2.2.6.3 Spin Echo Imaging

Gradient echo imaging is subject to T_2* relaxation decay which is caused by main field inhomogeneity, chemical shift and magnetic susceptibility. In order to eliminate the effect on the image resulting from these imperfections, spin echo imaging was introduced as illustrated in Figure 2.28.

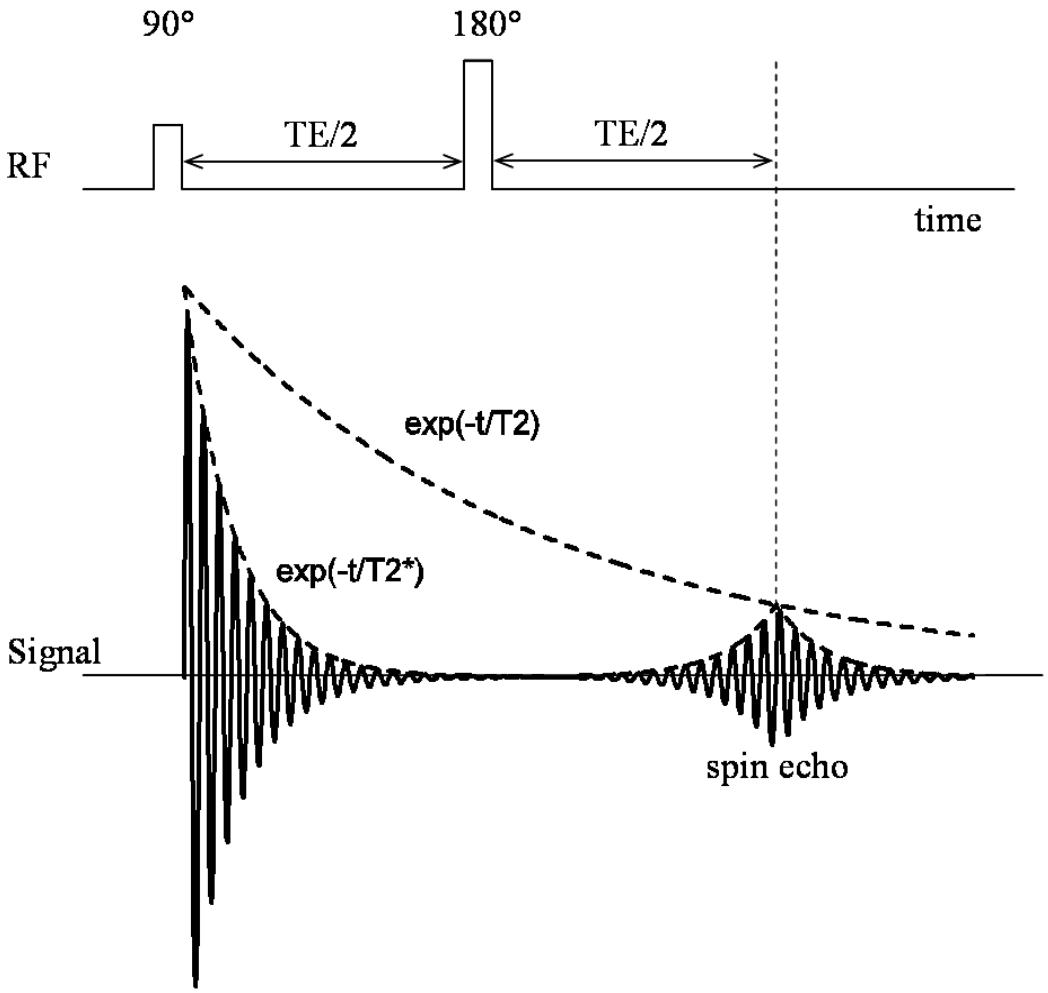

Figure 2.28. Spin echo signal

After the 90^0 RF pulse tips the magnetization to the transverse plane, the magnetization starts to de-phase due to imperfect field and spin-spin diffusion. Then another 180^0 RF pulse is applied to refocus the dephased spin. The pulse sequence design is illustrated in Figure 2.29. When we apply a 90^0 RF pulse to the sample, we switch on the slice encoding gradient to ensure the selection of a certain slice. Similarly, the 180^0 RF pulse and slice encoding gradient are turned on simultaneously to refocus the spins in the same slice excited by the 90^0 RF pulse. Following the 90^0 RF pulse, we implement the phase encoding on the phase encoding direction and dephasing lobe along the readout

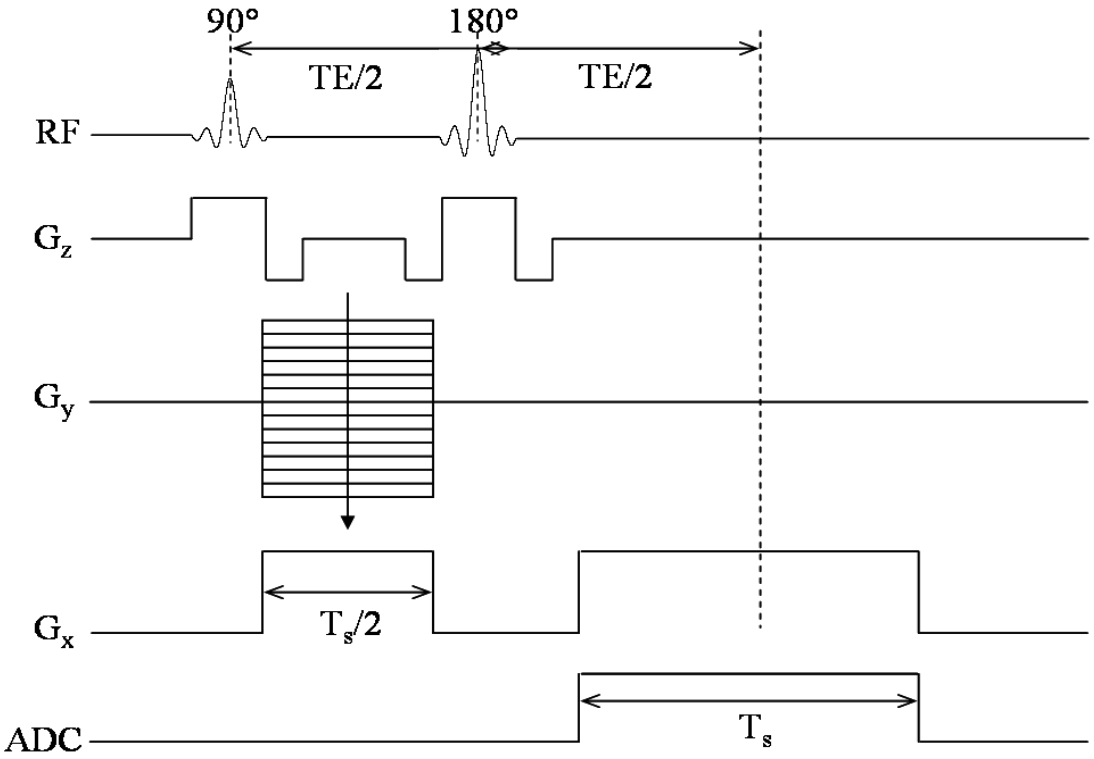

Figure 2.29. Spin echo pulse sequence

direction. Magnetization is modulated by the phase encoding gradient and frequency encoding dephasing lobe.

The readout dephasing lobe ensures that every k-space line starts from the most negative value to the most positive value. For each phase encoding line, we repeat the same process. Fourier transform can be performed from these k-space data.

From spin echo imaging, we can generate a T_2 weighted image. Spin magnetization evolves as shown in Figure 2.30. A 180^0 RF pulse along the y axis after a time τ flips the magnetization over in the x-y plane. The magnetization continues to evolve under the field inhomogeneity and is refocused at time 2τ. T_2 map can be made by fitting images with different echo times to the T_2 decay equation.

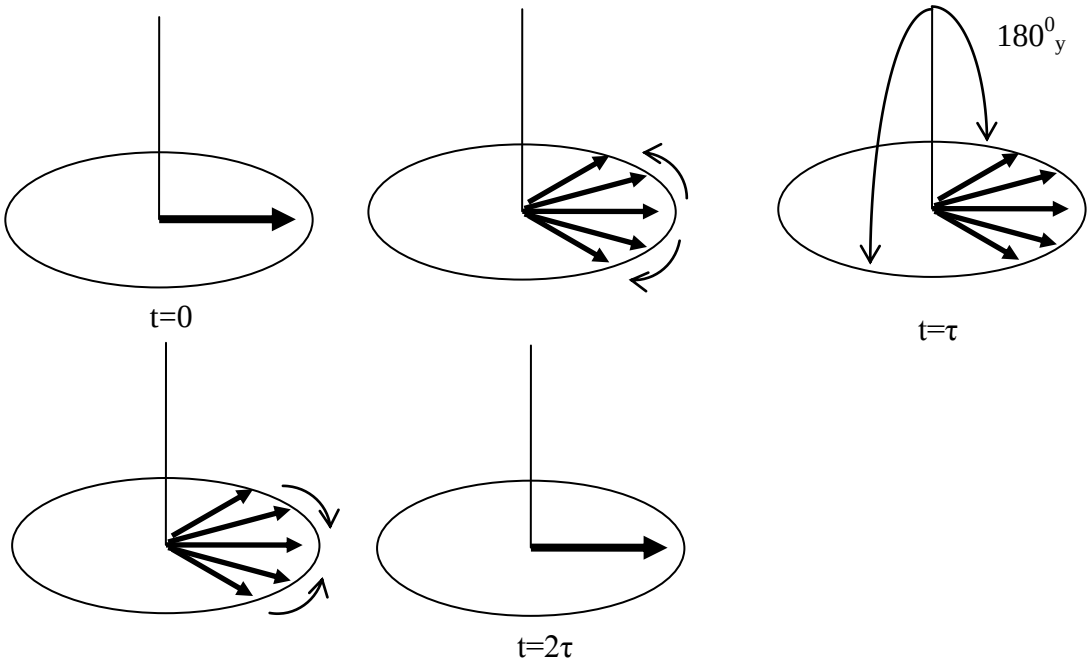

Figure 2.30. Magnetization evovles in the rotating frame due to field inhomogeneity (assuming no spin-spin diffusion).

Multiple echoes can be formed by using a series of 180^0 RF pulses as shown in Figure 2.31. The large number of 180^0 RF pulses gives rise to another problem because of imperfect 180^0 RF pulse. At different spatial positions, a given pulse will deviate from producing an exact 180^0 flip angle. This results in a reduced transverse magnetization after each subsequent 180^0 RF pulse. Meiboom-Gill made an improvement on a series of 180^0 RF pulse developed by Carr-Purcell (19). The key is to use a different axis for the initial 90^0 RF pulse excitation.

2.2.6.4 Stimulated Echo Imaging

In general, if we apply three pulses on the subject, five echoes can be generated: three conventional spin echos (SE_{12}, SE_{13} and SE_{23}), one secondary spin echo (SE_{123}),

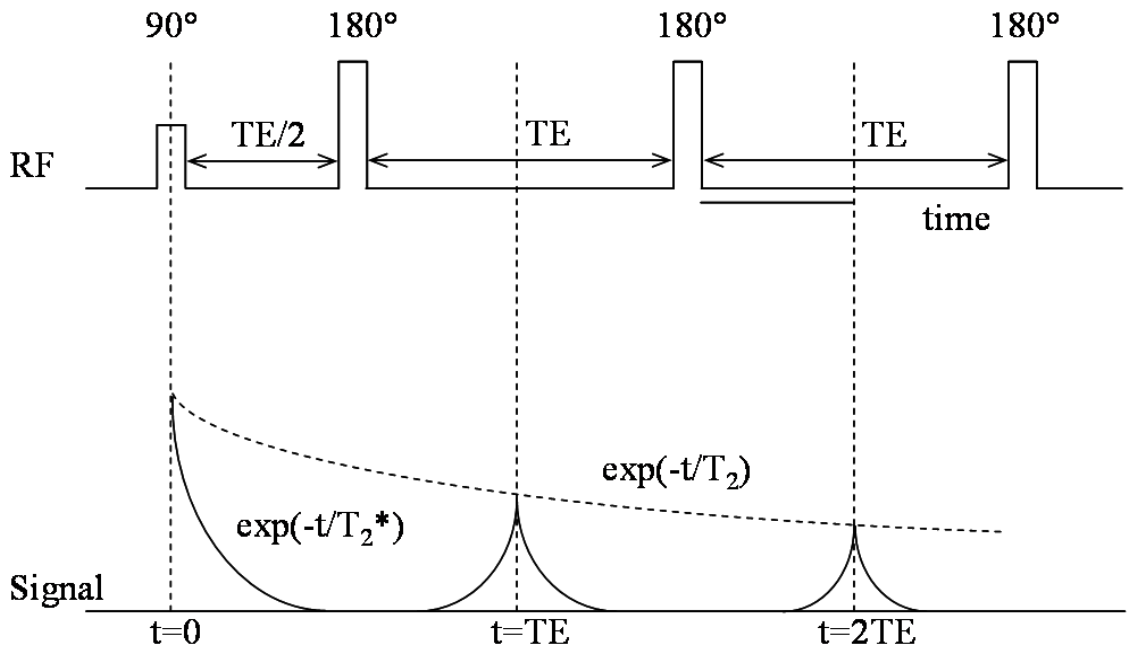

Figure 2.31. Multiple spin echo pulse sequence for measuring T_2.

and one stimulated echo (STE_{123}), as shown in Figure 2.32. α_1, α_2 and α_3 represent RF pulses with different flip angles. τ_1 is time interval between α_1 and α_2. τ_2 is time interval between α_2 and α_3. FID is referred to as free induction decay due to different RF pulses.

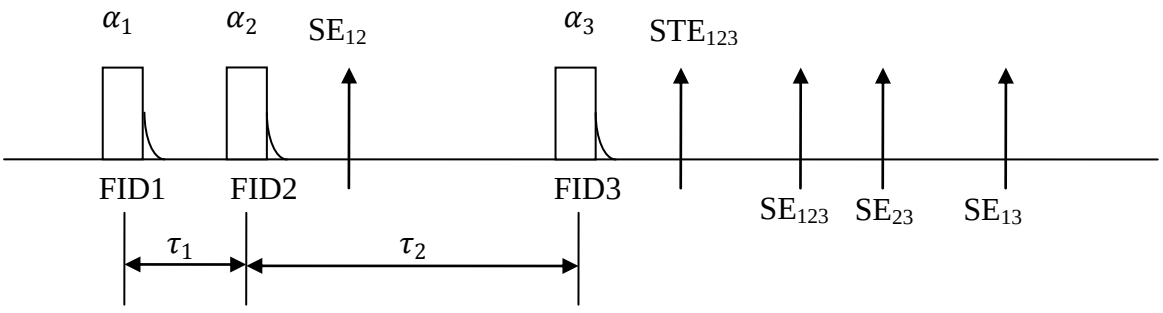

Figure 2.32. A train of three RF pulses generates three primary spin echoes, one secondary spin echo, and one stimulated echo.

FID1 generated by the 1st pulse is refocused by the 2nd pulse to form the 1st spin echo (SE_{12}). If FID1 is refocused by the 3rd pulse, the second spin echo (SE_{13}) is produced. The FID2 generated by the 2nd pulse is re-phased by the 3rd pulse to produce the spin echo (SE_{23}). Stimulated echo is formed by RF pulse 1, 2 and 3. If we take mirror action on SE_{12} with respect to the 3rd pulse, the secondary spin echo (SE_{123}) is yielded. The signal amplitude is listed in Table 2.2.

For stimulated echo imaging, we reject or spoil any other pathway of echoes except the stimulated echo. Because the signal is subject to the T_1 relaxation time decay, signal strength is improved compared to spin echo, which suffers from T_2 relaxation time decay ($T_2 << T_1$). In stimulated echo measurement, however, we throw away at least half of the excited magnetization. Due to its T_1 dependence property, we can measure T_1 map.

2.2.6.5 Echo Planar Imaging (EPI)

The echo planar imaging technique was first introduced by Peter Mansfield (20). Instead of measuring just one gradient echo after each excitation, multiple echoes are acquired. As long as the precessing magnetization in the transverse plane has not decayed away, it can be sampled. EPI has been widely applied in research fields such as function

Table 2.2. Signal amplitude from three pulses

Echo	TE	Amplitude
SE12	$2\tau_1$	$M_0 sin\alpha_1 sin^2\frac{\alpha_2}{2} e^{-2\tau_1/T_2}$
STE	$2\tau_1+\tau_2$	$\frac{1}{2} M_0 sin\alpha_1 sin\alpha_2 sin\alpha_3 e^{-\tau_2/T_1} e^{-2\tau_1/T_2}$
SE_{SE12}	$2\tau_2$	$-M_0 sin\alpha_1 sin^2\frac{\alpha_2}{2} sin^2\frac{\alpha_3}{2} e^{-2\tau_2/T_2}$
SE_{FID2}	$\tau_1+2\tau_2$	$M_0[1-(1-cos\alpha_1)e^{-\tau_1/T_1}] sin\alpha_2 sin^2\frac{\alpha_3}{2} e^{-(\tau_1+2\tau_2)/T_2}$
SE_{FID1}	$2\tau_1+2\tau_2$	$M_0 sin\alpha_1 cos^2\frac{\alpha_2}{2} sin^2\frac{\alpha_3}{2} e^{-(2\tau_1+2\tau_2)/T_2}$

MRI (fMRI), perfusion-spin tagging, diffusion tensor imaging and perfusion-dynamic susceptibility contrast. The spin echo EPI is illustrated in Figure 2.33.

EPI is very demanding on the hardware because strong field gradients have to be switched rapidly at the rate of about 1 kHz. Another shortcoming in EP images is the serious geometric distortion. Because ultra fast sequences place heavy demands on gradient amplitude and slew rate, gradient errors can cause significant image artifact. Gradient errors include inductive rise and fall time distortions from the desired waveform, and eddy currents induced on conductive surfaces of the magnet.

In Figure 2.34, (a) Rapid gradient switch leads to a modification of the ideal gradient shape due to inductance of the gradient coil. (b) Eddy currents modify the actual shape of the gradient pulse. Dotted lines in (b) represent the desired ramping-up gradient waveform. Solid lines show actual ramping-up waveform. Therefore, the echo is refocused with a slight delay. (c) In k-space, since back-and-forth trajectories are used between even and odd lines, the echo peaks are misaligned.

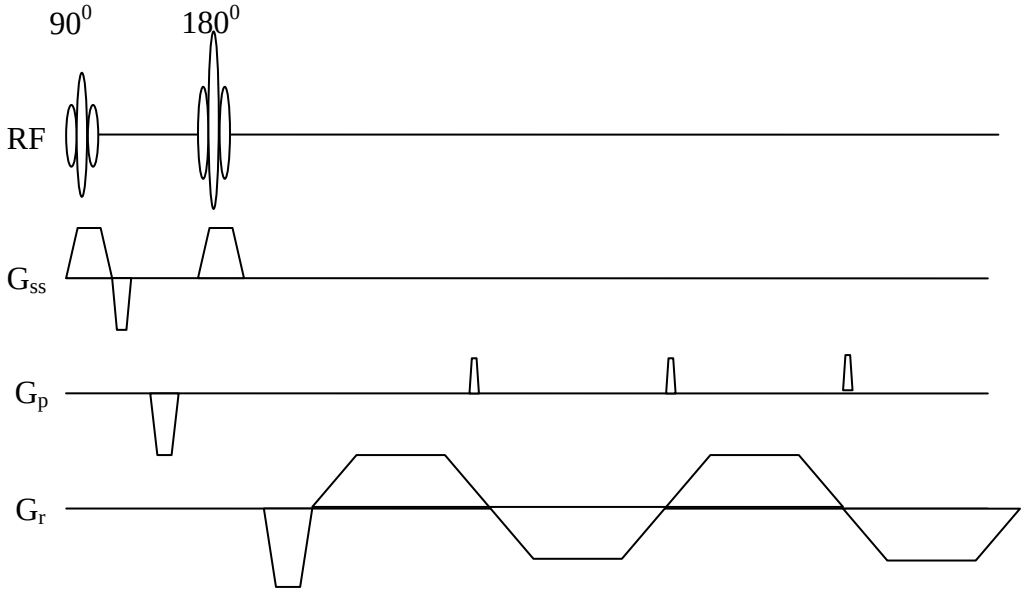

Figure 2.33. Spin echo EPI pulse sequence.

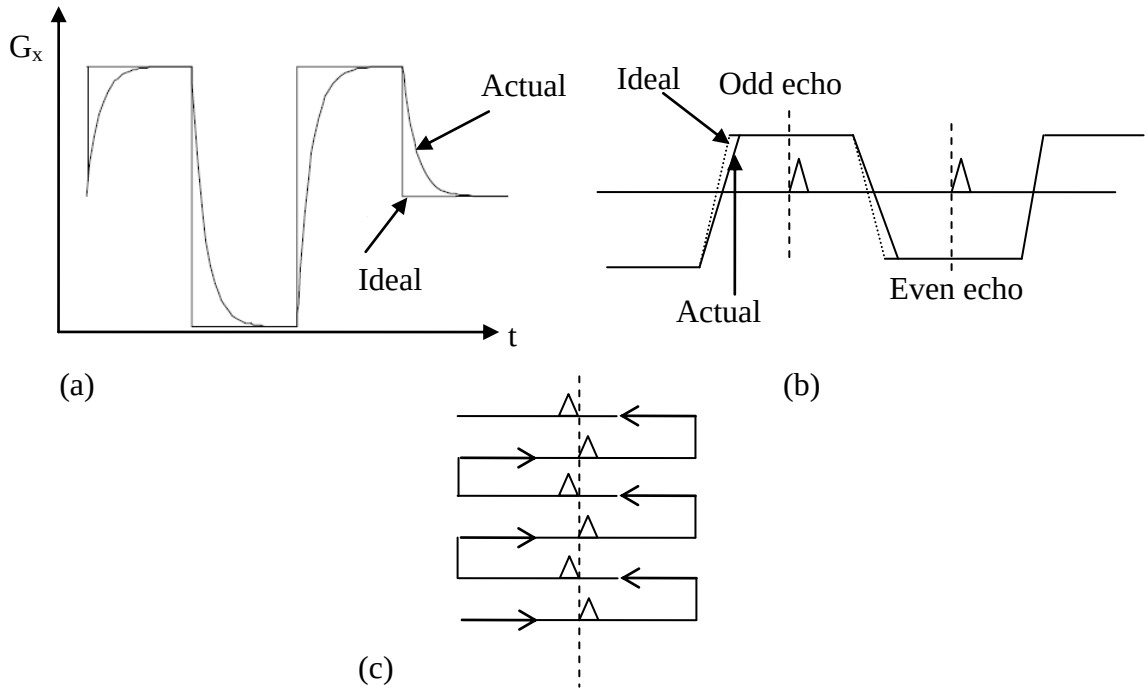

Figure 2.34. The diagram of gradient pulse shape. (a) Effects of coil inductance on actual shape of gradient pulse. (b) Eddy currents modify actual shape of the gradient pulse. The echo is refocused with a slight delay. (c) k-space trajectory

In order to resolve these problems, three reference lines are acquired without phase encoding and the correction of the EPI data is performed. The constant and linear phase corrections are calculated based on changes in echo position. Further, mechanical vibrations of the gradient coil system during readout in EPI can increase the temperature of the gradient system and alter the magnetic field distribution (21). This effect is enhanced by resonant modes of vibrations and results in apparent motion along the phase encoding direction. Before the EPI data are phase-corrected using reference scans, the phase induced by B_0 field drift must be corrected. Then data must be regridded due to ramp sampling. A rectangular matrix can be formed by zeropadding. Each even row is flipped and the reference scan is used to correct any constant and linear phase between even and odd lines. Filtering at the edge of k-space is applied to suppress Gibbs ringing artifacts caused by sampling truncation. If partial data is acquired, the Homodyne

correction (22) must be implemented to improve spatial resolution. Finally, we perform Fast Fourier Transform (FFT) and extract the magnitude image. This is a brief procedure for EPI data correction and ghost artifact reduction.

2.2.7 Image Reconstruction

In general, images are reconstructed from raw data acquired on Cartesian coordinates. The FFT is implemented on raw data. Because the data are discrete and finite, the images may suffer from all kinds of artifacts such as aliasing and Gibbs ringing. Based on the Nyquist theorem, the sampling rate should be at least twice the maximum spatial frequency in the object. In k-space explanation, the below relationship should be satisfied:

$$\Delta k = \frac{1}{FOV} \tag{2.68}$$

Δk is k-space interval between samples and FOV is the field of view along the readout or phase encoding direction. If FOV is larger than the scanned subject, no aliasing artifact appears in the reconstructed image. Otherwise, aliasing artifacts corrupt our image. There is another technique that can get rid of aliasing artifact due to smaller FOV compared to subject. It is called reduced FOV acquisition (23). Gibbs ringing artifact results from sharp signal change in the subject. When we apply an FFT on the data with dramatic signal change, a series of oscillations appear near sharp transitions. Usually, a Hanning filter applied to the edges of k space can be used to reduce Gibbs ringing artifacts. There are two different sampling methods. One is that sampling data are acquired in Cartesian coordinates. The other is that sampling data are not acquired in Cartesian coordinates. Thus we need to regrid these non-Cartesian data into a Cartesian grid. The next section will discuss the reconstruction of these two different data in detail.

2.2.7.1 Cartesian Grid Data Processing

For most cases, we deal with Cartesian sampling data. The advantage is that we can apply an FFT directly on data. However, there are still several problems such as longer acquisition time and sensitivity to motion. In order to improve scan time efficiency, researchers developed a partial data acquisition method and took advantage of the conjugate symmetry property of k space data. By postprocessing the data, the image can be reconstructed without loss of image resolution. Partial data acquisition is demonstrated in Figure 2.35. The solid line indicates the location of measured data. The dashed line shows the location of missing data in the conventional symmetric k-space coverage. In general, the partial data acquired is slightly more than half compared to full k-space coverage. In theory, most MRI images describe the spin density as a function of position, and therefore should be real value.

Based on this description and the Hermitian property of the Fourier Transform, half of the k-space data is enough to reconstruct an image. In reality, however, due to

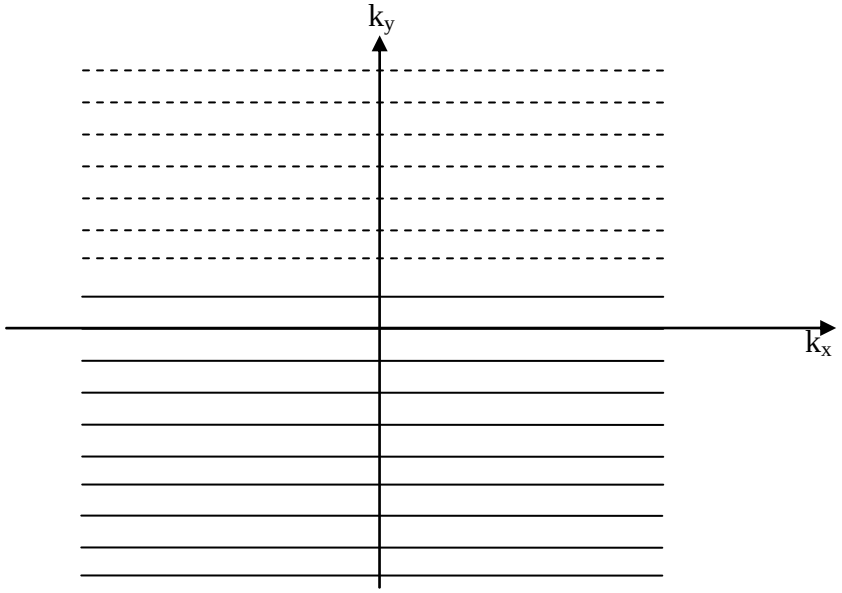

Figure 2.35. Partial data acquisition

phase errors from all kinds of sources such as motion, flow and field inhomogeneity, partial k-space reconstruction always requires some type of phase correction. When the phase correction is based on the sampling data, the technique is called Homodyne correction. The principle of this technique is to extract the phase from a low resolution image, assuming that the image phase slowly varies with spatial position. The conjugated phase is multiplied by the image reconstructed from direct inverse FFT of half k-space data. Then the inverse FFT is carried out on this modulated image. Using the conjugate property of k-space, we restore another half k-space. Figure 2.36 shows the flow chart of the Homodyne correction. Half of the k-space data can be regarded as the full k-space data multiplied by a window function. The window function is defined as

$$w(y) = \begin{cases} 1 & y > 0 \\ 0 & y < 0 \end{cases} \tag{2.69}$$

Half echo is expressed as $S_{half} = S_{full}\, w(y)$. If we apply inverse FFT on Eq. (2.69), the image would be reconstructed as below:

$$\begin{aligned} I_{half}(y) &= FFT^{-1}\left(S_{half}\right) \\ &= I_{true}(y) * \left[\frac{1}{2}\delta(y) + i\frac{1}{2\pi y}\right] \\ &= \frac{1}{2}|I_{true}(y)|e^{i\varphi(y)} + [|I_{true}(y)|e^{i\varphi(y)}] * \frac{i}{2\pi y} \end{aligned} \tag{2.70}$$

If $\varphi(y)$ slowly varies with spatial position, then Eq. (2.70) can be approximated by the equation:

$$I_{half}(y) = [\frac{1}{2}|I_{true}(y)| + |I_{true}(y)| * \frac{i}{2\pi y}]e^{i\varphi(y)} \tag{2.71}$$

The following expression demonstrates the image we calculate:

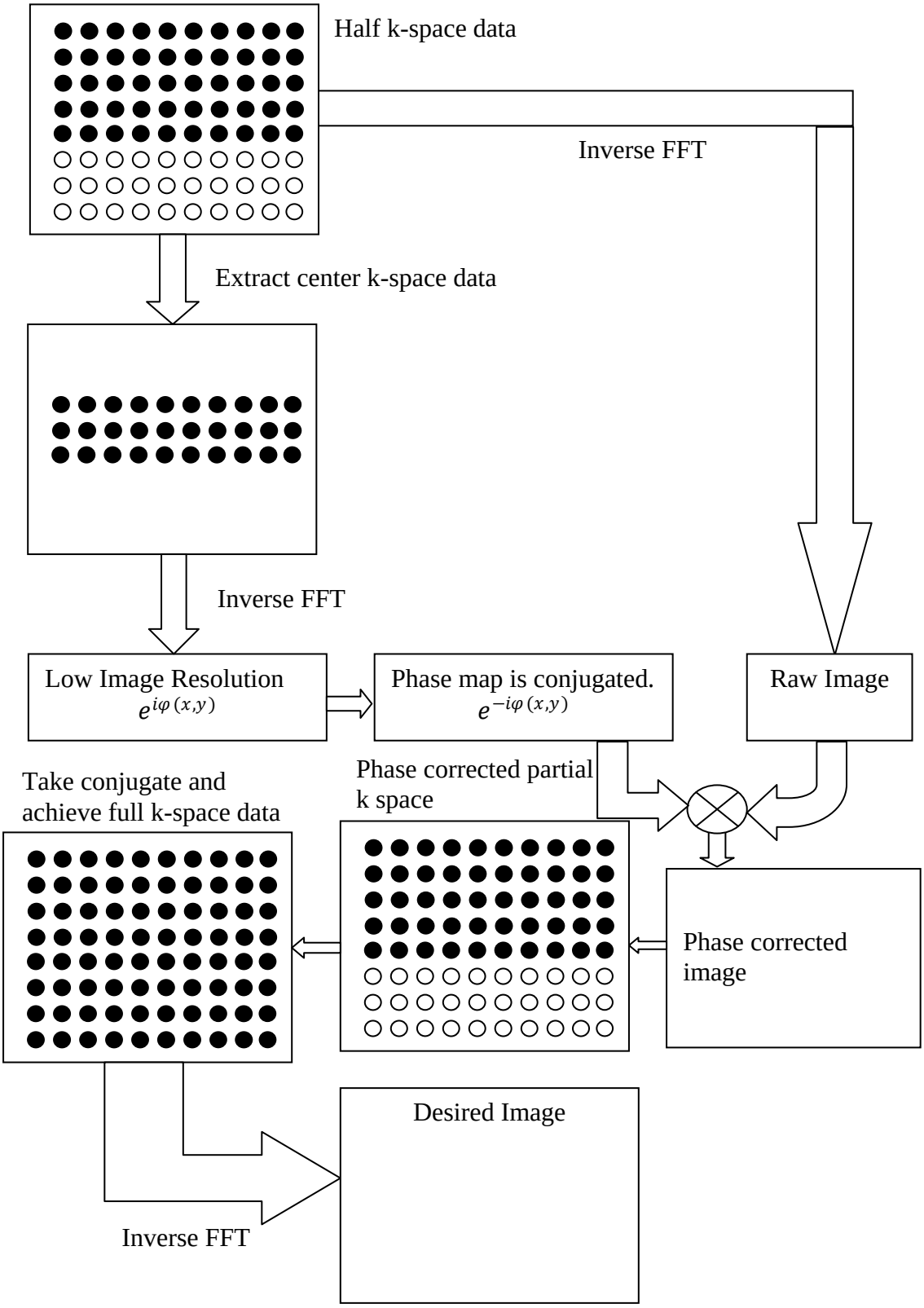

Figure 2.36. Homodyne flow chart.

$$I_{half}(y)e^{-i\varphi(y)} = \frac{1}{2}|I_{true}(y)|+|I_{true}(y)| * \frac{i}{2\pi y} \quad (2.72)$$

Then the real image is obtained from Eq. (2.72).

$$|I_{true}(y)| = 2RealPart\left[I_{half}(y)e^{-i\varphi(y)}\right] \quad (2.73)$$

Another method to improve scan time efficiency is to acquire a reduced set of phase encoding lines with multiple coil configuration. Correspondingly, the image will suffer from ghost artifact due to under-sampling data if there is no further postprocessing. Therefore, GRAPPA is one method introduced to achieve aliasing-free images. GRAPPA is referred to as generalized autocalibrating partially parallel acquisitions (24). It can recover the missing data of each coil using the RF coils for spatial encoding. A highly accurate field map is not necessary. The missing k-space lines can be calculated as a linear combination of several adjacent acquired lines. The weighting coefficients are computed from several full sampled k-space lines, which are called the auto-calibration signal (ACS) lines. Figure 2.37a demonstrates a k-space sampling scheme with reduction factor (R=2). Figure 2.37b shows that the data labeled by marked circle are used to fit ACS data (gray circle). In this example, four coils are applied. What we can obtain about the maximum R is 4. One open circle and one marked circle form a block. Here the total block number is 4. If we define the total block number as N_b, the signal of the gray circle from the i^{th} coil is expressed as:

$$S_i(k_{ACS}) = \sum_{j=1}^{N_c}\sum_{b=0}^{N_b-1} w(i,b,j,m)S_j(k_{ACS} + m\Delta k_y - bR\Delta k_y) \quad (2.74)$$

where N_c is the number of coils, w is the weighting coefficient and m is the offset of fitted line from the marked line. Since $w(i,b,j,m)$ is independent of ACS line, we can list a group of equations for different ACS lines and apply a least-squares method to

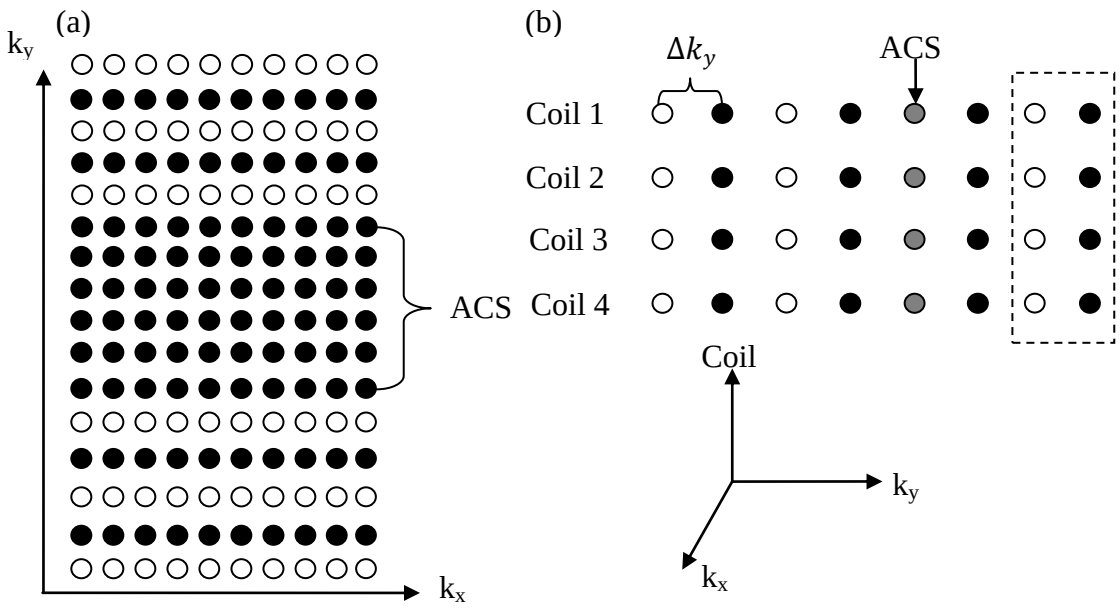

Figure 2.37. GRAPPA diagram. (a) K-space sampling with reduction factor 2. Marked circles indicate acquired data. Open circles represent missing data. (b) Gray circles are ACS data. Dashed box refers to one block.

solve those equations. $w(i,b,j,m)$ would be computed approximately. Then missing data can be calculated from adjacent acquired data using the weighting coefficients $w(i,b,j,m)$. Eq. (2.74) is rewritten as

$$S_i\left(k_{missing}\right) = \sum_{j=1}^{N_c} \sum_{b=0}^{N_b-1} w(i,b,j,m) S_j\left(k_{missing} + m\Delta k_y - bR\Delta k_y\right) \tag{2.75}$$

After we restore the missing data, we can perform direct FFT and reconstruct the image. The magnitude image is obtained by combining individual coil magnitude images using a sum of square (SOS) method.

2.2.7.2 Non-Cartesian Data Sampling

For non-Cartesian sampling, the most commonly used acquisition schemes are radial and spiral sampling. The k-space trajectory is given either by a set of radial lines starting from the origin of the coordinate system or by a set of interleaved spirals as shown in Figure 2.38. The disadvantage of non-Cartesian imaging is that it requires a multistep reconstruction process. The sampled data need to be gridded onto a Cartesian coordinate system. Moreover, density compensation should be applied to the uneven data distribution. The advantage is insensitivity to motion.

Here I briefly discuss the data gridding procedure (25,26). A 2D function $\rho(x, y)$ represents the spin density of the object in a certain slice. Its Fourier Transform can be written as

$$M(k_x, k_y) = \iint_{-\infty}^{+\infty} \rho(x, y) e^{-i2\pi k_x x - i2\pi k_y y} dxdy \tag{2.76}$$

We define sampling function for a sampling pattern as

$$S(k_x, k_y) = \sum_m \delta(k_x - k_{xm}, k_y - k_{ym}) \tag{2.77}$$

The sampled data are expressed in the equation:

$$M_s(k_x, k_y) = M(k_x, k_y) \cdot S(k_x, k_y) \tag{2.78}$$

Then the sampled data are convolved with a kernel function $C(k_x, k_y)$ and sampled into the Cartesian coordinate grid. * denotes the convolution

$$\begin{aligned} M_{scs}(k_x, k_y) = \{[M(k_x, k_y) \cdot S(k_x, k_y)] * C(k_x, k_y)\} \\ \cdot \mathfrak{M}(k_x, k_y) \end{aligned} \tag{2.79}$$

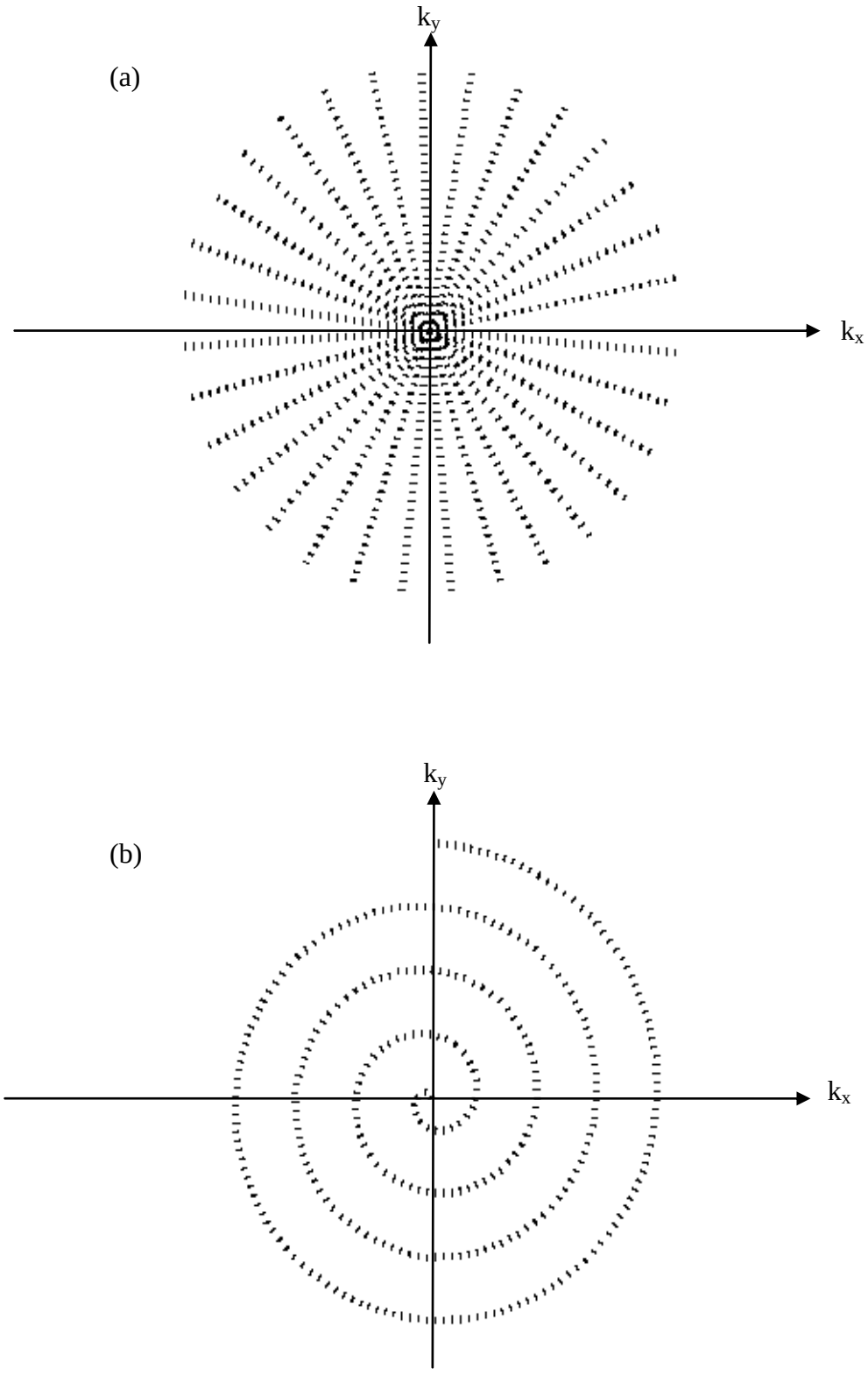

Figure 2.38. Sampling scheme. (a) Radial sampling (b) Spiral sampling

where $\mathfrak{M}(k_x, k_y)$ is a sum of two 2D equally spaced delta functions. Applying direct FFT on Eq. (2.79), we can reconstruct the image as the following equation:

$$I_{scs}(x,y) = \{[\rho(x,y) * S(x,y)] \cdot C(x,y)\} * \mathfrak{M}(x,y) \tag{2.80}$$

Considering the nonuniform sampling density, we can define P as density area function.

$$P(k_x, k_y) = S(k_x, k_y) * \ C(k_x, k_y) \tag{2.81}$$

Eq. (2.79) is modified as below.

$$\begin{aligned} M_{scs}(k_x, k_y) &= \left\{\left[\frac{M(k_x, k_y) \cdot S(k_x, k_y)}{P(k_x, k_y)}\right] * C(k_x, k_y)\right\} \\ &\quad \cdot \mathfrak{M}(k_x, k_y) \\ &= \left(\left\{M \cdot \left[\frac{S}{S * C}\right]\right\} * C\right) \cdot \mathfrak{M} \end{aligned} \tag{2.82}$$

The corresponding image is rewritten as

$$I_{scs}(x,y) = (\{\rho(x,y) * [S(x,y) *^{-1} (S \cdot C)]\} \cdot C) * \mathfrak{M}(x,y) \tag{2.83}$$

where $*^{-1}$ denotes de-convolution. For any convolution kernel function, we only perform finite convolution. Naturally, this introduces aliasing artifacts in the image. Any rolloff in the central lobe of C(x,y) will show the trend of attenuation toward the edge of image. In order to eliminate this effect, we directly divide Eq. (2.83) by C(x,y). The reconstructed image can be obtained in the following formula.

$$I_{recon}(x,y) = \frac{I_{scs}}{C(x,y)} \tag{2.84}$$

CHAPTER 3

IMPROVEMENT OF ACCURACY OF DIFFUSION MRI USING REAL-TIME SELF-GATED DATA ACQUISITION

Diffusion is a transport process which results in mixing or mass transport without requiring bulk motion. Especially in biological tissues, it has been shown to represent an important means of characterizing tissue properties. The diffusive movement resulting from the collision between water molecules and the surrounding medium is a fraction of the structure and geometry of the tissue at a microscopic level. As a result, diffusion reflects microscopic characteristics of the medium.

3.1 Introduction

Molecular diffusion refers to random translational motion of molecules resulting from collisions between molecules and structure in the tissue. Therefore, in a free medium, during a given time interval, molecular displacement obeys 3D Gauss distribution of mean zero. The variance of three dimensional diffusion displacements is given by (27):

$$\langle r^2 \rangle = 6Dt \tag{3.1}$$

The amount of displacement in a time t depends on the diffusion coefficient (D). The diffusion coefficient depends on the size of molecule, the temperature, and frictional

coefficient. In a fluid, the friction coefficient can be described as a function of viscosity and the size of the particle. For example, the value of the diffusion coefficient in the distilled water has a value of $3x10^{-3}$ mm^2/s, at 37 ^oC.

The characteristic displacement of water molecules due to diffusion is on the order of μm for a typical TE of about 100 ms of the widely used 2D singleshot diffusion-weighted EPI (2D ss-DWEPI) pulse sequence. This microscopic motion is detected by applying large bipolar gradient pulses (28). The random diffusive motion during these large gradients causes a signal loss and the magnitude of the signal loss is directly related to the diffusive motion. Typical physiological motion is several orders of magnitude greater than diffusive motion and results in large phase errors in the images if the motion occurs during the application of the diffusion encoding gradients. The effect of the motion-induced phase errors is minimized by taking the magnitude of the images before averaging, but motion can still result in signal attenuation and mis-registration between subsequent images.

Signal averaging is generally performed to improve the signal-to-noise ratio (SNR) in DW imaging. Although the between image phase error is removed by using magnitude averaging, the quality of the averaged image may be decreased by those data affected by substantial motion-induced artifact during the diffusion gradient encoding (29). And as a result the accuracy of the resultant DWI measurements is reduced.

The error caused by periodic physiological motions such as respiration, cardiac activity, and blood pulsation can be reduced by synchronizing the data acquisition with the motion cycle. However, error reduction heavily depends on the subject's cooperation in reducing voluntary, nonperiodic motions such as swallowing. Gating (30,31) has been

used to reduce motion-related inconsistencies in DTI data caused by blood and CSF pulsation in the brain (32) and in the spinal cord column (30,31). Cardiac gating mitigates the influence of motion on the accuracy of DWI measurements. Unfortunately, gating is not always reliable and increases the acquisition time. As a valid alternative to gated DWI, a postprocessing technique, selective averaging, was proposed by Wang JJ et al (33). In this technique, images to be averaged that show excessive motion-corruption are identified and discarded. The remaining images are averaged off-line. Such retrospective image elimination, however, is disadvantageous as the number of images included in averaging is reduced resulting in SNR loss. As this inspection procedure is done offline, the rejected images cannot be reacquired.

Earlier studies (34-38) proposed navigator methods to correct motion-induced phase artifacts before combining the data from multishot acquisitions. In these navigators, a single line, two orthogonal lines through the k-space center, or a 2D grid in k-space were acquired. 2D shifts can be measured accurately by a 2D navigator if the k-space center does not shift outside the FOV (37,38). Norris et al (39) introduced a new real-time correction method using a navigator and applying an adaptive gradient pulse to re-center k-space prior to acquisition.

In multishot diffusion MRI, navigator echoes are used to correct the phase inconsistency between different shots. This approach is utilized in self-navigating techniques such as SNAIL (self-navigated interleaved spiral) (40) and PROPELLER (periodically rotated overlapping parallel lines with enhanced reconstruction) (41) that use the imaging echoes as the navigator to correct the acquired data. These imaging techniques use the navigator echoes in post-processing, not in real-time. Translational

and rotational motions during the application of the strong diffusion gradients induce nonlinear phase modulation in image space (34,35). This modulation may be characterized by constant and linear phase terms for purely translational or rotational motion during the application of the diffusion gradient, respectively. The linear term in image space corresponds to a shift in the k-space. Both types of motions may also cause spatially varying attenuation of the image intensity even in singleshot DWI. Using the magnitude and position of the largest peak of echoes in k-space, DWI with excessive motion corruption can be identified and reacquired in real-time. In this chapter, a technique for real-time self-gated acquisition (RTSG) of 2D singleshot diffusion-weighted EPI (2D ss-RTSG-DWEPI) is described. The technique monitors the data consistency in real-time by using the real-time feedback capability of the MRI system to identify, reject, and reacquire any data with substantial corruption due to the motion.

3.2 Theory

3.2.1 Principles of Diffusion MRI

Diffusion weighted images are generated by applying a pair of large gradient pulses (28) as shown in Figure 3.1, where G and δ are the magnitude and the duration of the diffusion-weighting gradient pulses, respectively. The signal decay because of the diffusion weighting is summarized by the following formula:

$$S = \iint_{-\infty}^{+\infty} S_0 e^{i\gamma \vec{G}\cdot(\vec{r}_2-\vec{r}_1)\delta} P(\vec{r}_2|\vec{r}_1,\Delta) d\vec{r}_1 d\vec{r}_2 \qquad (3.2)$$

Here S_0 is the signal in the absence of diffusion gradients, $i\gamma\vec{G}\cdot(\vec{r}_2-\vec{r}_1)\delta$ is the phase term associated with displacement of $(\vec{r}_2-\vec{r}_1)$, and $P(\vec{r}_2|\vec{r}_1,\Delta)$ is the probability of a water molecules initially at $\vec{r}_1$ travelling to $\vec{r}_2$ during the time interval Δ. It is defined as:

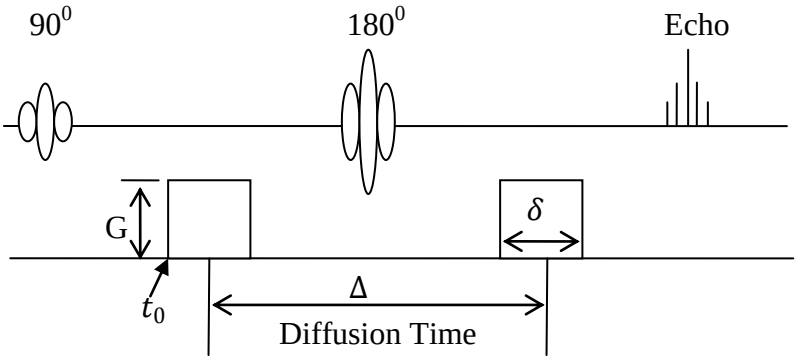

Figure 3.1. Diffusion weighted spin echo pulse sequence.

$$P(\vec{r}_2|\vec{r}_1,\Delta) = \frac{1}{(4\pi D\Delta)^{-3/2}} e^{-\frac{(\vec{r}_2-\vec{r}_1)\cdot(\vec{r}_2-\vec{r}_1)}{4D\Delta}} \tag{3.3}$$

If we integrate Eq. (3.2) within one pixel, the following equation is obtained.

$$S = S_0 e^{-\left(\sum_{i=x,y,z}\sum_{j=x,y,z} b_{i,j} D_{i,j}\right)}, \tag{3.4}$$

where $b_{i,j} = \gamma^2 G_i G_j \left[\delta^2\left(\Delta - \frac{\delta}{3}\right)\right]$. $D_{i,j}$ is a diffusion tensor (42) corresponding to the two applied diffusion gradient directions. The diffusion properties are relatively independent of orientation or isotropic in the gray-matter of the human brain. Conversely, in fibrous tissues such as brain white matter, the diffusivity varies with orientation. We can summarize this information to suggest that: assume the diffusion coefficient in pure water is D_0,

Isotropic unrestricted diffusion (Free water): $\begin{bmatrix} D_0 & 0 & 0 \\ 0 & D_0 & 0 \\ 0 & 0 & D_0 \end{bmatrix}$

Isotropic restricted diffusion (in the presence of barrier $< D_0$): $\begin{bmatrix} D & 0 & 0 \\ 0 & D & 0 \\ 0 & 0 & D \end{bmatrix}$

Anisotropic restricted diffusion (coherent axonal bundle): $\begin{bmatrix} D_{xx} & D_{xy} & D_{xz} \\ D_{yx} & D_{yy} & D_{yz} \\ D_{zx} & D_{zy} & D_{zz} \end{bmatrix}$

Considering the symmetric properties of diffusive motion, $D_{xy} = D_{yx}$, $D_{xz} = D_{zx}$ and $D_{zy} = D_{yz}$, i.e., the diffusion tensor is a symmetric second-rank tensor. According to Figure 3.1, the b factor can be computed as $\gamma^2 G^2 \left[\delta^2 \left(\Delta - \frac{\delta}{3}\right)\right]$. For isotropic tissue, the apparent diffusion coefficient (ADC) will be obtained from Eq. (3.4) .

$$ADC = -\frac{1}{b} ln\left(\frac{S}{S_0}\right) \tag{3.5}$$

However, in anisotropic tissues, a series of diffusion-weighted images must be obtained with the diffusion encoding gradient applied along various directions to extract principal diffusion coefficient values in the corresponding direction. At least six individual diffusion encoding directions are used to solve the linear equations. As a result, diffusion coefficient matrix can be thought as a symmetric second rank tensor. It is well known that a tensor can be reduced to principal axes referred to an eigenvalue and eigenvector decomposition if the below equation has a nontrivial solution.

$$D \begin{pmatrix} a_x \\ a_y \\ a_z \end{pmatrix} = \lambda \begin{pmatrix} a_x \\ a_y \\ a_z \end{pmatrix} \tag{3.6}$$

Here $D = \begin{bmatrix} D_{xx} & D_{xy} & D_{xz} \\ D_{xy} & D_{yy} & D_{yz} \\ D_{xz} & D_{yz} & D_{zz} \end{bmatrix}$, λ is the eigenvalue with eigenvector $\vec{A}(= a_x \vec{\imath} + a_y \vec{\jmath} + a_z \vec{k})$. By solving the characteristic equation of Eq. (3.6), we derive

$$\begin{aligned} &\lambda^3 - \lambda^2 \left(D_{xx} + D_{yy} + D_{zz}\right) \\ &\quad + \lambda \left(\begin{vmatrix} D_{yy} & D_{zy} \\ D_{yz} & D_{zz} \end{vmatrix} + \begin{vmatrix} D_{xx} & D_{yx} \\ D_{xy} & D_{yy} \end{vmatrix} \right. \\ &\quad \left. + \begin{vmatrix} D_{xx} & D_{zx} \\ D_{xz} & D_{zz} \end{vmatrix} \right) - \begin{vmatrix} D_{xx} & D_{xy} & D_{xz} \\ D_{xy} & D_{yy} & D_{yz} \\ D_{xz} & D_{yz} & D_{zz} \end{vmatrix} = 0 \end{aligned} \tag{3.7}$$

In Eq. (3.7), λ is independent of coordinate system choice and so are their coefficients. The solution of Eq. (3.7) is λ_1, λ_2 and λ_3, respectively. Thus three scalar invariants (36) are defined as B_1, B_2 and B_3 in Eq (3.8). Another index that describes the diffusion anisotropy is called as the relative anisotropy (RA) as shown in Eq. (3.9). I is the identity matrix. RA represents the ratio between the anisotropic and isotropic parts in diffusion tensor, respectively.

$$B_1 = Trace(D)$$

$$B_2 = \frac{1}{2}\left(Trace(D)^2 - Trace(D^2)\right) \tag{3.8}$$

$$B_3 = Determinant(D)$$

$$RA = \frac{\sqrt{\left(\lambda_1 - \bar{\lambda}\right)^2 + \left(\lambda_2 - \bar{\lambda}\right)^2 + \left(\lambda_3 - \bar{\lambda}\right)^2}}{\sqrt{3}\bar{\lambda}} \tag{3.9}$$

where $\bar{\lambda} = \frac{1}{3}(\lambda_1 + \lambda_2 + \lambda_3)$.

3.2.2 Motion Artifact

Diffusion gradients are usually much larger and longer than imaging gradients. Motion induced artifacts are much larger with diffusion gradients than with imaging gradients alone. In this section, two kinds of rigid body motion are described. The first one is the translation motion, and the other is rotation motion. Because a singleshot imaging technique (EPI) is generally used in DWI acquisition, motion during the sampling period can be thought as "frozen." The greatest artifact results only from the subject's motion during application of the diffusion gradient.

We assume that translation motion occurs only along the readout direction and diffusion gradient is also implemented in the same orientation. The object's trajectory is

expanded as in following equation

$$x(t) = x(t_0) + v_x(t_0)t + \frac{a_x(t_0)t^2}{2} + \cdots, \tag{3.10}$$

where $x(t_0), v_x(t_0)\ and\ a_x(t_0)$ are the position, velocity and acceleration at the initial time t_0, respectively. In Figure 3.1, the motion-induced phase can be written as

$$\begin{aligned} \varphi_d &= \gamma x(t_0) \int_{t_0}^{t_0+\delta+\Delta} G dt' \\ &\quad + \gamma v(t_0) \int_{t_0}^{t_0+\delta+\Delta} G t' dt' \\ &\quad + \frac{\gamma a_x(t_0)}{2} \int_{t_0}^{t_0+\delta+\Delta} G t'^2 dt' + \ldots \\ &= \varphi_0 + \varphi_c + \varphi_a + \cdots \end{aligned} \tag{3.11}$$

The first term φ_0 on the right side of the equation indicates the phase shift that occurs in the absence of motion. It leads to signal decay due to microscopic diffusive motion. The second term φ_c results from the motion of the object with constant speed.

$$\begin{aligned} \varphi_c &= \gamma v(t_0) \int_{t_0}^{t_0+\delta+\Delta} G t' dt' \\ &= \gamma v(t_0) \left[\int_{t_0}^{t_0+\delta} G t' dt' - \int_{t_0+\Delta}^{t_0+\delta+\Delta} G t' dt' \right] \\ &= \gamma v(t_0) \left[\frac{G}{2}(\delta^2 + 2t_0\delta) - \frac{G}{2}(\Delta^2 + 2\Delta t_0 + 2\Delta\delta) \right] \end{aligned} \tag{3.12}$$

Eq. (3.12) is only a constant phase. In the ideal case, there is no effect on the image if there is no diffusion. In reality, motion may cause signal loss on the image. The third and

higher order phases come from the accelerating motion. The phase resulting from translation motion induces signal decay.

For rotational motion, in order to simplify the calculation, we consider constant angular speed with respect to the center of the object. Figure 3.2(a) demonstrates that the objects rotate at a constant angular velocity. (b) shows that the magnetization phase profile in nine pixels inside the object in the absence of motion. (c) and (d) are the velocity profile in both phase encoding and readout direction due to object rotation in one pixel. (e) indicates the phase profile directly after diffusion gradient in the presence of motion. (c) and (d) explains why the signal in one pixel decays in the presence of rotation motion. For different pixels in Figure 3.2(e), net phase varies as the readout and phase encoding spatial position. Therefore, the additional phase induced by rotation motion can be written as

$$\varphi = \Delta k_{readout}\, x + \Delta k_{phase}\, y, \tag{3.13}$$

where $\Delta k_{readout}$ and Δk_{phase} describes the relations between extra phase and spatial position in both directions. Signal in k-space is expressed as

$$\begin{aligned} S &= \iint_{-\infty}^{+\infty} \rho(x,y) e^{-i\left(k_{readout}\ x + k_{phase}\, y\right)} e^{i\varphi} \\ &= \iint_{-\infty}^{+\infty} \rho(x,y) e^{-i\left[\left(k_{readout}\ - \Delta k_{readout}\ \right)x + \left(k_{phase} - \Delta k_{phase}\right)y\right]} \end{aligned} \tag{3.14}$$

Eq. (3.14) exhibits that the k-space center shift depends on the magnitude of rotation motion. Severe rotational motion may completely corrupt the diffusion weighted echo planar image.

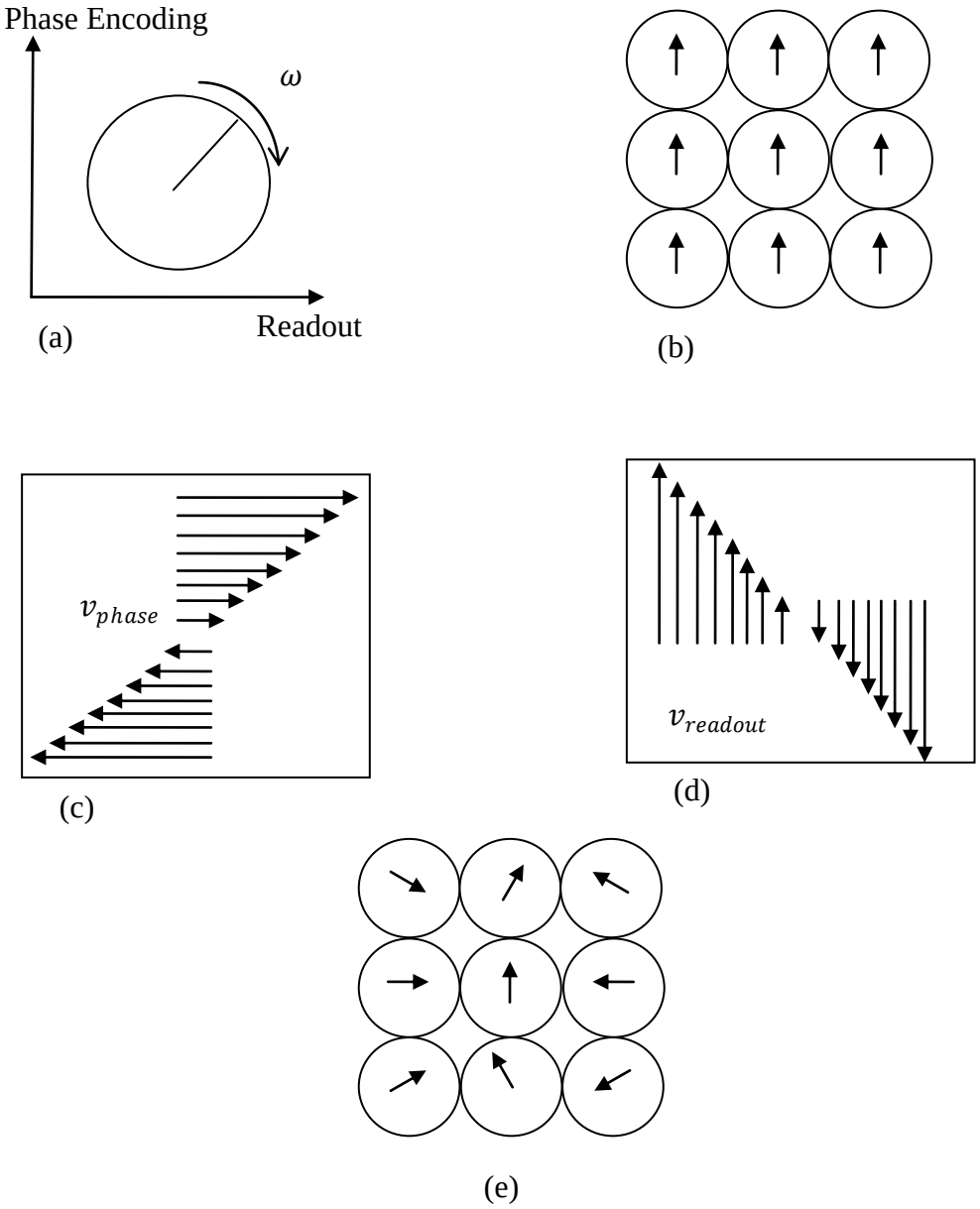

Figure 3.2. Motion-induced phase evolution and profile. (a) Object rotates at an angular speed ω. (b) Magnetization phase in nine pixels in the absence of rotation motion. (c) and (d) represent the velocity profile induced by rotation motion along the readout and phase encoding direction in one pixel, respectively. (e) Phase distribution right after diffusion gradients in the presence of rotation motion.

3.3 Methods

3.3.1 2D ss-RTSG-DWEPI

RTSG data acquisition was implemented in 2D ss-EPI, using the IDEA pulse sequence development environment (Siemens Medical Solutions, Erlangen, Germany). Real-time calculation of the navigated data was incorporated into an image reconstruction program using the Image Calculation Environment (ICE). The diagram of the developed pulse sequence is shown in Figure 3.3.

The pulse sequence is capable of Interleaved Multi-slice Inner Volume Imaging (IMIVI) of a reduced field-of-view (FOV) in the phase-encoding direction (43,44) . Two adiabatic RF pulses were used for IMIVI preparation. The first inversion pulse is non-selective whereas the second one is accompanied by a slice-selection gradient in the phase-encoding direction to define the reduced FOV in the phase-encoding direction. The application of IMIV preparation increased the TE by about 14 ms, which included two 5.12 ms RF pulses and a pair of crusher gradients sandwiched around each RF pulse. The crusher gradients are used to destroy the stimulated echoes caused by imperfection of the 180^{o} pulses.

Diffusion weighting was accomplished by adding a pair of Stejskal-Tanner diffusion-weighting gradient pulses (28) on both sides of the third 180^{o} RF. A real-time feedback flag was added to all EPI readouts. Using this flag, the acquired data served as a 2D navigator as well as the imaging data. Upon the transfer of the raw data to the image reconstruction computer, the echo data with realtime feedback flag were immediately fed into the real-time calculation algorithm, which identified the largest peak in k-space and calculated its coordinate $\boldsymbol{k}_{\mathrm{pk}}$ and magnitude $m(\boldsymbol{k}_{\mathrm{pk}})$, and sent these values to the scanning

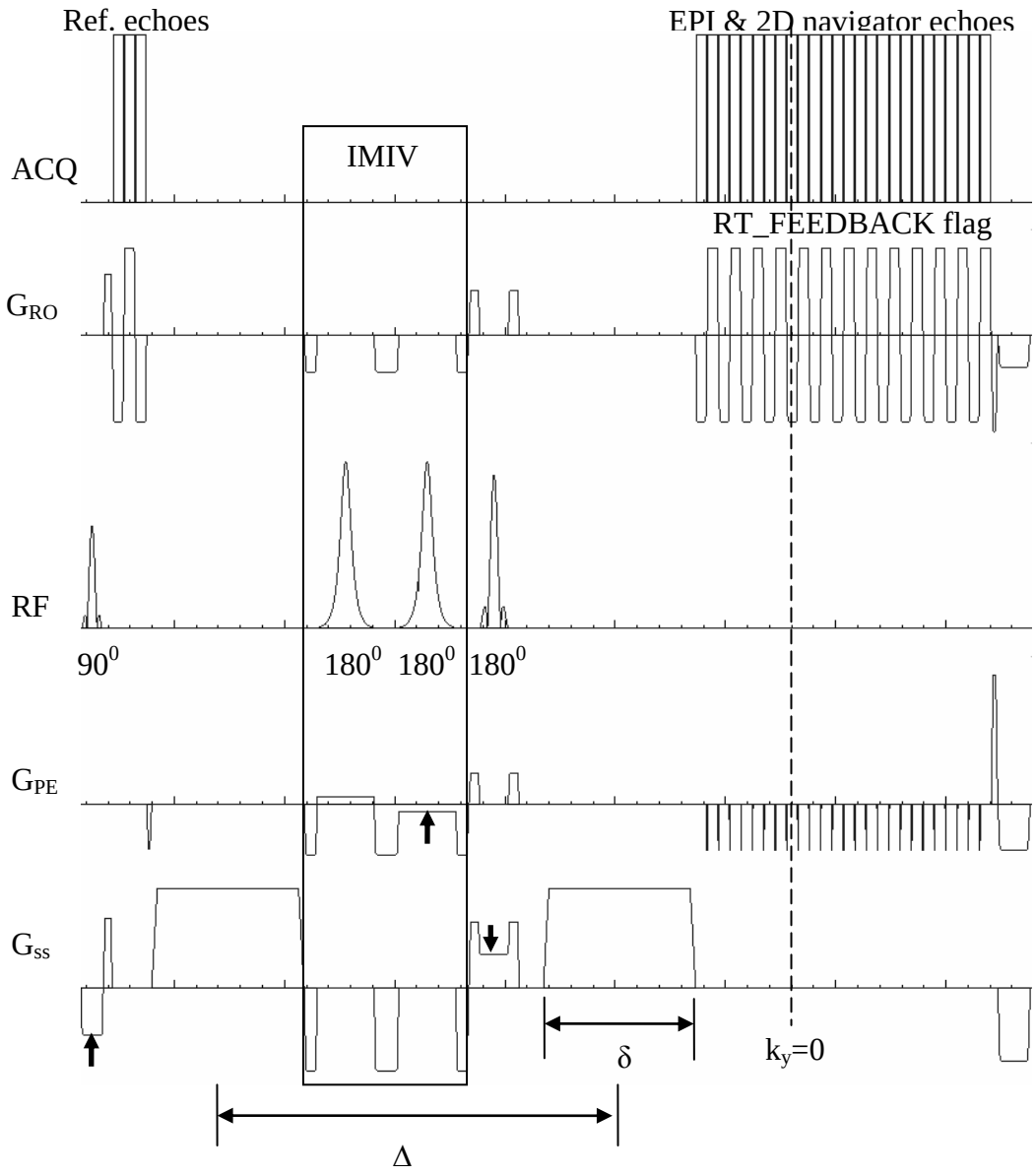

Figure 3.3. Diagram of 2D ss-RTSG-DWEPI pulse sequence with IMIV preparation. Vertical arrows indicate the slice-selection gradients. Two 180^o RF pulses enclosed within the dotted box are used to reduce the FOV in the phase-encoding direction. An operator controlled flag was set for EP readouts to activate real-time calculation. The dashed vertical line indicates the position of the spin-echo which coincides with the k-space center.

computer for the RTSG test. The location $\boldsymbol{k}_{pk}$ of the largest peak of the 2D data should correspond to the k-space center if no motion occurs during diffusion gradient application and if the timing and amplitudes of the imaging gradients are exact. Images are reconstructed only for the shots which pass the RTSG test. Our RTSG test criterion is that if magnitude changes and the shift of the k-space center are larger than 30% (38) and 2 pixel compared with those of reference data, respectively, the current measurement is rejected and reacquired.

The block diagram in Figure 3.4 describes the RTSG procedure of 2D ss-RTSG-DWEPI. The dashed and the dotted boxes indicate the processes in the data acquisition and the image reconstruction computers. The real-time calculation is processed by the ICE program within the image reconstruction computer. Indices n_{avg}, n_{reacq}, and d_j denote the counters for averages, reacquisitions, and diffusion encodings, respectively. The position $\boldsymbol{k}_{pk,1}$ and the magnitude $m(\boldsymbol{k}_{pk,1})$ of the largest echo in the 2D navigator of the first average shot ($n_{avg} = 1$) are stored into a temporary memory as the reference values and are used for comparison with the subsequent data. For each diffusion encoding direction d_j and average count n_{avg}, a maximum number of reacquisitions is set to avoid an over-extended scan duration. If the data successfully pass the RTSG test, the reacquisition counter n_{reacq} is reset to zero, which also directs the image reconstruction computer to calculate the image and send it to the image database. Then, the scan proceeds to the next diffusion encoding. In case the maximum reacquisition count is reached without passing the RTSG test, the data with the least change in the magnitude and the location of the largest k-space echo-peak are selected.

A cooperative human subject tends to remain still in the earlier stage during the

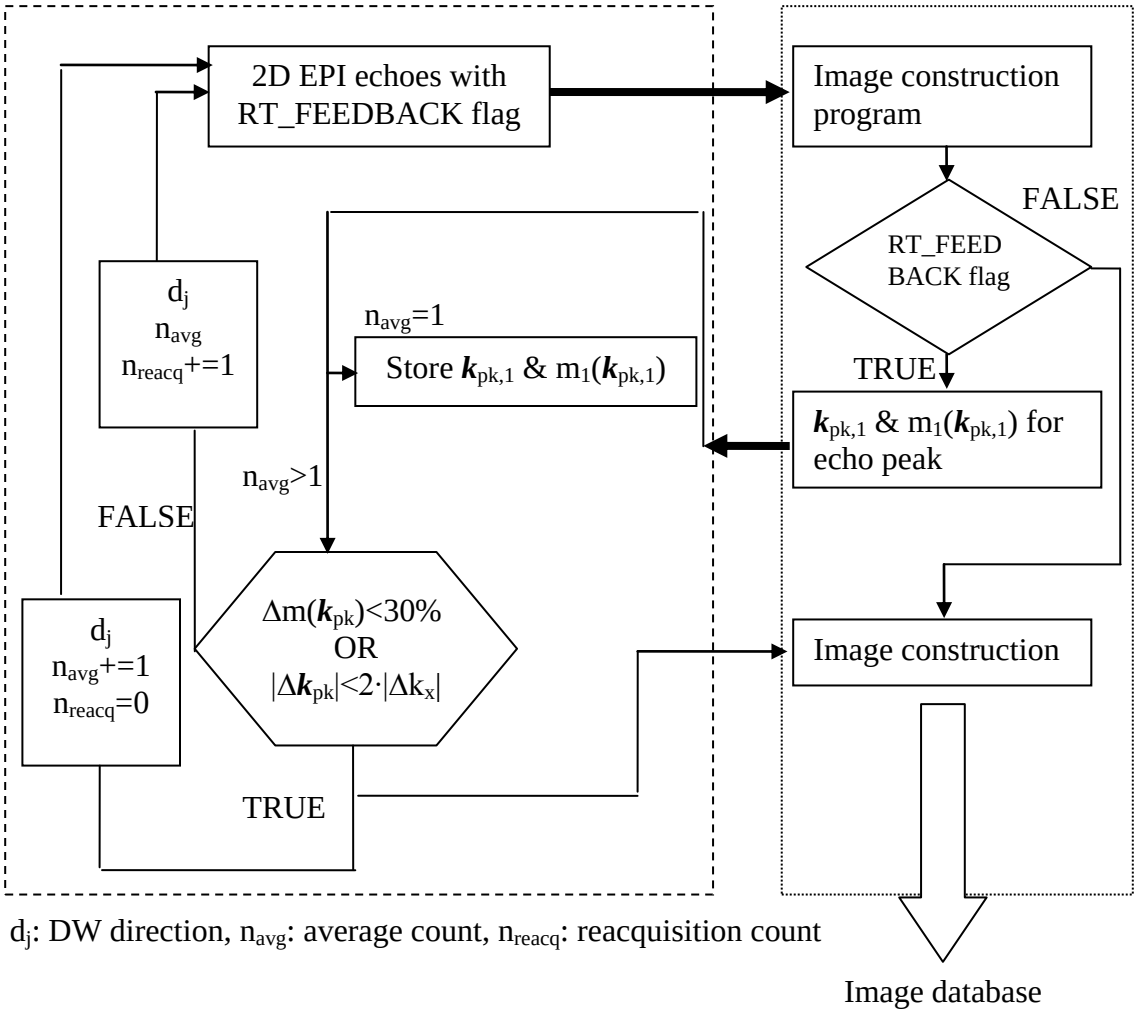

Figure 3.4. Flowchart of RTSG acquisition and real-time calculation for diffusion encoding d_j. Thick arrows indicate the data transfer between the data acquisition and the reconstruction computers. All MR data, including the 2D navigator, are sent to the reconstruction computer to locate the largest signal and to calculate its magnitude and position in k-space. These values are transferred to the scan computer to determine if the data is acceptable by comparing with the reference parameters.

measurement. Thus, the reference data were acquired at early averaging shot of DT imaging acquisition. The magnitude and position of the largest echo peak of the reference data in the time domain are stored and compared with those of the subsequent averaging shots to determine if the data acquired by other shots are acceptable. If the reference data are motion-corrupted, current measurement must be stopped and restarted.

Diffusion tensor data were evaluated by comparing, (1) intensity and uniformity of the signals on the reacquired and the motion-corrupted images and (2) internal angles of the principal eigenvectors of the data sets that include motion-corrupted or reacquired data with respect to the principal eigenvector of motion-free data.

3.3.2 MRI Experiment

MRI studies were performed on a Siemens Trio 3 Tesla MRI system (Siemens Medical Solutions, Erlangen, Germany) with Avanto gradients (45 mT/m strength and 200 T/m/s slew rate). A set of 2D ss-RTSG-DWEPI images of a phantom was acquired with diffusion weighting b=0 and 500 s/mm^2 in four noncollinear directions, (1,0,0), (0,0,1), (1,0,1), and (-1,0,1) in physical gradient coordinates (G_x, G_y, G_z) that represent (vertical, horizontal, magnet bore) or (A/P, R/L, S/I) anatomic directions. The phantom was intermittently moved during the scan to simulate a subject's random physiological motion. The maximum number of reacquisition was set to 2 and the threshold values for RTSG testing were 30 % and 2Δk for deviations of the peak magnitude and the peak position from the reference values. The minimum number of slices for failure of the RTSG test was set to 2 for interleaved multislice 2D imaging. Thus, the slice group was reacquired if two or more slices out of the slice group imaged during the current TR failed the RTSG test.

2D ss-RTSG-DWEPI was applied to acquire DWI from healthy human volunteers, using the imaging parameters: image matrix 128x96, FOV of 256x192 mm, TR/TE 5000/66 ms. Total number of imaging slices was 20. A 12 channel receive-only head-matrix coil (Siemens Medical Solutions, Erlangen, Germany) was used. To demonstrate the feasibility of the RTSG data acquisition for human imaging, the technique was tested for the following cases: a) the volunteer stays still during entire data acquisition; b) the volunteer stays still during earlier phase of acquisition and moves during the later phase of acquisition; c) the volunteer commits intentional head motion during the whole data acquisition. Diffusion weighting was performed with b = 0 and 750 s/mm^2 in 7 non-collinear directions along three orthogonal axes and four tetrahedral vertices: (1,0,0), (0,1,0), (0,0,1), (1,1,1), (-1,-1,1), (1,-1,-1), and (-1,1,-1). RTSG was accomplished with threshold values of 30 % (38) and 2Δk for the magnitude and the position changes of the largest echo-peak, and with the maximum number of reacquisition of 2. If the number of failed slices exceeded 4, all slices were reacquired for a specific average.

To achieve a robust real-time response from the image reconstruction computer, which is required for RTSG, only data from one coil element was used in the RTSG test. The selection of the coil element for RTSG was implemented in the pulse sequence interface. For brain imaging, the most anterior coil element of the head coil was chosen for RTSG evaluation, because it is the closest to the anterior part of the head which has the maximum movement. During data acquisition, subjects were instructed to move the head in the anterior-posterior direction. Due to the narrow space in the head coil, the subjects' motion was mostly rotational motion. The imaging protocol was approved by

the University of Utah Institutional Review Board and informed consent was obtained from the volunteers.

DW images were postprocessed using DTI analysis software written in Matlab (version 7.1, The Mathworks Inc., Natick, MA) to (1) extract the 6 independent diffusion tensor matrix elements using singular-value decomposition, (2) diagonalize the diffusion tensor matrix, and (3) visualize the results, using either fractional anisotropy or a three color (RGB) representation of the principal eigenvector. The fractional anisotropy (FA) was obtained from the three eigenvalues ($\lambda_1, \lambda_2, \lambda_3$) as a measure of anisotropy.

$$FA = \sqrt{\frac{3}{2}} \cdot \sqrt{\frac{(\lambda_1 - \bar{\lambda})^2 + (\lambda_2 - \bar{\lambda})^2 + (\lambda_3 - \bar{\lambda})^2}{\lambda_1^{\,2} + \lambda_2^{\,2} + \lambda_3^{\,2}}}\,.$$

Here, the average diffusivity $\bar{\lambda}$ was defined as $\bar{\lambda} = (\lambda_1 + \lambda_2 + \lambda_3)/3$.

3.4 Results

Typical results of the phantom studies are presented in Figure 3.5. The magnitude and phase images at a specific slice from the different measurements are shown in Figure 3.5a and Figure 3.5c. The numerical indices enclosed within the circles indicate the different diffusion encoding directions (e.g., "0" corresponds to b=0 s/mm^2 measurement). The indices inside the rectangular boxes represent the different slices.

The data that failed the RTSG test and were rejected are indicated by the dashed circles as the diffusion direction 2, and the accepted data are represented by the solid circles. From Fourier Transform theory, one pixel shift in k space corresponds to a 2π phase modulation across the FOV in image space. Thus, the number of 2π phase modulations across the FOV that are visible in the phase images represents the number of Δk shifts in k-space. The measurements for which either the magnitude of the peak signal

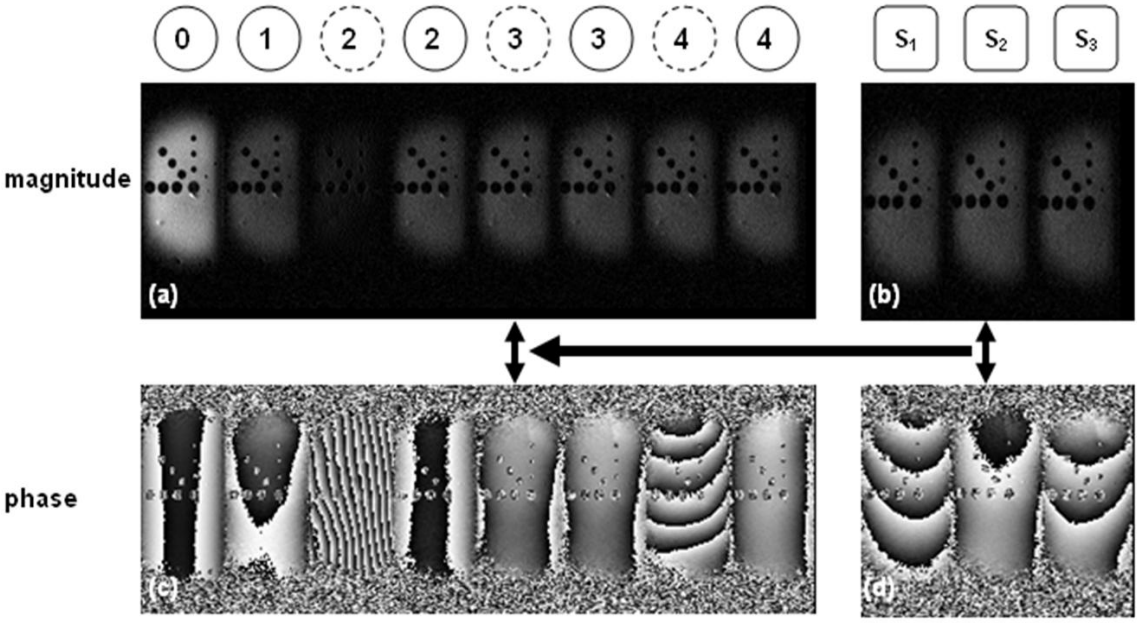

Figure 3.5. Top row: magnitude images; bottom row: phase images. Phase-encoding gradient is applied along the left-right direction in plane. The solid and dashed circles on the top represent the accepted and motion-corrupted measurements, respectively. The numbers (S_1, S_2 and S_3) enclosed within the rectangular boxes represent images of different slices when diffusion gradient is added on the (1, 0, 1) direction in physical gradient coordinate (G_x, G_y, G_z) during a given repetition time (TR).

was changed more than 30 % or the position of the peak was shifted more than 2Δk from the reference values were reacquired.

For direction 3, although the first measurement for the current slice passed the RTSG test, RTSG reported the failure for this measurement, because two other slices (S_1 and S_3) from the slice group scanned during the same TR failed the test as follows from Figure 3.5b and Figure 3.5d. The peak signals for slices 1 and 3 were shifted by 3Δk and 2Δk respectively, relative to the reference position. Therefore, the acquisition for direction 3 was repeated. The change in magnitude and position of the largest echo shown in Figure 3.5 in k-space relative to the reference values are plotted in Figure 3.6a

and Figure 3.6b, respectively. The horizontal axis represents the diffusion encodings (e.g., 0 for b = 0 s/mm^2).

The images in Figure 3.7 are the magnitude and phase images corresponding to the reference, the motion-corrupted, and the reacquired data from DW imaging of a human volunteer. The volunteer intentionally nodded his head to initiate the rotational motion during acquisition of the corrupted shot. Comparison of the corrupted and reacquired images clearly indicates a significant drop of magnitude in Figure 3.7b and recovery in Figure 3.7c, respectively. The RTSG test reported a 52 % change of magnitude and a 7 Δk shift of the signal peak for these specific data in Figure 3.7 (b, e) compared to the reference data in Figure 3.7 (a, d).

The images in Figure 3.8 are the magnitude and phase images of the reference, motion-corrupted, and reacquired data from a volunteer, who stayed still during the entire data acquisition except for occasional swallowing. The RTSG test reported a magnitude change of less than 0.5 % which passed the magnitude test. The *2*Δk shift of the peak

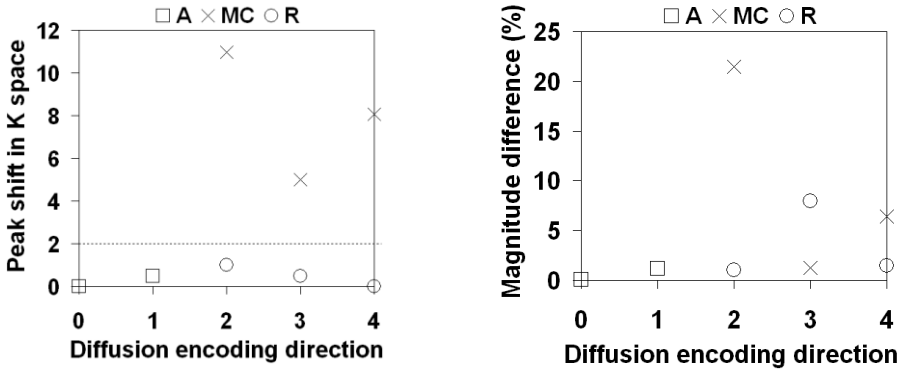

Figure 3.6. Plot of changes in the peak signal magnitude and its position for phantom shown in Figure 3.5 in k-space for various diffusion encodings. The horizontal axis labels represent b=0, (1,0,0), (0,1,0), (0,0,1), and (1,1,1). Where A, MC and R represent accepted data, motion-corrupted data and reacquired data, respectively.

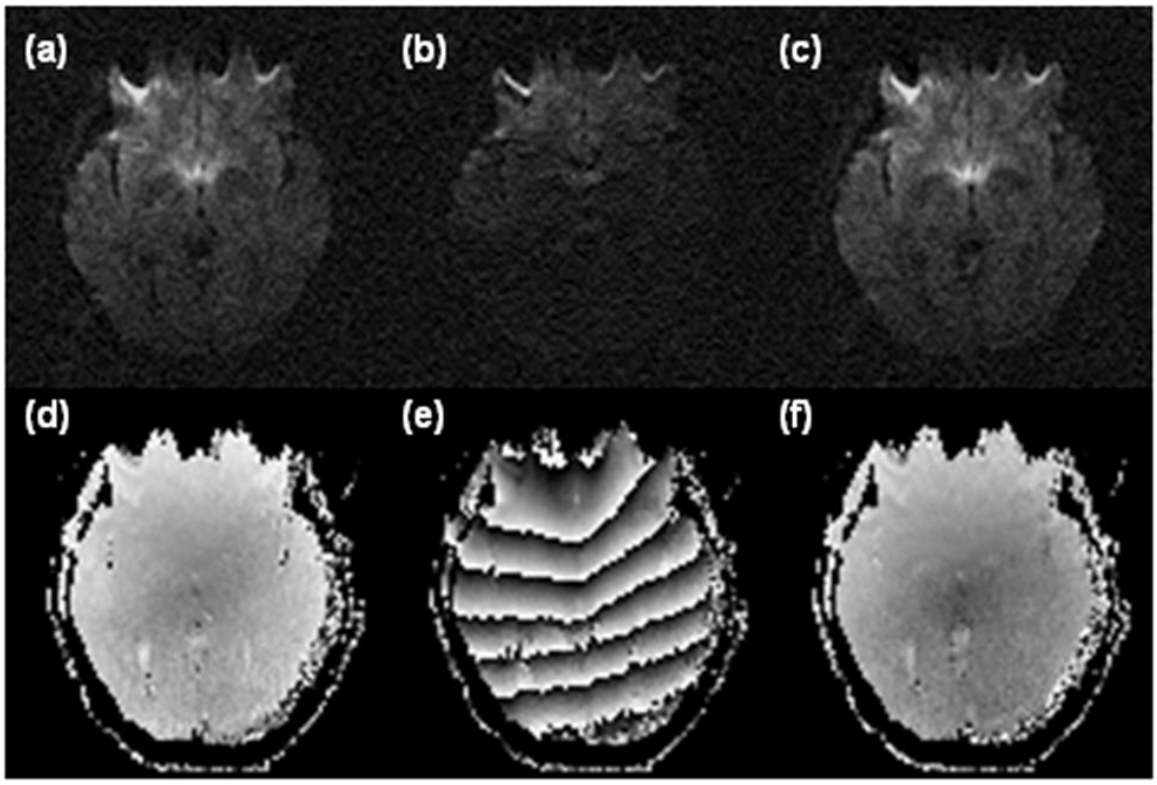

Figure 3.7. Magnitude (a-c) and corresponding phase images (d-f) form DTI of healthy human brain. Pairs of images (a, d), (b, e), and (c, f) indicate the magnitude and phase images from the reference, motion corrupted, and reacquired data, respectively.

echo, however, failed the peak position test and therefore the data were reacquired in real-time. Images in Figure 3.7 and Figure 3.8 clearly demonstrate the different degrees of magnitude change and phase-shifts in the resultant DW images from the large and small movements.

Three sets of DTI data of two average and eight directions, i.e., total 16 measurements, were constructed from total tensor data; (a) motion-free data, (b) motion-corrupted data: total 16 measurements with two motion-corrupted measurements from the 9^{th} to the 12^{th} shot, and (c) reacquired data: two motion-corrupted measurement data replaced by the reacquired data. To demonstrate the effect of motion-corrupted and reacquired data on the final DTI measurements, only two signal averages were used for

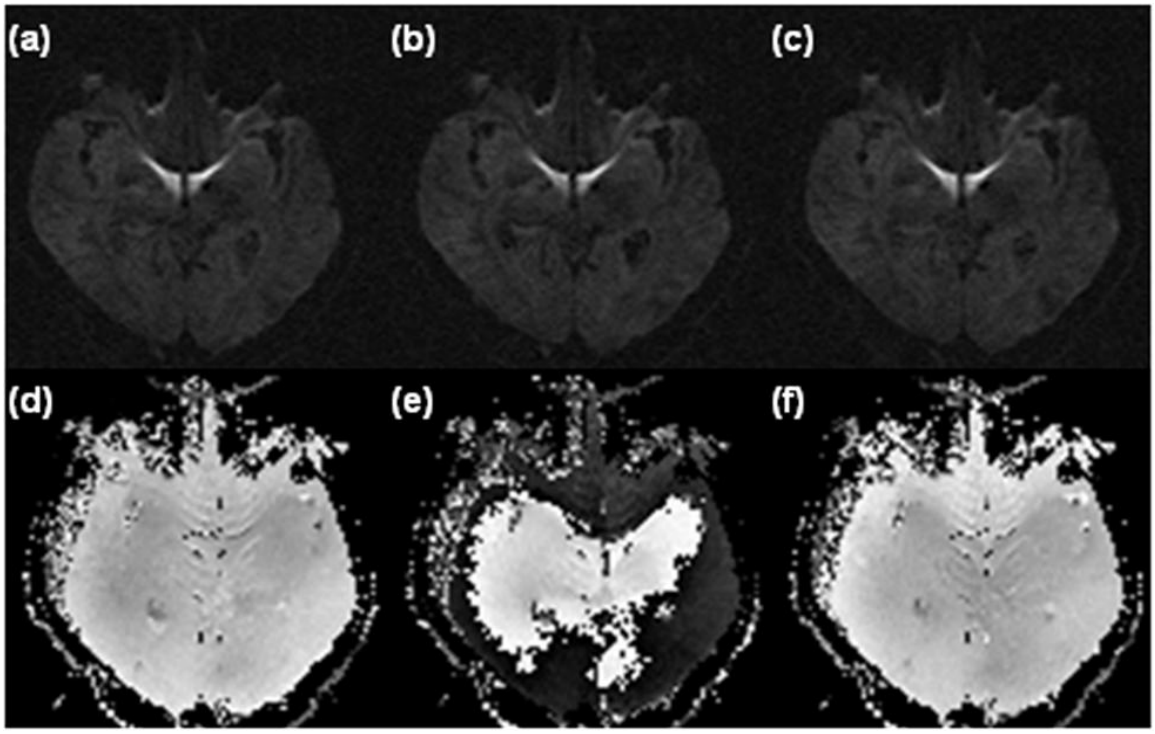

Figure 3.8. Real-time Self-Gated DW imaging for a typical cooperative subject. The subject held still during the DW imaging, other than swallowing and breathing. The RTSG test rejected the data for images (b, e) because of a 2 Δk shift of the peak echo for these specific data.

each diffusion encoding direction. These three data sets were used to construct the DTI parameter maps. For the measurements that failed RTSG testing for all reacquisitions, the shot with the least variation of the magnitude and the peak position of the largest echo-peak was selected for the reacquired data set.

Because the true values of the DTI parameters (FA and the direction of the principal eigenvector) are not available, DTI parameters from the motion-free data set may be considered to be close to the true values, in comparison to those from the motion-corrupted or reacquired data sets. Figure 3.9a is the averaged motion-free diffusion-weighted image of a slice that failed the most RTSG testing for the shots 9 ~ 12 during which the subject moved. The difference images were constructed between the motion-

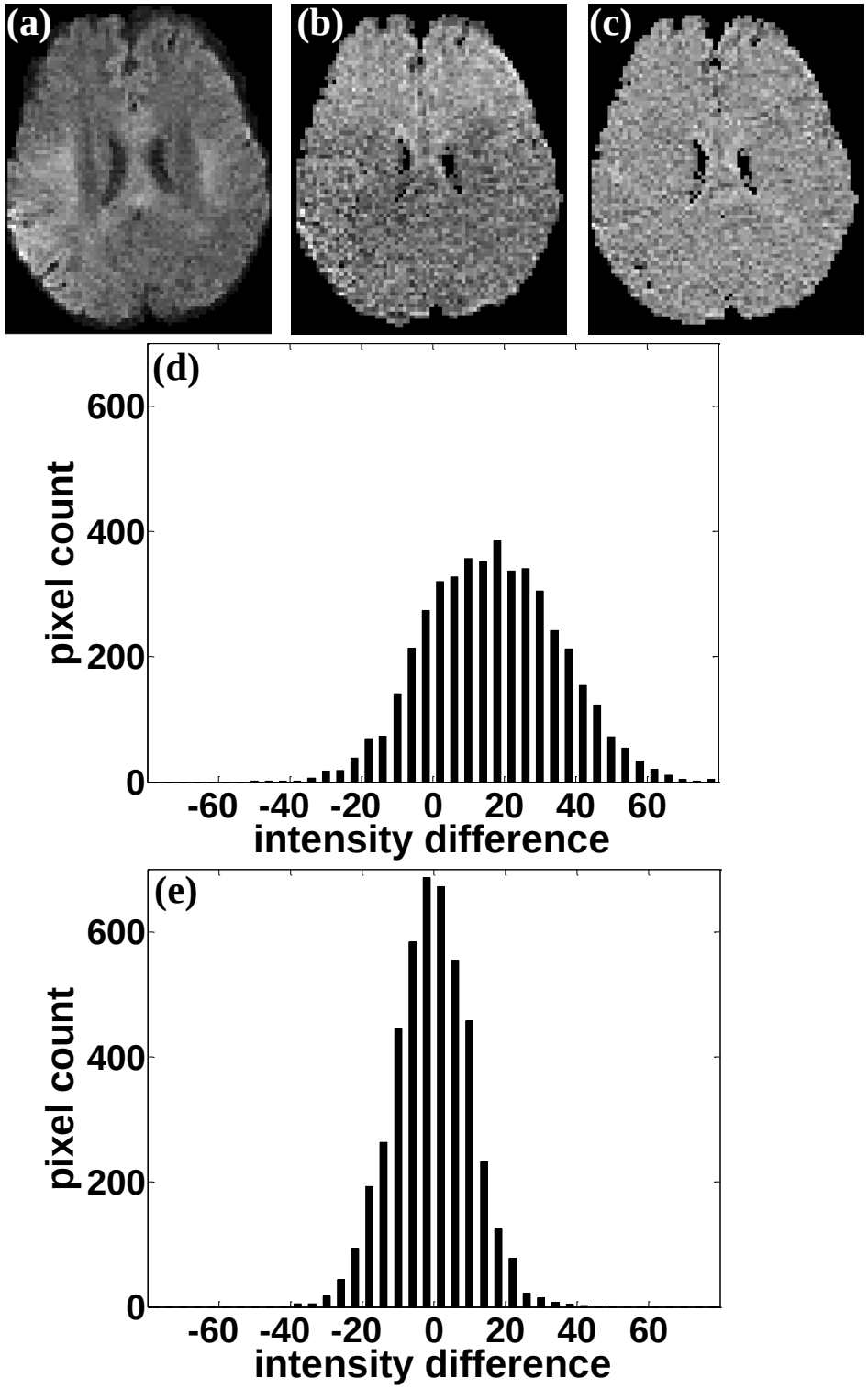

Figure 3.9. Comparison of diffusion weighted images. (a) Magnitude averaged DW image of motion-free data, and the difference images (b) between motion-free image and motion-corrupted image, and (c) between motion-free and motion-corrected using the reacquired images. The plots of (d, e) are the histograms of difference images (b) and (c), respectively.

free and motion-corrupted (Figure 3.9b) and reacquired averages (Figure 3.9c). The signal intensities of these difference images are plotted in the histograms in Figure 3.9(d, e). It is clearly indicated that the consistency of the reacquired data set was improved by using the RTSG reacquired average.

Images and histogram plots in Figure 3.10 illustrate consistency between the principal eigenvectors calculated using the motion-free, motion-corrupted, and reacquired data sets. The principal eigenvectors were used to construct the maps of the directional correlation defined as $\left[1 - |cos\theta\left(\overrightarrow{e_1} \cdot \overrightarrow{e_1}'\right)|\right]$. Where $\theta\left(\overrightarrow{e_1} \cdot \overrightarrow{e_1}'\right)$ is the internal angle between the principal eigenvectors, $\overrightarrow{e_1}$ is the principal eigenvector of the motion free data, and $\overrightarrow{e_1}'$ is the principal eigenvector of the motion-corrupted or the reacquired data sets. The histogram shown in Figure 3.10b and Figure 3.10d were evaluated from the whole brain. The images and the histograms in Figure 3.10 indicate that the principal eigenvectors of the RTSG reacquired data set are less deviated from the motion-free data set than those of the motion-corrupted acquisition data set.

3.5 Discussion

Signal averaging is generally performed to improve SNR in DW imaging. Any discrepancy in images between different averages reduces the accuracy of diffusion MRI measurements. Our motion artifact reduction scheme with real-time self-gated data acquisition for diffusion MRI can be used to resolve this problem. In our technique, the acquired data are used for both navigation and image reconstruction and the acceptance criteria are based on the signal intensity and position in k-space. In the current study, 30 % for the peak signal magnitude variation and 2Δk for the peak signal position shift in k-space were used as the acceptance criteria. Decreasing the acceptance criteria values will

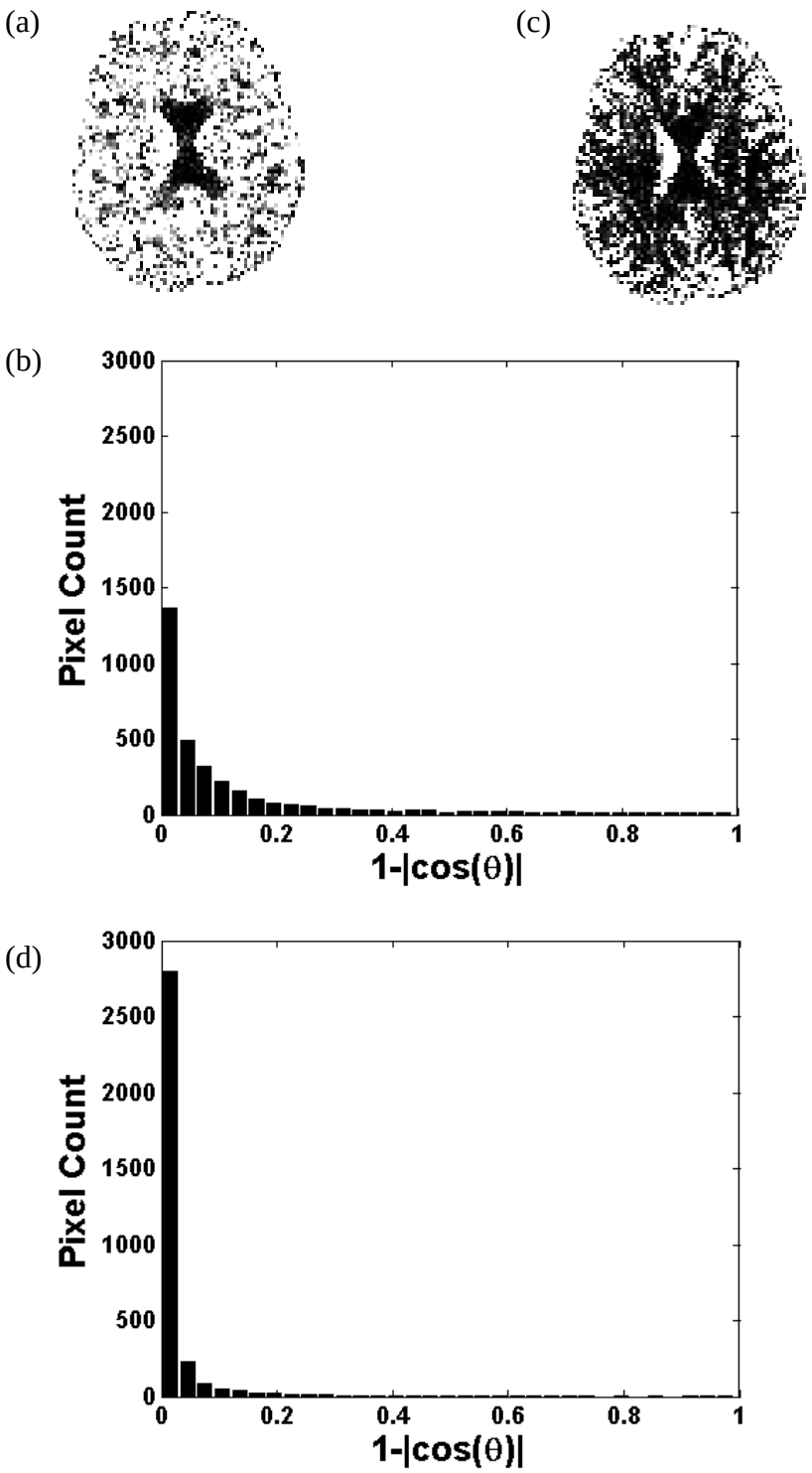

Figure 3.10. Directional correlation map and its histogram. (a) and (c) the directional correlation (1-|cosθ|) images for the motion-corrupted (a) and the reacquired images (c), respectively. (b, d) the histograms of the directional correlation values in the brain.

increase the imaging time, which may in turn induce a higher chance of permanent position change between measurements. For our testing, the limit on the number of reacquisitions of a specific measurement was set to 2 for all studies to avoid unacceptably long imaging times. This limit may be increased for cooperative subjects. However, the increased number of reacquisitions may yield too many failures of the RTSG test and significantly extend the imaging time for uncooperative patients.

During the preliminary studies, there were times when the maximum number of reacquisitions was exceeded without passing the RTSG test and the scan proceeded to the next measurement. In such cases, the acquisition with the least deviation in the magnitude and position of the largest signal peak from the reference parameters was selected for averaging.

There is a time interval required for the RTSG process, which includes the time for data communication between the data acquisition and reconstruction computers and the time for RTSG calculation. This time interval should be kept minimal because it limits the number of slices that can be interleaved during the prescribed TR. Our implementation of the RTSG procedure requires less than 1 ms because the calculation in the real-time image reconstruction program was very simple.

As implemented, our RTSG algorithm would not be able to detect subject motion that results in a position change between shots because such motion would not yield any significant changes in the magnitude and/or position of the signal peak. However, the RTSG algorithm may be readily modified to detect such a position shift. After such a position shift is detected, postprocessing may be used to co-register the later averages with respect to the early ones before magnitude averaging.

RTSG technique may be implemented into a multishot DWEPI sequence by acquiring for each shot an additional echotrain that samples the central k-space region. In this realization, the shots with excessive motion corruption will be rejected by RTSG and the shots which pass RTSG will be combined using low resolution phase maps reconstructed from the data acquired by the additional echotrains.

RTSG imaging is more suitable to identify rigid bulk movement rather than local deformation motion. It can also, however, be used to detect and monitor local motion such as swallowing, which may induce a shift of the reference peak by several Δk, as was observed during the brain DWI studies (Figure 3.8). Because swallowing does not happen frequently, the RTSG parameters may be set to screen any motion with equal or larger amplitude than swallowing. If the coil element chosen for RTSG is sensitive to local deformation motion, such as a CSF pulsation for DWI of cervical spinal cord, the RTSG test may fail too often. In such cases, the RTSG technique may be combined with cardiac gating for diffusion weighted imaging. Since each reacquisition increases the scan time by TR, the threshold values for the RTSG acceptance criteria may be increased to detect the data corruption by the large motion only, reducing the number of failures in the RTSG test.

The preliminary application of RTSG for DTI measurement on healthy human brain indicated that the directional correlations were improved by using the reject/reacquired data. Because the level of improvement depends upon the relative number of corrupted data in the total data, the improvement may not be noticeable for DTI measurements of cooperative subjects.

CHAPTER 4

SINGLESHOT T_1 MAPPING USING SIMULTANEOUS ACQUISITIONS OF SPIN- AND STIMULATED-EP IMAGING (2D SS-SESTEPI)

4.1 Introduction

The spin-echo sequence, gradient-echo pulse sequence, and their variants are commonly used for data acquisition in magnetic resonance imaging (MRI). The stimulated-echo (STE) pulse sequence is often used to investigate transport phenomena, such as molecular translational diffusion (45,46) and displacement-encoded imaging (DENSE) (47). STE is also used in localized single-voxel spectroscopy for studying short T_2 species (48). The spin-pathway can be simplified such that half of the prepared magnetization is restored into the longitudinal direction by the second 90^o RF (tipup) pulse, and the other half, which remains on the transverse plane after the tipup RF pulse, is discarded, as previously reported (9,15,49). This results in wasting of a quadrature component of the magnetization. This half magnetization can be recovered by measuring a spin-echo after the second 90^o RF pulse while simultaneously measuring the stimulated-echo (50). The additional data can be used for quantitative measurement of NMR and physical parameters such as molecular translation diffusivity, T_1 relaxation time and phase change, which is useful for characterization of other physical parameters such as temperature and physiological motion.

In dynamic contrast enhancement-MRI (DCE-MRI), the signal intensity of 2D fast gradient-echo imaging is generally used to estimate the concentration of metal ion for pharmacokinetic (PK) evaluation (51). Because of the nonlinear relationship between the NMR signal intensity and the concentration of paramagnetic-ion based contrast agent, the resultant PK parameters are subject to error and may be considered semi-quantitative. However, it is well known that $1/T_1$ is directly related to the concentration of MRI contrast agent over a wide range of concentrations (52), as in $\Delta R_1 = 1/T_1(C) - 1/T_1(C=0) = r_1C$, where r_1 and C are the relaxivity and the local concentration of the contrast agent, respectively.

T_1 measurement typically requires multiple scans with different recovery times (TR) or inversion times (TI) (53). It generally takes several tens of minutes to complete T_1 measurement using the inversion-recovery (IR) or saturation-recovery (SR) spin-echo (SE), which are the most commonly used techniques (54). Using IR-SE or SR-SE for T_1 measurement that uses the recovery process of the longitudinal magnetization, the accuracy of the measured T_1 heavily depends on whether the fully (or almost fully) relaxed signal is measured. Acquisition of the fully relaxed signal significantly increases the total measurement time due to the long recovery time (TR or TI) and limits its application only to non-dynamic imaging. Gradient-echo imaging with flip angle variation has been used with reasonable temporal and spatial resolution (53); however, the T_1 estimation obtained by this method is very sensitive to B_1 inhomogeneity. Although there have been reports on various fast T_1 mapping techniques such as 2D singleshot-EPI (2D ss-EPI) and its variants (Look-Locker EPI, IR-EPI) (55-57), and a multishot spin-echo EPI (ms-SEPI) with automated variation of TR and TE to

simultaneously measure T_1 and T_2 (58,59), there is no technique that acquires the complete data set for T_1 calculation in a single shot suitable for dynamic T_1 measurement (DTM).

In this report, a novel singleshot T_1 mapping method is presented using a spin-EPI (SEPI) and a stimulated-EPI (STEPI) that are simultaneously acquired in a single shot (2D ss- SESTEPI). Because two images are acquired after a single excitation, they have identical phase-errors, assuming that the gradient is ideal and the motion in the imaging field-of-view is negligible. The phase difference between SEPI and STEPI is independent of phase-error unless the phase is varied by location change during the mixing time TM, as for DENSE imaging (47). A major source of error using SEPI and STEPI for quantitative MRI comes from the spatially varying B_1 amplitude, which is imperfect in most MR imaging applications. Unless the second and the third RF pulses are a perfect 90^o in all locations within the imaging FOV, the prepared transverse magnetization is no longer evenly divided for spin- and stimulated-echoes by the second RF pulse and the third RF pulse does not flip the total stored longitudinal magnetization down to the transverse plane for the stimulated echo. A method has been developed to correct the difference in signal intensities in SEPI and STEPI, caused by an imperfect 90^o pulse in acquired images.

4.2 Theory

In general, three non-180^o RF pulses in Figure 2.35 form five echoes: four spin-echoes and a stimulated echo. Pairs of crusher gradient pulses, which are indicated as G_{cr} and G_{cr2} in Figure 4.1, are used to selectively refocus the prepared magnetization during the stimulated-echo acquisition, while spoiling the freshly recovered magnetization. If

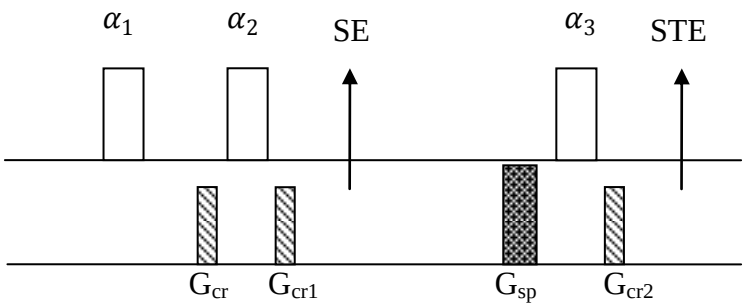

Figure 4.1. Two crusher gradients (G_{cr} and G_{cr1}) wrap around the second RF pulse. Spoiler gradient spoil the remnant transverse magnetization. The 3rd crusher gradient (G_{cr2}) immediately follow the last RF pulse to destroy the freshly magnetization during the mixing time.

$\alpha_1 = 90^o_x, \alpha_2 = 90^o_{-x}\ and\ \alpha_3 = 90^o_x$, the transverse magnetization excited by the first 90^o_x is dephased by the dephasing crusher G_{cr}, and split into two quadrature components M_I and M_Q with equal magnitudes by a perfect tipup 90^o_{-x}. *I* component M_I is rephased by the rephasing crusher G_{cr1}, and a spin-echo is formed at position "SE", and is spoiled by G_{sp} after SE acquisition in Figure 4.1. Eq. (4.1) describes the magnitude of the SE.

$$M^I_+(\vec{r}) = \frac{1}{2} M^o_+(\vec{r}) \cdot e^{-TE/T_2} \tag{4.1}$$

The *Q* component is stored in the longitudinal space and during the mixing time TM (time interval between 2nd and 3rd RF pulses), during which the fresh longitudinal magnetization also recovers. The longitudinal magnetization just before the third RF pulse is the sum of T_1 decayed prepared magnetization and freshly recovered magnetization during the mixing time TM, as in,

$$M_z(\vec{r}, TM) = M_o(\vec{r})\left(1 - e^{-TM/T_1}\right) + \frac{1}{2} M^o_+(\vec{r}) \cdot e^{-TM/T_1} \tag{4.2}$$

The third 90^o RF pulse tips this longitudinal magnetization down to the transverse plane. G_{cr2} rephases only prepared magnetization previously dephased by G_{cr}, while spoiling the freshly recovered magnetization as well as all other spin-echoes that are mirrored by the

third 90^o RF. The stimulated echo is formed at the position "STE", where the center of EPI (k_y=0) is also positioned (60). Therefore, the STE signal is only from the purely prepared magnetization, without being contaminated by the fresh magnetization.

$$M_+^Q(\vec{r}) = \frac{1}{2} M_+^o(\vec{r}) \cdot e^{-TE/T_2} \cdot e^{-TM/T_1} \tag{4.3}$$

Because the flip angles of RF pulses deviate from the perfect 90^o due to B_1 field inhomogeneity, these signal equations must be modified as follows, to include the effect from spatial variation of the B_1 field.

$$M_{SE}(\vec{r}) = f_I(\vec{r}) \cdot \frac{1}{2} M_+^o(\vec{r}) \cdot e^{-TE/T_2} \tag{4.4}$$

$$\begin{aligned} M_{STE}(\vec{r}) &= f_Q(\vec{r}) \cdot \frac{1}{2} M_+^o(\vec{r}) \cdot \ e^{-TE/T_2} \cdot \ e^{-TM/T_1} \\ &= g(\vec{r}) \cdot M_{SE}(\vec{r}) \cdot e^{-TM/T_1} \end{aligned} \tag{4.5}$$

Here, $M_{SE}(\vec{r})$ and $M_{STE}(\vec{r})$ are transverse magnetizations for the spin-echo and the stimulated-echo, and $f_I(\vec{r})$ and $f_Q(\vec{r})$ are position-dependent fractions for spin-echo and stimulated-echo, respectively. $g(\vec{r})$ is defined as $g(\vec{r}) = f_Q(\vec{r})/f_I(\vec{r})$. Because the effect on the flip angle deviation of the first RF is identical for both SE and STE, the B_1 functions $f_I(\vec{r})$ and $f_Q(\vec{r})$ are caused by B_1 field distribution of the second and third RF pulses. Note that functions $f_I(\vec{r})$, $f_Q(\vec{r})$, and $g(\vec{r})$ are spatially smoothly varying and position dependent. It is necessary to obtain the map of these B_1 correction functions to use the magnitude images of SE and STE for quantitative analysis, such as T_1 measurement.

4.3 Methods

4.3.1 Pulse Sequence Description

RF in the sequence diagram in Figure 4.2 includes both RF pulses and data acquisition windows of the MR signal. Three reference echoes (REF) are acquired immediately after the first 90^o RF for EPI phase-correction. G_{cr} and G_{sp} indicate the gradient pulses for crusher and spoiler. Both spin-echo and stimulated-echo are formed at the same echotime TE, where the effect from the field inhomogeneity is removed.

4.3.2 Effect of B_1 Inhomogeneity on T_1 Measurement

Assuming the actual flip angle of three RF pulses in stimulated-echo sequence at position $\vec{r}$ is α, not perfect 90^o, the signal intensities measured at spin-echo (SE) and

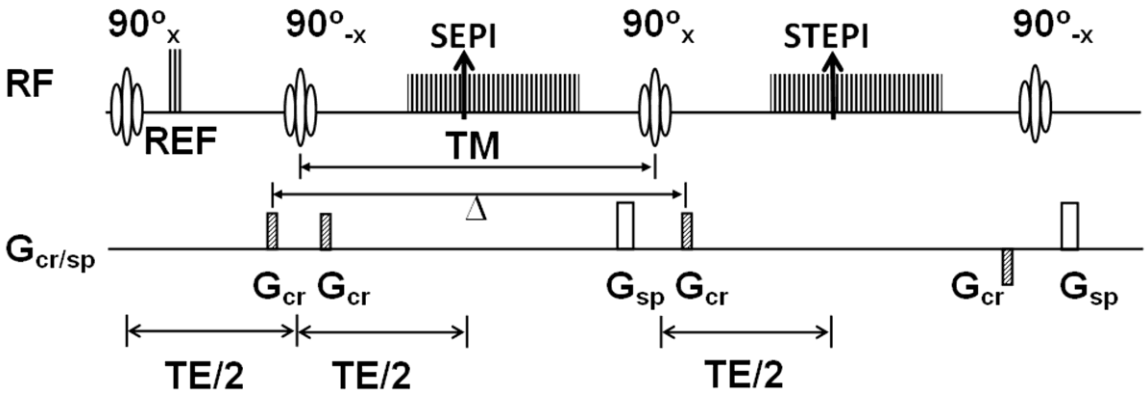

Figure 4.2. Pulse sequence diagram of 2D ss-SESTEPI using EPI readout. Two EPI images are acquired simultaneously with different T_1 decay. For perfect 90^o RF pulses, half of the magnetization is stored in the longitudinal space and the other half remains in the transverse plane after the tipup RF pulse (90^o_{-x}). The crusher gradient G_{cr} selectively rephases the prepared magnetization, while spoiling the fresh longitudinal magnetization that is recovered during TM. All imaging gradients applied after the center of the third 90^o are rewound at the center of the fourth 90^o_{-x} pulse to rephase only the freshly recovered magnetization during the TM. The last 90^o_{-x} RF pulse restores this rephased transverse magnetization back into the longitudinal space. Δ indicates the separation between two crusher gradients, which is an important parameter to estimate the diffusion-weighting.

stimulated-echo (STE) are written as (17)

$$S_{SE}(\vec{r}) = S_{+}^{o}(\vec{r})\sin(\alpha)\sin^2\frac{\alpha}{2}\cdot e^{-TE/T_2}\cdot f_R(\vec{r}) \tag{4.6}$$

$$\begin{aligned} S_{STE}(\vec{r}) &= \frac{1}{2}S_{+}^{o}(\vec{r})\sin^3\alpha\cdot e^{-TE/T_2}\cdot\ e^{-TM/T_1}\cdot f_R(\vec{r}) \\ &= S_{SE}(\vec{r})\cdot g(\vec{r})\cdot e^{-TM/T_1} \end{aligned} \tag{4.7}$$

Here, TE and TM are echo-time and mixing-time, respectively, and $f_R(\vec{r})$ the receiver function. $g(\vec{r})$ indicates the error in magnitude from the imperfect 90° RF pulses due to B_1 inhomogeneity. For α of perfect 90° RF pulses, $g(\vec{r})$ should be 1, which indicates that the signal intensity of STE differs from that of SE only by T_1 decay term $e^{-TM/T1}$. From these two equations (Eqs. (4.6) and (4.7)), the theoretical B_1 correction function $g(\vec{r})$ is obtained as

$$g(\vec{r}) = \frac{\sin^2\alpha}{2\ \sin^2\frac{\alpha}{2}} = 2\cos^2\frac{\alpha}{2} \tag{4.8}$$

The measured spin-relaxation time T_1^{meas} can be described as

$$\begin{aligned} T_1^{meas} &= \left\{\frac{\ln S_{SE}(\vec{r}) - \ln S_{STE}(\vec{r})}{\mathrm{TM}}\right\}^{-1} \\ &= \left\{\frac{1}{T_1^{true}} - \frac{1}{\mathrm{TM}}\ln\left(2\cos^2\frac{\alpha}{2}\right)\right\}^{-1} \end{aligned} \tag{4.9}$$

This equation indicates that the error in measured T_1 will differ for different mixing times as well as different actual flip angles. During the evaluation of Eq. (4.9), only the transmit function is considered without involving the difference in signal reception.

There is no need to accurately measure the actual position-dependent flipangle α(**r**). Any difference between SEPI and $STEPI_0$ with TM →0 (or TM $\ll T_1$) is directly

related to the B_1 correction function. Therefore, the correction function $g(\vec{r})$ can be experimentally measured as a part of the data acquisition by setting TM →0 (or minimum TM). As shown in the pulse sequence diagram in Figure 4.3, the data acquisition window for SEPI is removed to acquire the $STEPI_0$ image with minimal mixing time. In practice, this minimal TM was about 5 ms and the T_1 decay for typical T_1 at 3 T was less than 1 % for T_1 > 0.5 second. A B_1 correction map $g(\vec{r})$ is then obtained by dividing $STEPI_0$ by $SEPI_0$ (the averaged SEPI) as,

$$g(\vec{r}) = \frac{STEPI_0}{SEPI_0} \tag{4.10}$$

In practice, $STEPI_0$ is measured only once by pre-imaging with increased signal averaging. The same number of averages was used for $STEPI_0$ and $SEPI_0$ for the B_1 correction map $g(\vec{r})$. $SEPI_0$ was the averaged SEPI from pre-dynamic images and was not measured separately. Two ~ four complex averaging was used to acquire $STEPI_0$ and

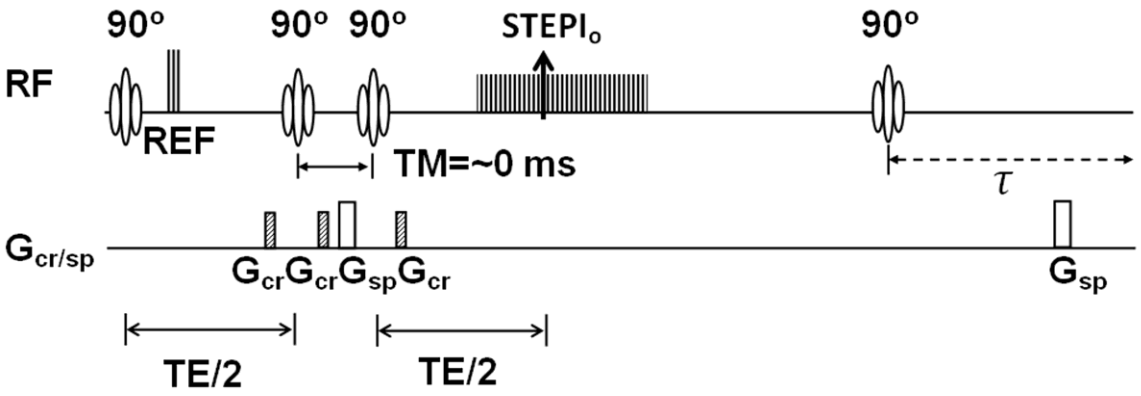

Figure 4.3. Pulse sequence to measure B_1 correction function. STEPI is acquired after three 90° RF pulses with the minimum mixing time TM to remove the T_1 decay. Subscript "0" in $STEPI_0$ indicates zero TM; therefore the difference between SEPI and STEPI is only the B_1 function. By comparing the SEPI and $STEPI_0$, the B_1 inhomogeneity effect can be removed. The fourth 90° is applied after $STEPI_0$ to achieve exactly the same recovery time as that of ss-SESTEPI.

$SEPI_0$ for the B_1 correction map $g(\vec{r})$. The inverse of B_1 correction function, $g^{-1}(\vec{r})$, calculated by using Eq. (4.10), is multiplied by STEPI signal to remove the difference caused by B_1 inhomogeneity. This correction eliminates the error in the resultant quantification that is caused by the inhomogeneous B_1. A pair of crusher gradients, indicated as G_{cr} in Figure 4.2, is crucial to spoil the freshly recovered longitudinal magnetization during the mixing time after it is flipped onto the transverse plane, while refocusing the prepared magnetization (39,60). However, the pair of crusher gradients G_{cr} along with the large mixing time ($t_{diff} = \sim TM$) induces non-negligible diffusion weighting and decreases the signal intensity of STEPI by e^{-bD}, where b and D are the diffusion-weighting factor and the diffusivity of the water molecules, respectively. Here, b is around $(\gamma A)^2 T_M$, where A is the zeroth moment of each crusher gradient G_{cr}. The signal intensity in Eq. (4.7) of the T_1-weighted STEPI needs to be modified to include the signal decay that is caused by diffusion-weighting as,

$$\begin{aligned} S_{STE}(\vec{r}) &= S_{SE}(\vec{r}) \cdot g(\vec{r}) \cdot e^{-\frac{TM}{T_1}} \cdot e^{-bD} \\ &= S_{SE}(\vec{r}) \cdot g(\vec{r}) \cdot e^{-TM(\frac{1}{T_1}+\frac{bD}{TM})} \end{aligned} \tag{4.11}$$

The measured T_1 is underestimated as,

$$\frac{1}{T_1^{meas}} = \frac{1}{T_1} + \frac{bD}{TM} \tag{4.12}$$

Therefore, the error in the measured T_1 that is caused by diffusion-induced signal loss in STE can be corrected by measuring average diffusivity D separately as a part of prescanning.

All imaging gradients applied after the center of the third excitation 90^o_x pulse are rewound at the center of the fourth restoring 90^o_{-x} RF. Only the transverse magnetization,

contributed from the fresh magnetization that is recovered during the mixing time, is rephased and the fourth 90^o RF restores this rephased magnetization back into the longitudinal space. Because the recovered fresh magnetization may be as large as 40 % for TM = ~0.5 T1 in T_1 measurement, the longitudinal magnetization before the first excitation RF will be improved, although the fresh magnetization undergoes T_2* decay during the data acquisition of STE.

MRI studies were performed on a Siemens Trio 3 Tesla MRI system (Siemens Medical Solutions, Erlangen, Germany) with Avanto gradients (45 mT/m strength and 150 T/m/s slew rate). The pulse sequence was developed based on a singleshot spin-echo EPI sequence, using the IDEA pulse sequence development environment. Real time calculation of T_1 mapping was implemented into a custom-made ICE program (Image Construction Environment). The on-line image construction program produced two magnitude images and a T_1 map for each slice.

A phantom was constructed with two 40 cc plastic bottles filled with 0.1 and 0.2 mM $MnCl_2$/water solutions, respectively, and immersed in a 0.075 mM $MnCl_2$/water solution in a rectangular acrylic container with dimensions 8x8x13 cm^3. The T_1 of each concentration was measured as 0.904 and 0.602 sec for 0.1 and 0.2 mM, respectively, using the inversion recovery turbo-spin echo (IR-TSE) with 10 s TR, 8 ms TE, 2x2x2 mm^3 spatial resolution, 128x40 acquisition matrix, 250 Hz/px receiver bandwidth, and 34 inversion times ranging from 25 to 2000 ms.

An MRI experiment was performed to investigate the effect of flip angle and mixing time TM for B_1 correction mapping on the accuracy of T_1 measurement, using a 128x40 imaging matrix with 62.5 % phase-encoding asymmetry, 2x2x2 mm^3 spatial

resolution, 1.346 kHz/pixel receiver bandwidth, 7.0 s TR, using a transmit/receive head RF coil. The echo times were 14.2 ms for both SEPI and STEPI. The experiment was repeated for the nominal flipangles of 60, 75, 90, 105, and 120^{o} and for different mixing times of 0.1, 0.2, 0.4, and 0.8 s to investigate the effect of the mixing time on the resultant T_1.

To examine the diffusion effect on the T_1 values by the crusher gradient, 2D ss-SESTEPI was applied to a fluid phantom with 0.4 s TM, 5 s TR, and 2x2x2 mm^3 resolution. T_1 of the solution was measured as 0.95 s by IR-TSE. The zeroth moment of the crusher gradients was incremented as multiples of $A_{o.}$ The zeroth moment A_o satisfies the relationship $\gamma A_o \Delta x = 2\pi$. The resultant b-factor was varied from 8 ~ 256 s/mm^2. Diffusivity of the water phantom was measured using 2D singleshot diffusion-weighted EPI with b=0 and 500 s/mm^2. Eq. (4.12) was used to simulate the T_1 underestimation by diffusion-weighting.

2D ss-SESTEPI was applied on a healthy human brain to acquire T_1 mapping images with imaging parameters of 84x128 acquisition matrix, 2x2x2 mm^3 spatial resolution, 7 s TR, 21.7 ms TE, 256x168 mm^2 FOV, 1.346 kHz/pixel receiver bandwidth, and 0.6 s TM. B_1 correction map was calculated from eight prescanning images. T_1 maps were computed by taking multiple measurements and calculating the averages of SEPI and STEPI in 1, 4 and 16 repetitions, respectively. T_1 map imaging was also acquired using IR-TSE for the same locations with 10 s TR, 16 ms TE, 256x192 matrix, 1x1x2 mm^3 spatial resolution, 11 echo-train-length, and 250 Hz/pixel receiver bandwidth for twelve different TIs (36, 70, 100, 200, 400, 500, 600, 800, 900, 1200, 1800 and 2400 ms). B-factor was estimated as 23.8 s/mm^2 within the pulse sequence. The imaging protocol

was approved by the Institutional Review Board, at the University of Utah, and informed consent was obtained from the volunteer.

2D ss-SESTEPI was applied to invivo dynamic T_1 mapping MRI of two tumor-bearing female nude mice (61), using a home-made quadrature transmit/receive saddle coil with 1.5 inch inner-diameter and 3 inch length and imaging parameters: in-plane resolution of 1x1 mm^2 with 2 mm slice thickness, 128x32 imaging matrix, 5.0 s TR, 120 total repetitions (time frames) for 10 min, TEs 15 msec for both SEPI and STEPI. The first 4 measurements were used to acquire $STEPI_o$ images for B_1 correction mapping. T_1 maps were constructed from the time frame 5. Contrast agent was administered after 8 repetitions, i.e., acquisitions of four $STEPI_o$ and four precontrast scans. MultiHance (Gadobenate dimeglumine: Gd-BOPTA, Bracco Diagnostics, Inc.) was injected via the catheterized tail vein to a dose of 0.1 mM Gd/kg. Animals were cared for under the guidelines of a protocol approved by the University of Utah Institutional Animal Care and Use Committee.

4.4 Results

4.4.1 Simulation of Error on T_1

Eq. (4.9) was used to simulate the anticipated error in the T_1 estimation with respect to the actual flip angle and mixing-time without B_1 inhomogeneity correction, as shown in plots in Figure 4.4. The measured T_1 tends to be prolonged with a short mixing time and a flip angle smaller than 90^o and shortened with the actual flip angle larger than 90^o. As indicated in Eq. (4.9), the estimated T_1 agrees with the true T_1 for a perfect 90^o flip angle regardless of TM, as indicated by the vertical arrow in Figure 4.4.

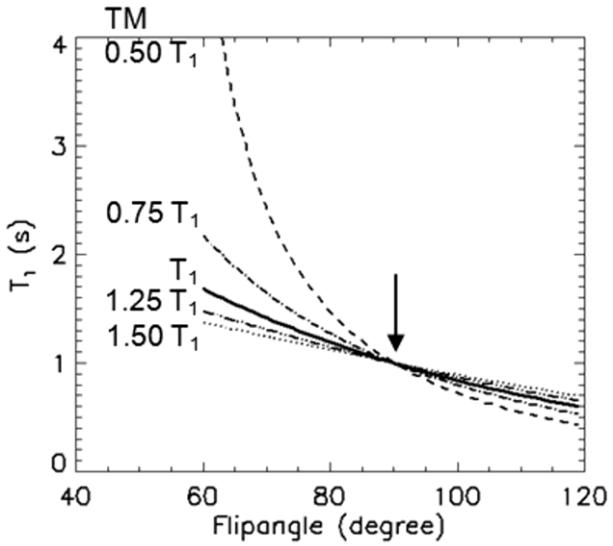

Figure 4.4. Simulated T_1 values with respect to RF flipangle α without B_1 correction using eq. 4 with the mixing times TM = 0.50, 0.75, 1, 1.25, 1.5 T_1 from top to bottom. 1.0 s was used for the true T_1. The measured T_1^{meas} deviates further from the true value with smaller TM and larger difference in flipangle α from 90°. Vertical arrow indicates the measured T_1 = true T_1 with 90° pulses.

4.4.2 B_1 Correction Process

Figure 4.5 shows the T_1 calculation process: 4-averaged magnitude images of $SEPI_o$ (Figure 4.5a) and $STEPI_o$ (Figure 4.5b) to calculate the B_1 correction map, the computation result of B_1 correction map $g(\vec{r})$ (Figure 4.5c), singleshot images of SEPI (Figure 4.5d) and STEPI (Figure 4.5e). Figure 4.5f and Figure 4.5g show T_1 maps before and after B_1 correction, respectively. The plots in Figure 4.5h and Figure 4.5i are T_1 values along the horizontal dotted lines on the resultant T_1 maps of Figure 4.5f and Figure 4.5g, and display almost complete elimination of the B_1 inhomogeneity effect.

4.4.3 Flip Angle Variation

To investigate the effects of flip angle variation on the resultant T_1 value, a T_1 map was acquired using 2D ss-SESTEPI with nominal flip angles 60, 75, 90, 105, and

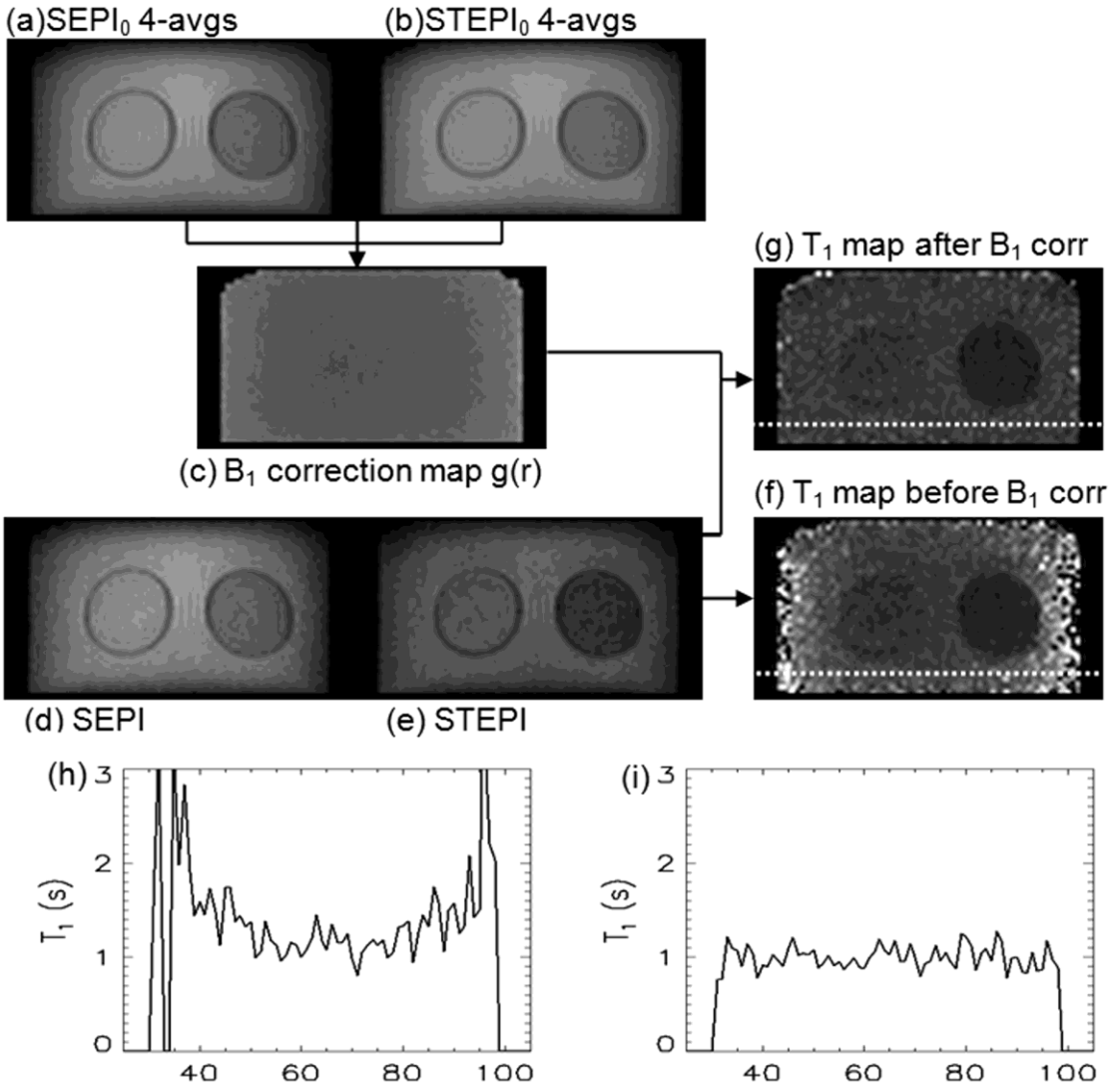

Figure 4.5. B_1 correction process: four averaged (a) $SEPI_o$ and (b) $STEPI_o$ images to calculate (c) B_1 correction map, which is used to correct singleshot (d) SEPI and (e) STEPI. (f, g) are T_1 maps before and after B_1 correction, respectively. T_1 values of water protons in $MnCl_2$ along the horizontal dotted lines are presented in plots (h) and (i) for before and after B_1 correction, respectively. T_1 map (g) and plot (i) clearly indicate substantial improvement by B_1 correction**.**

120^o for the second and third RF pulses in Figure 4.2, using a 0.4 sec mixing time, and four-averaged B_1 correction map. Mean T_1 values on regions-of-interest (ROIs) of 0.1 and 0.2 mM solutions are plotted in Figure 4.6a and Figure 4.6b. Closed and open symbols represent T_1 measurements before and after B_1 correction, and circles and square symbols indicate 0.1 and 0.2 mM $MnCl_2$ concentrations, respectively. The dotted and broken lines are guidelines to the T_1 plots without B_1 correction. Solid horizontal lines indicate T_1 values measured using IR-TSE imaging. These results demonstrated significant improvement in accuracy by B_1 correction for all values of T_1 (0.2 ~ 1.3 sec.). Plots in (b) are T_1 values in (a) normalized to T_1=1.0 s to compare the empirical data to the simulated plot in Figure 4.4. TM of 0.4 s corresponds to 0.44 T_1 for T_1=0.904 s and 0.66 T_1 for T_1=0.602 s for 0.1 and 0.2 mM $MnCl_2$ concentrations, respectively. Plots in Figure 4.6b show good agreement with the theoretical simulation in Figure 4.4 and robustness of the B_1 inhomogeneity correction.

4.4.4 TM Variation

To improve the accuracy of T_1 measurement using 2D ss-SESTEPI, the signal difference between SEPI and STEPI must be significantly larger than the noise amplitude, otherwise the resultant measurement will be dominated by noise, rather than T_1 decayed signal change. The T_1 map was acquired using 2D ss-SESTEPI with a nominal flip angle of 90^o and a four-averaged B_1 correction map for variable mixing times of TM = 0.1, 0.2, 0.4, and 0.8 sec. The mean and standard deviation were measured on ROIs selected on each concentration and plotted with respect to the mixing time in Figure 4.7. Error bars on the plots indicate the standard deviation of each measurement. These plots indicate that the uncertainty of the measurements greatly depends on the selection of TM. T_1

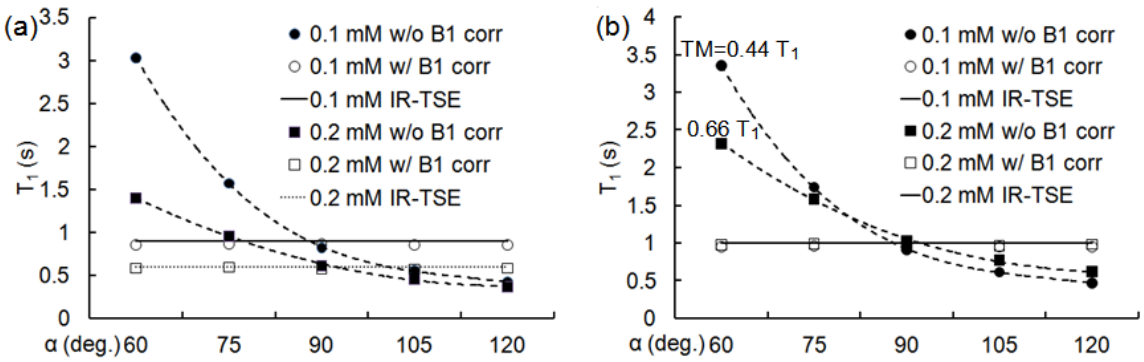

Figure 4.6. T_1 measurement before (●, ■) and after (○, □) B_1 correction. The data in (a) are actually measured T_1 values, and those in (b) were normalized T_1 to 1.0 s to compare with the theoretical plots in Fig. 3. Dotted and broken lines indicate guidelines. Horizontal solid-lines represent T_1 using IR-TSE MRI.

measurement using the increased TM produces increased accuracy and reduced errors; However, it limits the number of slices in an interleaved multislice scan. For T_1 below 1.0 sec, the difference in uncertainty for measurements with 0.4 sec and 0.8 sec TM is not significant.

4.4.5 Diffusion Effect on T_1 estimation

Open squares (□) in Figure 4.8 are measured T_1 values. Diffusivity was measured as 2.14×10^{-3} mm^2/s. The dotted line indicates the simulated T_1 values using Eq. (4.12) with respect to the diffusion-weighting by the crusher gradients, using T_1 = 0.95 s, D = 2.14×10^{-3} mm^2/s. These plots demonstrate a substantial decrease in the measured T_1 with the increased diffusion-weighting by increased crusher area.

4.4.6 In vivo Measurement of Human Brain T_1 Map

Images in Figure 4.9 are T_1 maps computed from (b) IR-TSE and (c~e) 2D ss-SESTEPI. T_1 values were measured for selected regions of gray and white matter (GM, WM) as shown on T_2 weighted image in Figure 4.9a. Mean values are listed in Table 4.1.

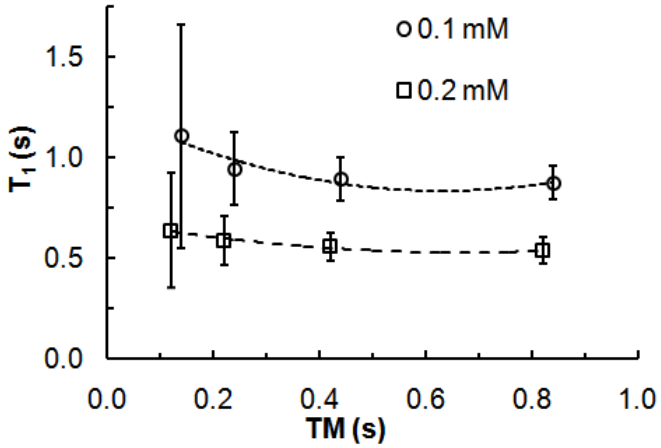

Figure 4.7. Plots of T_1 values of ROIs for each concentration of $MnCl_2$ with a 90^o nominal flipangle and four-averaged B_1 correction map for different mixing times, TM = 0.1, 0.2, 0.4, and 0.8 second. Dotted and broken lines are the guidelines of each data. Error bars represent the Standard Deviation of the means.

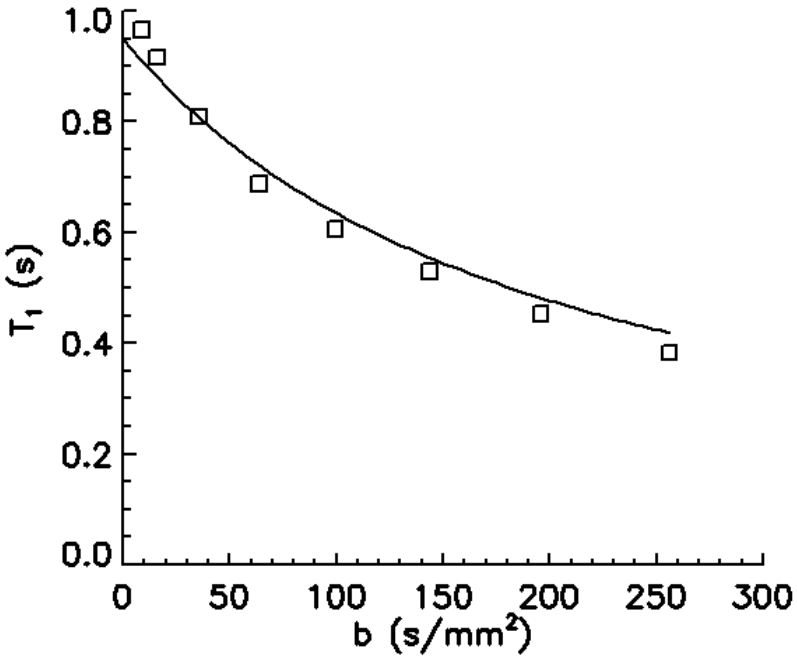

Figure 4.8. Plot of measured (□) and simulated (solid line) T_1 values with respect to b-factor. A T_1 of 0.95 s and diffusivity D of 2.14×10^{-3} mm^2/s were used for the simulation. T_1 and D were independently measured using inversion-recovery turbo spin-echo and 2D ss-DWEPI, respectively. This plot indicates dramatic underestimation of T_1 by diffusion effect.

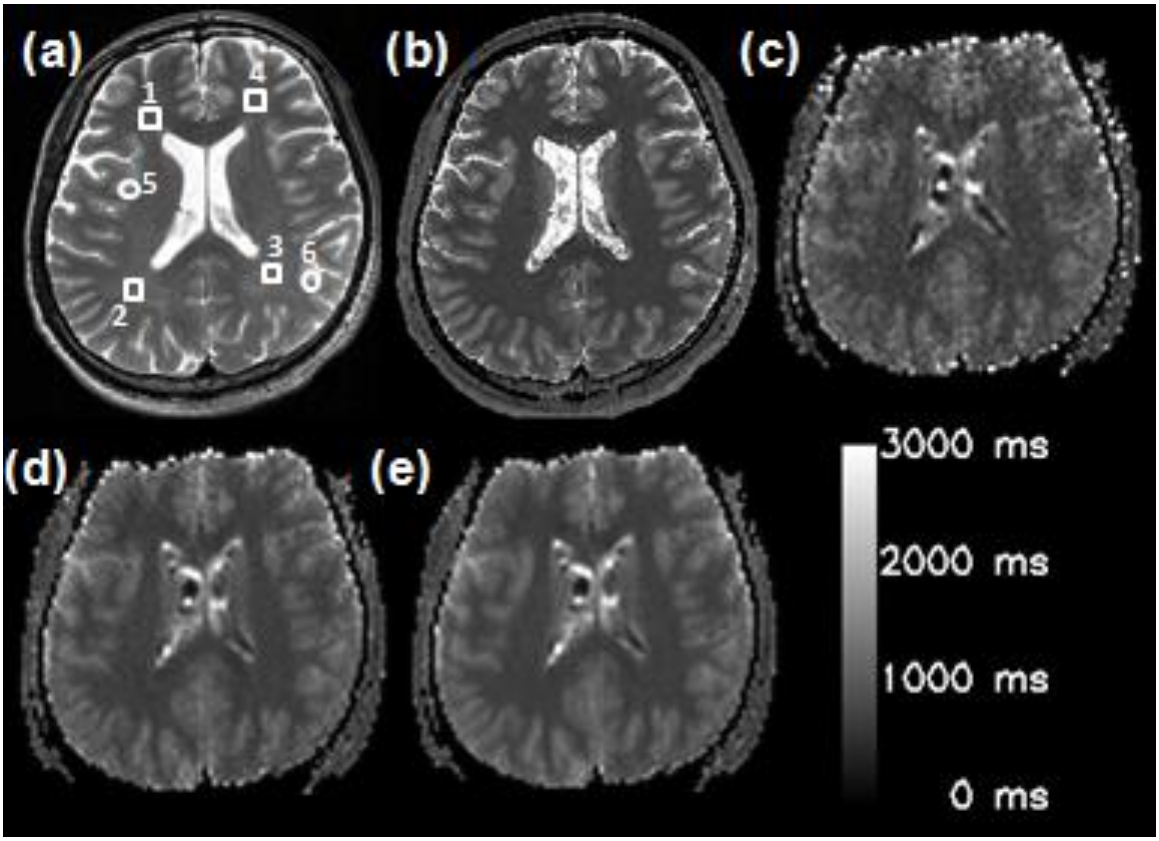

Figure 4.9. T_1 maps calculated from different signal averages. **(**a) T_2–weighted image, and T_1 maps using (b) IR-TSE and 2D ss-SESTEPI with signal averages of (c) 1, (d) 4, and (e) 16. ROIs are indicated by the square (white matter) and circles (gray matter). ROIs (1~4) and (5, 6) indicate white and gray matters, respectively.

Table 4.1: T_1 relaxation time of gray and white matter at different regions of interest shown in Figure 8. 1 avg, 4 avg and 16 avg indicate multiple repetition average for SEPI and STEPI obtained by 2D ss-SESTEPI.

	Region	IR-TSE (ms)	2D ss-SESTEPI (ms)		
			1 avg	4 avg	16 avg
White matter	1	722±33	799±58	721±41	728±20
	2	716±26	727±68	726±30	722±20
	3	733±32	772±78	747±29	744±27
	4	685±33	742±89	725±40	715±27
Gray matter	5	1276±90	1149±54	1101±61	1116±81
	6	1177±90	1069±71	1087±80	1088±58

No significant difference was observed in the T_1 values of WM between IR-TSE and 2D ss-SESTEPI. The increased standard deviation of T_1 values measured by 2D ss-SESTEPI is because of the relatively poor SNR. However, T_1 values measured using 2D ss-SESTEPI in GM were about 10 % smaller than that using IR-TSE.

4.4.7 In vivo Measurement of Singleshot T_1 in a Mouse

Images in Figure 4.10 are (a) T_1 maps and (b) ΔR_1 maps of selected time frames (every 30 sec.). T_1 maps of 10 slices were obtained every 5 sec. Images in Figure 4.10c are T_1 weighted spin-echo images of pre-contrast and 10 min after the injection. The brightness represents the larger values in T_1 and ΔR_1 maps. ΔR_1 was plotted in Figure 4.10c for several selected ROIs of 9 pixels and all at the 10 minute time point. Regions of

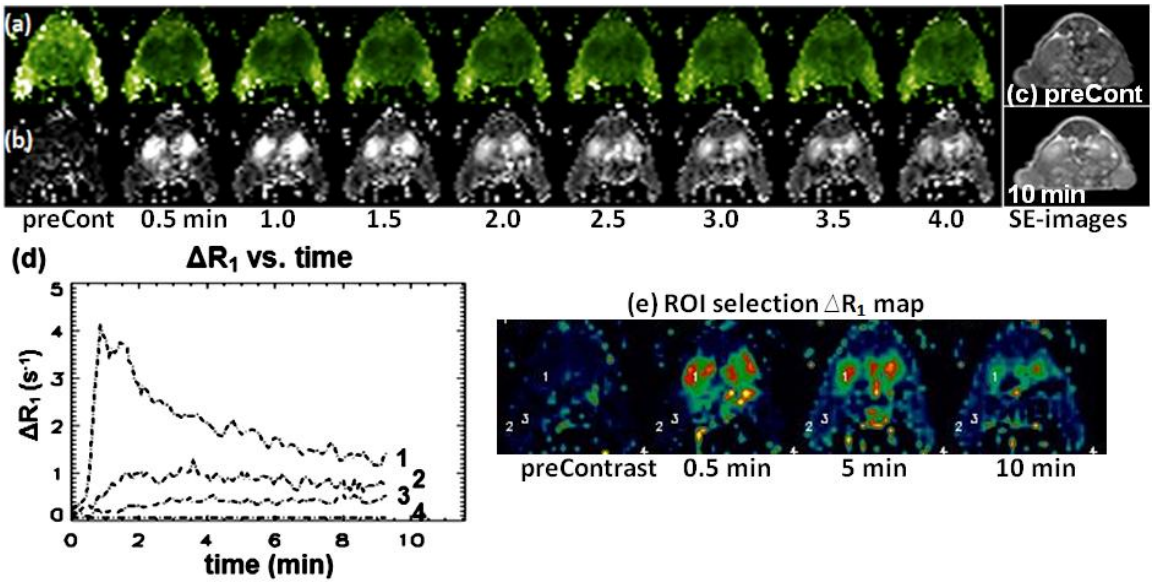

Figure 4.10. Selected images of singleshot T_1 mapping using 2D ss-SESTEPI in a tumor bearing nude mouse: (a) T_1 maps, (b) ΔR_1 map, (c) T_1 weighted spin-echo images of various time points. The temporal resolution (TR) was 5 sec, with 1x1 mm^2 resolution and 2 mm slice thickness. (d) Time curves of selected ROIs in (e) ΔR_1 maps in a tumor bearing nude mouse. Numbered labels in the plots indicate the 9-pixel (18 μL) ROIs on ΔR_1 maps; 1/kidney, 2/tumor periphery, 3/tumor core, and 4/noise.

3x3 pixels (18 μL volume) were selected at kidney, tumor periphery, tumor core, and muscle. These data can be used for further pharmacokinetic evaluation pixel-by-pixel or by organ.

4.5 Discussion

B_1 inhomogeneity correction was very successful with an experimentally measured correction map using the 2D ss-SESTEPI pulse sequence. Eq. (4.9) and (4.10), which describe the error in the T_1 estimation using SEPI and STEPI without correction of B_1 inhomogeneity, include only the transmit function without signal reception. The measured B_1 correction map, however, reflects all inhomogeneity causes including RF transmission and NMR signal reception, except for T_1 and diffusion-weighted decays. The simulated plots in Figure 4.4 agreed very well with the measured T_1 in Figure 4.6, which indicates that the correction method for B_1 inhomogeneity is very robust. The only difference is a systematic underestimation. This probably results from diffusion-induced signal decay with the long diffusion time.

The accuracy of the resultant T_1 value using 2D ss-SESTEPI decreased with a lower TM/T_1 ratio because there is not enough change in the T_1 decay with a short TM, as shown in Figure 4.7. Although the plots indicate that the measured T_1 is more accurate with increased TM/T_1, we have observed greatly decreased accuracy for very short T_1 and large TM. This is because there was no signal left when TM is greater than 2~3 times T_1. The choice of mixing time, therefore, depends on the spin-relaxation time of interest. For instance, one may be interested in $T_1 < 1$ s in DCE-MRI and T_1 decreases with increased local concentration of MRI contrast agent. 0.4~0.5 s TM may be suitable for dynamic T_1 mapping using paramagnetic-ion based contrast agents.

The T_1 value was greatly underestimated for an increased crusher area, as shown in Figure 4.8. This diffusion-induced error in the T_1 calculation is reduced by minimizing the zeroth moment *A* of the crusher gradients. However, the minimum area of the crusher gradient must be sufficient to spread the spin phase more than 2π within an imaging voxel, as in $\gamma A \cdot \Delta x > 2\pi$ for a smallest voxel dimension Δx. The b-factor was within the range of 10 ~ 30 s/mm^2 for TM 0.4 s and 1~2 mm pixel dimension. For a typical diffusivity of 1.0×10^{-3} mm^2/s in tissue water, the diffusion-weighted decay was 1~3 %, which may be ignored because it is within the noise level for STEPI images with SNR = ~ 30.

The important advantages of using 2D singleshot EPI are that the resultant images are free from motion-related artifact and have the highest signal-to-noise ratio (SNR) per fixed imaging time, which are crucial for quantitative MRI. However, 2D ss-EPI is very sensitive to the local variation of a nonlinear background gradient caused by magnetic susceptibility at or near the tissue/air and tissue/bone interfaces, as on mouse images in Figure 4.10. The resultant images suffer greatly from major geometric distortion that renders images useless. For singleshot EPI type acquisition, geometric distortion often becomes the largest limitation and its application is mostly restricted to diffusion and functional MRI of the intracranial brain, far from the sinus and the temporal bone. Therefore, it is crucial to reduce the susceptibility artifact in EPI images using 2D ss-SESTEPI before it may be useful for other applications. Because the degree of geometric distortion in 2D ss-EPI is proportional to the imaging field-of-view (FOV) in the phase-encoding direction, it can be reduced by using the reduced phase FOV. However, imaging a limited FOV in large surroundings induces aliasing in the phase-encoding

direction in conventional MR imaging. The aliasing artifact can be completely removed while accomplishing interleaved multislice imaging by using double inversion/refocusing RF pulses with slice selection gradients applied perpendicular to imaging RF pulses (43,60) or 2D spatially selective excitation (62).

Although the technique measures the T_1 in a singleshot in a few seconds and the source images have low SNR, the resultant T_1 values were comparable to those measured using inversion-recovery TSE. Average T_1 values of GM and WM using 2D ss-SESTEPI and IR-TSE are summarized with other reported values (63-66) in Table 4.2. There is large variation among different reports, which may be because of different acquisition techniques. T_1 in GM measured using 2D ss-SESTEPI was about 10 % lower than that using IR-TSE, while T_{1s} in WM were similar to each other. This underestimation may result from the diffusion-induced signal decay in STE of SESTEPI. According to the literature (67), mean apparent diffusion coefficient (ADC) in posterior left white matter are 0.67×10^{-3} mm^2 /s, while typical ADC in cortical gray matter is described as 1.0×10^{-3} mm^2/s**.** Theoretical underestimation of T_1 was calculated as 0.69 s and 1.169 s for GM and WM, respectively, using Eq. (4.12) with TM=0.6 s and b=23.8 s/mm^2, assuming true T_1 is 0.714 s (WM) and 1.226 s (GM) obtained using IR-TSE.

Table 4.2: Comparison of measured T_1 values with previously reported values for gray and white matter in the brain at 3T.

	White Matter (ms)	Gray Matter (ms)
2D ss-SESTEPI	727±12	1102±50
IR-TSE	714±21	1226±67
Literature (63)	832±10	1331±13
Literature (64)	1084±45	1820±114
Literature (65)	1110±45	1470±50
Literature (66)	933±15	1380±59

These values are 3.0 and 4.6% different from T_{1s} measured using IR-TSE. As presented, rapid T_1 mapping may be useful for non-invasive measurement of the concentration of the paramagnetic ion-based contrast agent. In the preliminary application of the technique for DCE-MRI on mice, the limiting factor for increased temporal resolution was signal-to-noise ratio. If a sufficient SNR is available by using a high-sensitivity RF coil or high-field MRI system, both temporal and spatial resolution can be improved.

CHAPTER 5

SNR IMPROVEMENT AND REDUCTION OF GEOMETRIC DISTORTION IN 3D SINGLESHOT DIFFUSION-WEIGHTED STIMULATED EPI (3D SS-DWSTEPI)

5.1 Introduction

Diffusion-weighted MRI (28) such as 2D singleshot diffusion-weighted EPI (2D ss-DWEPI) used to serve as the detection of abnormal water diffusion in the brain (e.g., ischemic stroke) (68,69) while diffusion tensor imaging (DTI) is used as the study of the anisotropic tissues (42,44,70). For example, DTI plays an important role in studying the optic nerve (71) and multiple sclerosis (72). However, DWI/DTI still face such challenges as limited resolution, substantial susceptibility artifacts and sensitivity to eddy currents causing geometric distortion (73,74). To overcome these disadvantages, segmented echo planar imaging technique (23,75-77) has been developed.

Although susceptibility artifact is reduced using segmented EPI, other artifacts such as ghosting are introduced by signal discontinuities and motion-related errors (36). Most of multishot DWI acquisition techniques suffer from the instability of phase errors between shots due to global or local motions during application of the large diffusion gradients. Reasonable success has been achieved with techniques that use navigator echoes to detect and correct phase errors (36,37,41,78), and non-EPI approaches that are

less sensitive to phase errors. Because most of them are 2D acquisition techniques, they generate relatively poor resolution along the slice direction.

Kuhl et al. (79) applied a SENSE technique on single shot spin-echo EPI to achieve higher quality images with substantial reduction of image distortions and blurring. But a coil sensitivity map was needed for both the image homogeneity correction and the SENSE reconstruction. The limitation is that it is difficult to obtain an adequate standard of reference. Moreover, the signal-to-noise ratio (SNR) is reduced due to under-sampled k-space data.

Because the use of diffusion weighted stimulated echo (DWSTE) can increase diffusion weighting without significant signal loss due to T_2 decay and is beneficial for tissues with short T_2 and long T_1, the combination of DWSTE and 3D acquisition technique can make further improvement in image quality. For instance, 3D singleshot DW STimulated-EPI (3D ss-DWSTEPI) (60,80) was developed to provide high resolution DTI. The entire 3D k-space data from a localized volume after a single excitation and a diffusion-weighting preparation is sampled. The EPI readout time is shortened by using an inner volume imaging (IVI) technique along the phase-encoding direction (23,81). A high resolution image can be acquired with reduced geometric distortion. 3D ss-DWSTEPI, however, suffers from a low SNR because it uses only half the diffusion-weighted magnetization stored in the longitudinal space by a 90^o RF and spoils the other half.

This section will describe how the 3D ss-DWSTEPI pulse sequence was modified to obtain parallel imaging reference data to further reduce the susceptibility-related artifact. The degree of susceptibility-induced distortion in EPI-type acquisitions is

inversely proportional to the speed of the k-space traveling in the phase-encoding direction, which is proportional to the phase FOV. To improve the SNR and reduce susceptibility-induced distortion, a parallel imaging technique (GRAPPA) (24) has been implemented in 3D ss-DWSTEPI to reduce the geometric distortion and a method was developed to improve the SNR by utilizing the whole diffusion-weighted magnetization.

5.2 3D Diffusion Weighted Stimulated Echo Pulse Sequence

Stimulated echoes have several useful applications in imaging and localized spectroscopy (82,83). A 2D diffusion weighted stimulated echo pulse sequence is depicted in Figure 5.1. A spoiler gradient (sp) destroys any remaining transverse magnetization. A crusher gradient (Cr2) eliminates any freshly recovered magnetization, while refocusing previous transverse magnetization. An α RF pulse tips the stored longitudinal magnetization back into the transverse plane.

3D singleshot diffusion weighted stimulated EPI pulse sequence is shown in Figure 5.2. α_n RF pulse flips a portion of the stored magnetization into the transverse plane for a slice encoding k_z. Once we determine the total slice encoding number, flip angles of each excitation can be found. To evenly distribute the prepared longitudinal magnetization for all k_z encodings, the following relationship (60) between the flip angles α_{n-1} and α_n is used:

$$tan(\alpha_{n-1}) = sin\alpha_n \cdot e^{-\tau/T_1} \qquad (5.1)$$

The last flip angle is set to 90^0 to use up all the remnant longitudinal magnetization. As the equation indicates, this relationship works for a specific T_1 value. Because the technique was intended for DTI of nerve at 3T, a T_1 of 1 sec was used.

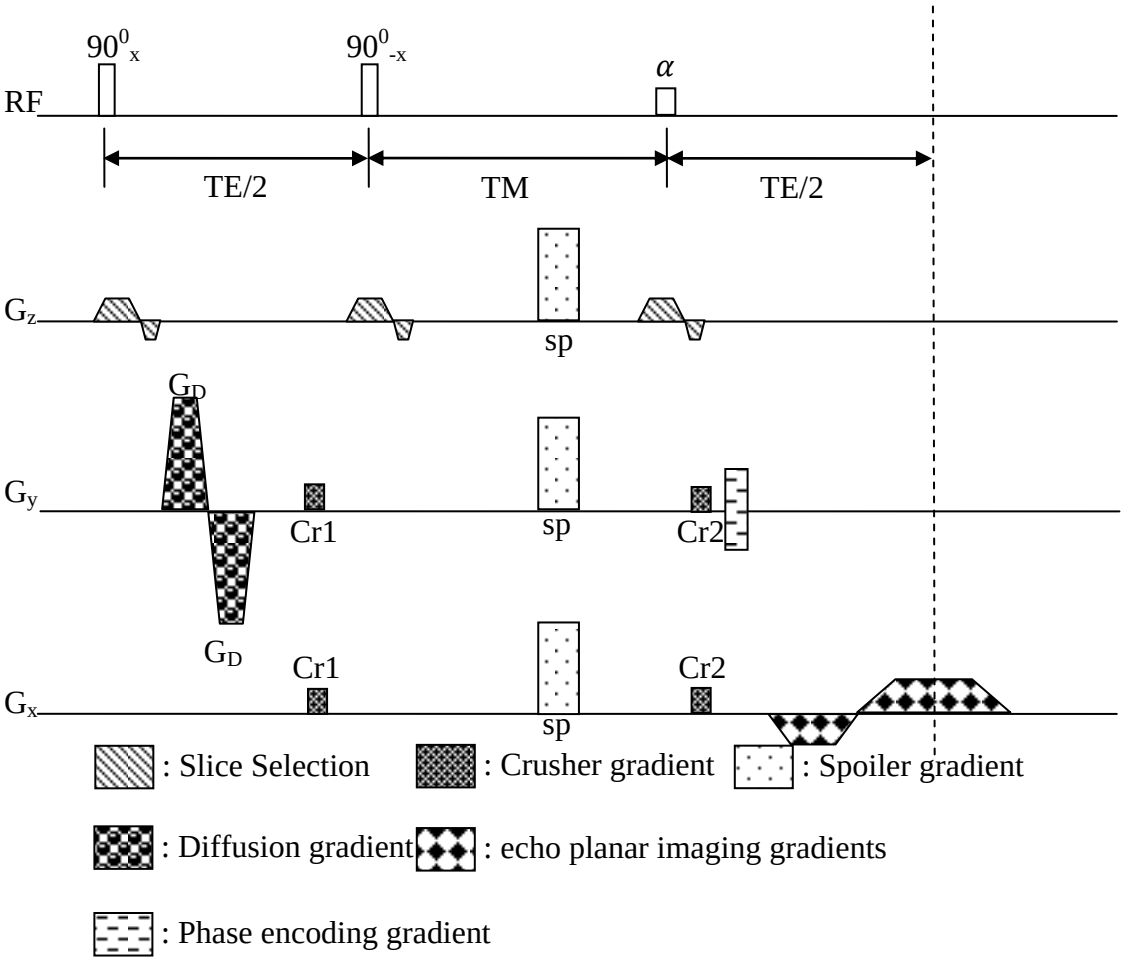

Figure 5.1. 2D single shot diffusion weighted stimulated echo pulse sequence.

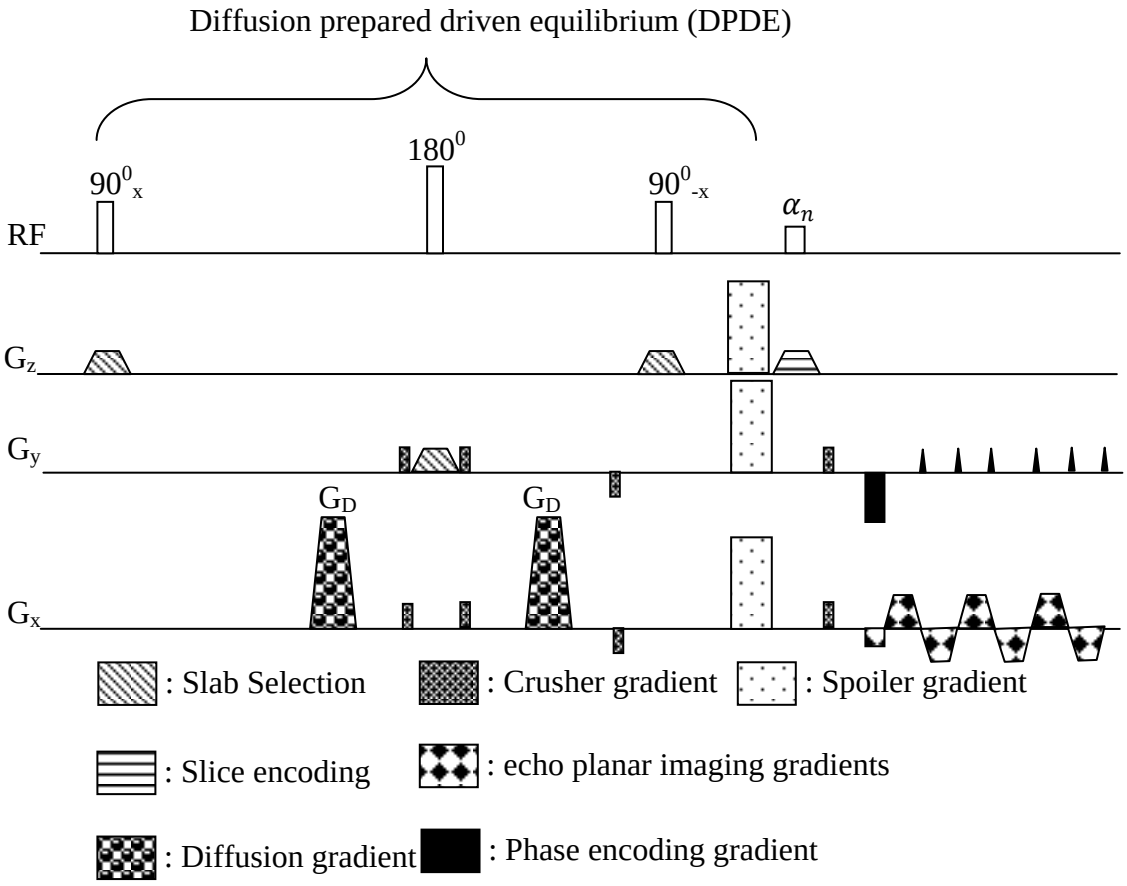

Figure 5.2. 3D single shot diffusion weighted stimulated EPI pulse sequence.

However, this technique is subject to a blurring in the slice direction due to the uneven distribution of the longitudinal magnetization for tissues with T_1 different from 1 sec. The combination with the inner volume imaging technique (81) results in availability of acquiring the entire 3D k-space data from a localized volume after a single diffusion-weighting preparation. However, it suffers from a low SNR because (1) only half the diffusion-weighted magnetization, which is stored into the longitudinal plane by a 90^0 RF pulse, is used and the other half is spoiled, and (2) number of NMR data in the k_y direction is reduced.

In the 3D ss-DWSTEPI pulse sequence, in-plane readout is shortened by reducing the FOV in the phase encoding direction. The reduced FOV (rFOV) approach is used to image a small FOV in the phase direction without aliasing artifacts from the signal outside the imaging FOV. rFOV partly reduces the geometric distortion, which is the major limitation of using the conventional 2D ss-DWEPI. The susceptibility artifact can be further decreased by using parallel imaging. A spin-echo can be used to improve the SNR of the sD-ss-STEPI from the transverse magnetization that was discarded.

5.3 Materials and Methods

Parallel imaging was implemented only in the phase-encoding direction because the number of slice-encodings in 3D ss-DWSTEPI is small (8 ~ 24). The original 3D-ss-DWSTEPI sequence was modified to acquire reference data (ET_{PI}) for parallel imaging as shown in Figure 5.3. The ET_{PI} dataset was acquired only once for multiple repetitions.

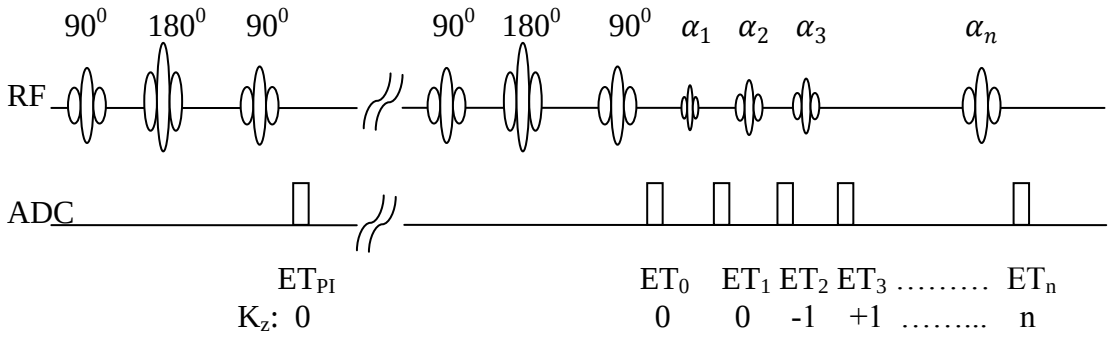

Figure 5.3. Schematic diagram of 3D-ss-DWSTEPI combined with Parallel Imaging (PI) data acquisition. Reference data for multidimensional GRAPPA reconstruction is acquired by ET_{PI} readout. 90^0 RF Tip-Up pulse transfers half of the diffusion-weighted magnetization to the longitudinal direction. This magnetization is sampled by ET_1, ET_2 , … ET_n readouts. Each readout covers the complete k_x-k_y plane for different k_z views. Flip angles (α_1, α_2,.. α_n) for the readouts are adjusted according to a variable flip angle scheme. Another half of the magnetization is sampled by ET_0 readout immediately after the 90^0 tip-up RF pulse. Both ET_0 and ET_1 readouts acquire k_z=0 plane of 3D k-space.

In the original 3D-ss-DWSTEPI, the diffusion weighted magnetization that is left in the transverse plane after the tip-up 90^o RF pulse was spoiled. In the new 3D-ss-DWSTEPI, this magnetization is sampled by the echotrain ET_0 that can form a thick slab 2D image. The k_z=0 plane of 3D k-space is sampled twice by ET_0 and ET_1 readouts. To improve image SNR, these readouts are combined as follows.

The ratio between the peak magnitude S_{ET0} of the echotrain ET_0 and S_{ET1} of ET_1 was calculated as $SF = \max(S_{ET1})/ \max(S_{ET0})$ and used to scale the ET_o readout down to the same magnitude as that of the corresponding image ET_1 readout. Two echotrains ET_0 and ET_1 were then combined to construct new k-space data (ET_{new}) for k_z=0 using the expression: $S_{new}=(S_{ET1}+SF^{2\cdot} S_{ET0})/(1+SF)$. The acceleration factor (R) was set to 2 for ET_0-ET_n readouts. Each readout covers the complete k_x-k_y plane for 3D k-space. To reconstruct missing k_y views in the readouts, multidimensional realization (84,85) of the GRAPPA algorithm (24) was implemented. The missing k_y lines were derived according to the reconstruction coefficients computed from the reference data acquired by ET_{PI} readout.

Imaging experiments were performed on a 3 T clinical MRI system (Trio-Tim, Siemens Medical Solutions, Erlangen, Germany) with Avanto gradients (40 mT/m strength and 150 T/m/s slew rate) using a 12-channel head coil. One experiment was designed to demonstrate the SNR improvement gained from our data combination method. During our measurement, the number of slice was gradually increased.

Phantom images were acquired with the following imaging parameters: slab thickness 20 mm, bandwidth 1.086 kHz/pixel, TR/TE 4000/61 ms for R=1 and 4000/46

ms for R=2, FOV 256x120 mm, acquisition matrix 128x60x10, and b=100 s/mm^2 along the slice direction.

5.4 Results and Discussions

5.4.1 Phantom Studies

The images shown in Figure 5.4 demonstrate the improvements in 3D ss-DWSTEPI image quality: (a) → (b): reduction of geometric distortion using parallel imaging, (b) → (c): SNR improvement using the combined k_z=0 data. The SNR of the R=2 image is similar to that of the R=1 image due to a shorter TE for the R=2 image. The actual ETLs were 60 and 30, and corresponding TEs were 61 and 46 ms for R= 1 and 2, respectively. The SNR of image (c) increased about 3% compared with that of image (b). This was because the k_z=0 plane of 3D k-space dataset was sampled twice and the data were combined.

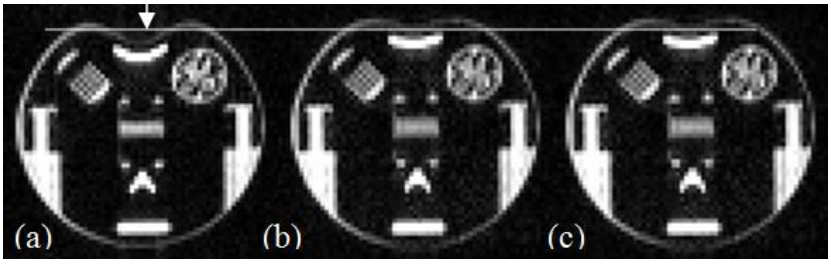

Figure 5.4. Phantom images (a) and (b) reconstructed from complete data (R=1) and partial data (R=2), respectively. The vertical arrow indicates a shift of the water signal due to the local field variation. The horizontal solid line is the guideline to measure the geometric shift due to the local susceptibility field. The susceptibility artifact was halved using parallel imaging with R=2. Image (c) was reconstructed using parallel imaging and the new k_z=0 data (weighted sum of ET_0 and ET_1).

Figure 5.5 shows the SNR improvement factor with respect to the number of partitions in a slab, Improvement in SNR was significant at low number of slices; however, it was negligible for the number of slices above 10. As the number of partitions increases, flip angles (α_1, α_2 ,…α_n) also are adjusted during our experiments.

5.4.2 Human Studies

The performance of our pulse sequence was tested on a volunteer. A healthy volunteer was given written informed consent according to an Institutional Review Board-approved protocol before the imaging experiment. The result of experiment is shown in Figure 5.6. The acquisition matrix was 160x26x10 and 160x13x10 and corresponding TEs of 62 and 55 ms for R=1 and 2, respectively and with slab thickness 20 mm, T R:4000 ms ,and b value: 500 s/mm2, FOV:240x60 mm2. From (a) to (b), spinal cord distortion is reduced. From (b) to (c), SNR of the image with combined k_z=0 data improves about 7% with respect to that of the uncombined image.

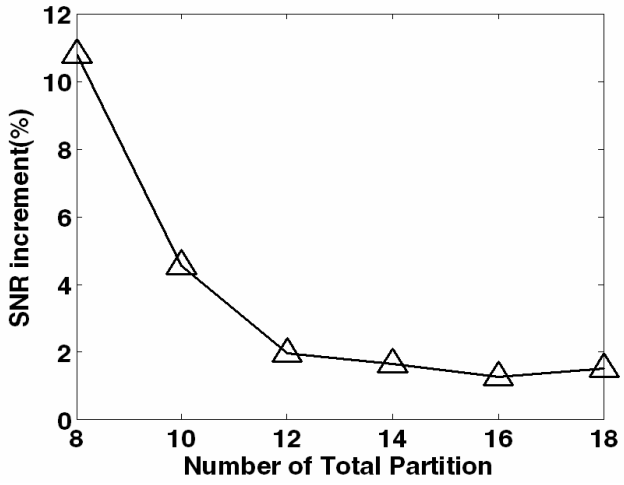

Figure 5.5. This plot shows SNR increment ratio between image combined with ET_0 and image without ET. SNRincrement=100*($SNR_{combined}$-$SNR_{uncombined}$)/($SNR_{uncombined}$). Increased number of partitions leads to smaller SNR increment.

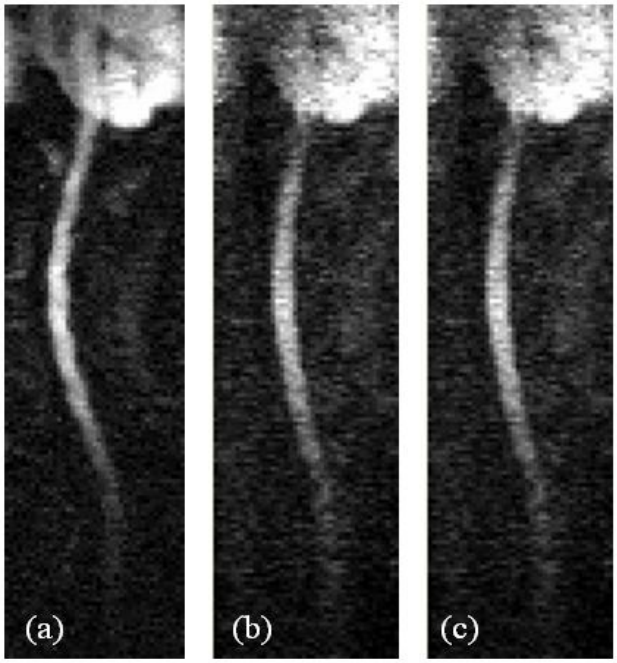

Figure 5.6. Human spinal cord eight-average diffusion weighted image (a) and (b) reconstructed from complete data (R=1) and partial data (R=2), respectively. (c) Image reconstructed from the combined k_z=0 data. In image (b) and (c), spinal cord geometric distortion is less with respect to image (a).

5.5 Conclusion

The geometric distortion in 3D ss-DWSTEPI was reduced by reducing the imaging FOV in the phase encoding direction with inner-volume-imaging. Parallel imaging technique further decreased the distortion, as expected. Improvement in SNR was achieved by combining ET_0 and ET_1 data. The proposed technique reduces geometric distortion and improves SNR in diffusion weighted imaging with 3D ss-DWSTEPI pulse sequence.

CHAPTER 6

CONCLUSIONS

6.1 Scientific Contributions

This dissertation mainly concentrates on developing various techniques to improve the accuracy in quantitative MRI by reducing motion-related and off-resonance artifacts in singleshot EP imaging. During the period of MRI acquisition, the problems we usually face may include various artifacts. For instance, a patient's involuntary motion generally induces blurring or ghosting artifacts. These artifacts reduce the accuracy of the quantitative MRI parameters, such as in diffusion tensor MR imaging.

2D singleshot-echo-planar-imaging (2D ss-EPI) completes the acquisition of the entire k-space data after a single RF excitation. 2D ss-EPI is a crucial tool for diffusion-tensor MRI to freeze the physiologic motion. Although the geometric distortion on the resultant EPI images limits its application mostly to DTI, DWI, and fMRI, the technique is useful in rapid imaging.

DWI and DTI are generally performed with signal averaging of multiple measurements to improve the signal-to-noise ratio (SNR) and the accuracy of the measurement. Any discrepancy in images between different averages causes errors in the calculation, which reduces the accuracy of diffusion MRI measurements. Translational and rotational motions during the application of diffusion gradients induce an additional phase term and a shift of the echo-peak position in k-space, respectively. These motions

also reduce the magnitude of the echo-peak. Based on these properties, a new scheme is presented, which monitors the position and the magnitude of the largest echo-peak in k-space. The position and the magnitude of each average are compared to those of early averaging shots to determine if the differences are within or beyond the given threshold values. Motion corrupted data are then reacquired in real time. The proposed technique reduced the inconsistency between images to be averaged, caused by subject motion during the application of the diffusion gradients.

The conventional stimulated-echo NMR sequence only measures the longitudinal component, while discarding the transverse component, after tipping up the prepared magnetization. This transverse magnetization can be used to measure a spin-echo, in addition to the stimulated-echo. 2D ss-SESTEPI is an EPI-based singleshot imaging technique that simultaneously acquires a spin-EPI (SEPI) and a stimulated-EPI (STEPI) after a single RF excitation. The magnitudes of SEPI and STEPI differ by T_1 decay for perfect 90^o RF pulses and can be used to rapidly measure the T_1 relaxation time. However, the spatial variation of B_1 amplitude induces uneven splitting of the transverse magnetization for SEPI and STEPI within the imaging FOV. Therefore, correction for B_1 inhomogeneity is critical for 2D ss-SESTEPI to be used for T_1 measurement. We developed a method for B_1 inhomogeneity correction by acquiring an additional stimulated-echo with minimal mixing time, calculating the difference between the spin-echo and the stimulated-echo and multiplying the stimulated-EPI by the inverse functional map. 2D ss-SESTEPI successfully measured both spin-echo and stimulated-echo in a singleshot. B_1 inhomogeneity correction was successfully achieved by acquiring an additional stimulated-echo with minimal mixing time during the prescan. Realtime T_1

measurement was possible using two images and an online image reconstruction program. It was possible to rapidly acquire T_1 mapping in a few seconds. However further time shortening was limited by SNR of the source spin- and stimulated-EP images. The measured T_1 agreed with those measured using conventional IR-TSE. 2D ss-SESTEPI may be an important tool for realtime in-vivo estimation of the concentration of paramagnetic-ion based contrast agent in DCE-MRI because it is rapid and the resultant images are free from motion-related artifacts.

The previously developed 3D ss-DWSTEPI pulse sequence acquires the entire k-space data after a single RF excitation. Inner volume imaging is used for localized volume imaging. It enables us to image a reduced FOV in the phase encoding direction without aliasing artifacts from the signal outside the imaging FOV. Correspondingly, in-plane resolution can be improved. However, the geometric distortion is eminent at/near the air/tissue and bone/tissue interfaces. EPI-related distortion increases with the increased FOV in phase-encoding direction. Parallel imaging was implemented into the 3D ss-STEPI to reduce the susceptibility artifact by increasing the k_y travel step. Inevitably, SNR is decreased with less acquired data. To compensate for the loss of signal, one additional image with slice encoding of k_z=0 is acquired between the third RF pulse and small α flip angle. The image is combined with the stimulated echo image to improve the SNR. This new design not only reduces the geometric distortion of the image but also advances the SNR. It has potentially wide applications in various tissue interfaces.

6.2 Future Work

Although the singleshot EPI-type techniques are less sensitive to the motion-related phase-error, there are residual effects from the subject motion strongly coupled to the large diffusion gradient. It will degrade the image quality and lead to the reduction in the accuracy on the DTI parameters. In an extreme case, the images acquired under the implement of pulse sequence are still not good enough after the reacquisition upper limit is reached. Two alternative methods may be selected. One is that the data are dropped from the data series. The other is to make use of reacquired data with minimal corruption. However, our ultimate goal for motion-corrupted diffusion weighted data is to completely remove the artifact induced by motion. There is a strong demand to develop new post-processing methods and correct the residual artifact in the image. Due to complicated motion pattern, there is no unique solution to motion artifact. It will take time and further study to correct the corresponding artifact based on various motion patterns.

T_1 map accuracy had been improved greatly by correcting B_1 inhomogeneity and the diffusion induced error. But several limited factors still play the key role in obtaining the accurate T_1 relaxation time map. For example, the mixing time must be taken carefully. Too short or too long mixing time both result in degrading the accuracy of the T_1 map. Diffusion-induced error on T_1 map heavily depends on the accuracy of measured diffusion coefficient.

REFERENCES

1. Bloch F, Hansen W, Packard M. The nuclear induction experiment. Phys Rev 1946;70:474-485.

2. Purcell EM, Torrey H, Pound R. Resonance absorption by nuclear magnetic moments in a solid. Phys Rev 1946;69:37-38.

3. Damadian R. Tumor detection by nuclear magnetic resonance. Science 1971;171(976):1151-1153.

4. Lauterbur PC. Image formation by induced local interactions: examples employing nuclear magnetic resonance. Nature 1973;242:190-191.

5. Kumar A, Welti D, Ernst R. NMR Fourier zeugmatography. J Magn Reson 1975;18:69-83.

6. Chapman A, Turner R, Ordidge R, Doyle M, Cawley M, Coxon R, Glover P, Mansfield P. Real-time movie imaging from a single cardiac cycle by NMR. Magn Reson Med 1987;5:246-254.

7. Edelstein W, Hutchinson J, Johnson G, Redpath T. Spin warp NMR imaging and applications to human whole-body imaging. Phys Med Biol 1980;25:751-756.

8. Pottumarthi V. Prasad. Magnetic resonance imaging methods and biologic applications. Walker JM, editor. Totowa: Humana Press; 2006.

9. Slichter C. Principles of magnetic resonance. Heidelberg, Germany: Springer-Verlag; 1990.

10. Morcos S, FRCS, FFRRCSI, FRCR. Nephrogenic systemic fibrosis following the administration of extracellular gadolinium based contrast agents: is the stability of the contrast agent molecule an important factor in the pathogenesis of this condition? The British J Radiology 2007;80:73-76.

11. Woessner D. Nuclear spin relaxation in ellipsoids undergoing rotational brownian motion. J Chem Phys 1962;37:647-654.

12. Bloembergen N, Purcell EM, Pound R. Relaxation effects in nuclear magnetic resonance absorption. Phys Rev 1948;73:679-712.

13. Jensen JH, Helpern JA. Special issue: iron-fortified MRI effects and applications of iron-induced NMR relaxation in biological tissues. NMR Biomed 2004;17(7).

14. Chen C-N, Hoult DI. Biomedical magnetic resonance technology. New York: IOP Ltd.; 1989.

15. Haacke E, Thompson M, Brown R. Magnetic resonance imaging, physical principles and sequence design: Wiley-Liss; 1999.

16. Bracewell RN. The Fourier transform and its applications.: McGraw-Hill 1986.

17. Liang ZP, Lauterbur PC. Principles of magnetic resonance imaging: a signal processing perspective. New York: Wiley-IEEE Press; 2000.

18. Robin A. de Graaf. In vivo NMR Spectroscopy principles and techniques. San Francisco: John Wiley & Sons, Ltd; 2007. 570 p.

19. Carr HY, Purcell EM. Effects on diffusion on free precession in nuclear magnetic resonance experiments. Phys Rev 1954;94:630-638.

20. Mansfield P. Multiplanar image formation using NMR. Journal of Physics 1977;C10:L55-L58.

21. Bernd UF, Dardo T, Elisabeth CC. Magnetic field shift due to mechanical vibration in functional magnetic resonance imaging. Magn Reson Med 2005;54(5):1261-1267.

22. Noll CD, Nishimura GD. Homodyne detection in magnetic resonance imaging. IEEE Trans Med Imag 1991;10(2):10.

23. Jeong EK, Kim SE, Guo J, Kholmovski EG, Parker DL. High-resolution DTI with 2D interleaved multislice reduced FOV single-shot diffusion-weighted EPI (2D ss-rFOV-DWEPI). Magn Reson Med 2005;54(6):1575-1579.

24. Griswold MA, Jakob PM, Heidemann RM, Nittka M, Jellus V, Wang J, Kiefer B, Haase A. Generalized autocalibrating partially parallel acquisitions (GRAPPA). Magn Reson Med 2002;47(6):1202-1210.

25. O'Sullivan J. A fast sinc function gridding algorithm for Fourier inversion in computer tomography. IEEE Trans Med Imag 1985;MI(4):200-207.

26. Jackson JI, Meyer CH, Nishimura DG. Selection of a convolution function for inversion using gridding. IEEE Trans Med Imag 1991;10(3):473-478.

27. Einestein A, editor. Investigation on the theory of the Brownian movement. New York: Dover Publication, Inc.; 1926. 119 p.

28. Stejskal E, Tanner J. Spin diffusion measurement: spin echoes in a presence of time dependent field gradient. J Chem Phys 1965;42:288-292.

29. Le Bihan D, Poupon C, Amandon A, Lethimonnier F. Artifacts and pitfalls in diffusion MRI. J Magn Reson Imaging 2006;24:478-488.

30. Ehman RL, Felmlee JP. Adaptive technique for high-definition MR imaging of moving structures. Radiology 1989;173(1):255-263.

31. Nguyen TD, Nuval A, Mulukutla S, Wang Y. Direct monitoring of coronary artery motion with cardiac fat navigator echoes. Magn Reson Med 2003;50(2):235-241.

32. Skare S, Andersson J. On the effects of gating in diffusion imaging of the brain using single shot EPI. Magn Reson Imaging 2001;19:1125-1128.

33. Wang JJ, Deichmann R, Hsiao I, Liu H, Wai Y, Wan Y, Turner R, Ordidge R. Selective averaging for the diffusion tensor measurement. Magn Reson Imaging 2005;23(4):585-590.

34. Anderson A, Gore J. Analysis and correction of motion artifacts in diffusion weighted imaging. Magn Reson Med 1994:379-387.

35. Ordidge RJ, Helperin J, Qing Z, Night R, Nagesh V. Correction of motion artifact in diffusion weighted MR images using navigator Echoes. MR Imaging 1994;12:455-460.

36. Butts K, Crespigny AJ, Pauly JM, Moseley ME. Diffusion weighted interleaved echo planar imaging with pair of orthogonal navigators. Magn Reson Med 1996;35:763.

37. Atkinson D, Porter DA, Hill DL, Calamante F, Connelly A. Sampling and reconstruction effects due to motion in diffusion-weighted interleaved echo planar imaging. Magn Reson Med 2000;44:101-109.

38. Butts K, Pauly JM, Crespigny AJ, Moseley ME. Isotropic diffusion weighted and spiral navigated interleaved EPI for runtime imaging of acute stroke. Magn Reson Med 1997;38:741-749.

39. Norris DG. Implications of bulk motion for diffusion-weighted imaging experiments: effects, mechanisms, and solutions. J Magn Reson Imag 2001;13:486-495.

40. Liu C, Bammer R, Kim DH, Moseley ME. Self-navigated interleaved spiral (SNAILS): application to high-resolution diffusion tensor imaging. Magn Reson Med 2004;52:1388-1396.

41. Pipe JG, Farthing VG, Forbes KP. Multishot diffusion-weighted FSE using PROPELLER MRI. Magn Reson Med 2002;47(1):42-52.

42. Le Bihan D, Mangin J, Poupon C, Clark C, Pappata S, Molko N, Chabriat H. Diffusion tensor imaging: concepts and applications. JMRI 2001;13:534-546.

43. Jeong EK, Kim SE, Guo J, Kholmovski EG, Parker DL. High-resolution DTI with 2D interleaved multislice reduced FOV single-shot diffusion-weighted EPI (2D ss-rFOV-DWEPI). Magn Reson Med 2005;54(6):1575-1579.

44. Conturo TE, McKinstry RC, Akbudak E, Robinson BH. Encoding of anisotropic diffusion with tetrahedral gradients: a general mathematical diffusion formalism and experimental results. Magn Reson Med 1996;35(3):399-412.

45. Merboldt KD, Hanicke W, Bruhn H, Gyngell ML, Frahm J. Diffusion imaging of the human brain in vivo using high-speed STEAM MRI. Magn Reson Med 1992;23(1):179-192.

46. Farrell JA, Smith SA, Gordon-Lipkin EM, Reich DS, Calabresi PA, van Zijl PC. High b-value q-space diffusion-weighted MRI of the human cervical spinal cord in vivo: feasibility and application to multiple sclerosis. Magn Reson Med 2008;59(5):1079-1089.

47. Aletras AH, Ding S, Balaban RS, H. W. DENSE: displacement encoding with stimulated echoes in cardiac functional MRI. J Magn Reson 1999;137(1):247-252.

48. Frahm J, Bruhn H, Gyngell ML, Merboldt KD, Hanicke W, Sauter R. Localized high-resolution proton NMR spectroscopy using stimulated echoes: initial applications to human brain in vivo. Magn Reson Med 1989;9(1):79-93.

49. Haase A, Frahm J, Matthaei D, Hanicke W, Bomsdorf H, Kunz D, Tischler R. MR imaging using stimulated echoes (STEAM). Radiology 1986;160(3):787-790.

50. Peter Bornert, Dye Jensen. Single-shot-double-echo EPI. Magn Reson Imaging 1994;12(7):1033-1038.

51. Feng Y, Jeong EK, Mohs AM, Emerson L, Lu ZR. Characterization of tumor angiogenesis with dynamic contrast-enhanced MRI and biodegradable macromolecular contrast agents in mice. Magn Reson Med 2008;60(6):1347-1352.

52. Nicolle GM, Eva Toth, Heribert Schmitt-Willich, Bernd Raduchel, Merbach AE. The impact of rigidity and water exchange on the relaxivity of dendritic MRI contrast agent Chem Eur J 2002;8(5):9.

53. Deoni SC, Rutt BK, Peters TM. Rapid combined T1 and T2 mapping using gradient recalled acquisition in the steady state. Magn Reson Med 2003;49(3):515-526.

54. Tofts PS, editor. Quantitative MRI of the Brain: measuring changes caused by disease. West Sussex, England; 2004.

55. Gowland P, Mansfield P. Accurate measurement of T1 in vivo in less than 3 seconds using echo-planar imaging. Magn Reson Med 1993;30(3):351-354.

56. Look DC, Locker DR. Time saving in measurement of NMR and EPR relaxation times. Review of Scientific Instruments 1970;41(2):2.

57. Guo JY, Kim SE, Parker DL, Jeong EK, Zhang L, Roemer RB. Improved accuracy and consistency in T1 measurement of flowing blood by using inversion recovery GE-EPI. Medical physics 2005;32(4):1083-1093.

58. Liu X, Feng Y, Lu ZR, Jeong EK. Rapid simultaneous data acquisition of T_1 and T_2 mapping, using multishot EPI and automated variations of TR and TE at 3T. 2007; Berlin, Germany.

59. Liu X, Feng Y, Lu ZR, Morrell G, Jeong EK. Rapid simultaneous acquisition of T_1 and T_2 mapping images using multishot double spin-echo EPI and automated variations of TR and TE (ms-DSEPI-T12). NMR Biomed 2009(23):97-104.

60. Jeong EK, Kim SE, Kholmovski EG, Parker DL. High-resolution DTI of a localized volume using 3D single-shot diffusion-weighted STimulated echo-planar imaging (3D ss-DWSTEPI). Magn Reson Med 2006;56(6):1173-1181.

61. Wang Y, Ye F, Jeong EK, Sun Y, Parker DL, Lu ZR. Noninvasive visualization of pharmacokinetics, biodistribution and tumor targeting of poly[N-(2-hydroxypropyl)methacrylamide] in mice using contrast enhanced MRI. Pharmaceutical research 2007;24(6):1208-1216.

62. Saritas EU, Cunningham CH, Lee JH, Han ET, Nishimura DG. DWI of the spinal cord with reduced FOV single-shot EPI. Magn Reson Med 2008;60(2):468-473.

63. Wansapura JP, Holland SK, Dunn RS, RT, Ball WS. NMR relaxation times in the human brain at 3.0 Tesla. J Magn Reson Imaging 1999;9:531-538.

64. Stanisz GJ, Odrobina EE, Pun J, Escaravage M, Graham SJ, Bronskill MJ, Henkelman RM. T_1, T_2 relaxation and magnetization transfer in tissue at 3T. Magn Reson Med 2005;54:507-512.

65. Ethofer T, Mader I, Seeger U, Helms G, Erb M, Grodd W, Ludolph A, Klose U. Comparison of longitudinal metabolite relaxation times in different regions of human brain at 1.5 and 3 tesla. Magn Reson Med 2003;50:1296-1301.

66. Preibisch C, Deichmann R. T_1 mapping using spoiled FLASH-EPI hybrid sequences and varying flip angle. Magn Reson Med 2009;62:240-246.

67. Daisy Chien, Richard B. Buxton, Kenneth K. Kwong, Thomas J. Brady, Rosen BR. MR diffusion imaging of the human brain. Journal of Computer Assisted Tomography 1990;14(4):514-520.

68. Moseley ME, Cohen Y, Mintorovitch J, Chileuitt L, Shimizu H, Kucharczyk J, Wendland MV, Weistein PR. Early detection of regional cerebral ischemia in cats: comparison of diffusion- and T2 weighted MRI and spectroscopy. Magn Reson Med 1990;14:330-346.

69. Michael CH, MSc, Ulug AM, Lijuan Z, Marcus HH, Barry JD, Robert ZD, Richard W. Distribution of microstructure damage in the brains of professional boxers: a diffusion MRI study. Journal of Magnetic Resonance Imaging 2006;24:537-542.

70. Basser PJ, Pierpaoli C. A simplified method to measure the diffusion tensor from seven MR images. Magn Reson Med 1998;39:928-934.

71. Song SK, Sun SW, Ju WK, Lin SJ, Cross AH, Neufeld AH. Diffusion tensor imaging detects and differentiates axon and myelin degeneration in mouse optic nerve after retinal ischemia. Neuroimage 2003;20(3):1714-1722.

72. Clark CA, Werring DJ, Miller DH. Diffusion imaging of the spinal cord in vivo: estimation of the principal diffusivities and application to multiple sclerosis. Magn Reson Med 2000;43:133-138.

73. Schenck J. The role of magnetic susceptibility in magnetic resonance imaging: MRI magnetic compatibility of the first kind and the second kinds. Med Phys 1996;23:815-850.

74. Jezzard P, Barnett A, Pierpaoli C. Characterization of and correction for eddy current artifacts in echo planar diffusion imaging. Magn Reson Med 1998;39:801-812.

75. McKinnon GC. Ultrafast interleaved gradient-echo-planar imaging on a standard scanner. Magn Reson Med 1993;30:609-616.

76. Butts K, Riederer SJ, Ehman RL, M T, Jack C. Interleaved echo planar imaging on a standard MRI system. Magn Reson Med 1994;31:67-72.

77. Brockstedt S, Moore J, Thompson C, Holtas S, Stahlberg F. High-resolution diffusion imaging using phase-corrected segmented echo-planar imaging. magn Reson Imaging 2000;18:649-657.

78. Liu C, Moseley M, Bammer R. Simultaneous phase correction and SENSE reconstruction for navigated multi-shot DWI with non-Cartesian k-space sampling. Magn Reson Med 2005;54:1412-1422.

79. Kuhl C, Gieseke J, von Falkenhausen M. Sensitivity encoding for diffusion-weighted MR imaging at 3.0T: intraindividial comparative study. Radiology 2005;234:517-526.

80. Jeong EK, Kim SE, EG K, Parker DL. High resolution DTI of localized volume, using 3D singleshot stimulated EPI. 2006; Seattle, WA.

81. Feinberg D, Hoenninger J, Crooks L, Kaufman L, Watts J, Arakawa M. Inner volume MR imaging: technical concepts and their application. Radiology 1985;156:743-747.

82. Robert T, Markus vK, Chrit TWM, Peter CMvZ. Single-shot localized echo-planar imaging (STEAM-EPI) at 4.7 tesla. Magn Reson Med 2005;14(2):401-408.

83. Kai TB, Jens F. Radial single-shot STEAM MRI. Magn Reson Med 2008;59(4):686-691.

84. Wang Z, Wang j, Detre JA. Improved data reconstruction method for GRAPPA. Magn Reson Med 2005;54:738-742.

85. Kholmovski EG, Samsonov A. GARSE: Generalized autocalibrating reconstruction for sensitivity encoded MRI. 2005; Miami, FL. p 2672.